TUNING STRUCTURE AND THERMAL EVOLUTION OF HIGH-ZT THERMOELECTRICS USING FIRST PRINCIPLES

by

Hyoungchul Kim

A dissertation submitted in partial fulfillment
of the requirements for the degree of
Doctor of Philosophy
(Mechanical Engineering)
in the University of Michigan
2013

Doctoral Committee:

Professor Massoud Kaviany, Chair
Professor Ctirad Uher
Associate Professor Anton Van der Ven
Associate Professor Pramod Sangi Reddy

Acknowledgements

Since starting my graduate studies here in Ann Arbor, I have been fortunate to meet many outstanding researchers, educators, labmates, and friends. Without their help and inputs, it would have been impossible to complete this work. I would like to specially thank Professor Massoud Kaviany, my advisor, for being a constant source of motivation and valuable discussions which led to novel ideas. I am thankful to Professors Ctirad Uher, Anton Van der Ven, and Pramod Sangi Reddy, my Ph.D. Committee Members, for their evaluation of my thesis and for their valuable comments.

I would like to express gratitude to Dr. John C. Thomas, and Dr. Kiyong Ahn (Hanyang University) and Professor Stephen Stackhouse (University of Leeds) for discussions related to the non-equilibrium *ab-initio* molecular dynamics and the density-functional theory in general. I am thankful to Professor Jeffrey Snyder (California Institute of Technology) and Dr. David Parker (Oak Ridge National Laboratory) for discussions related to electronic structure and transport properties of lead chalcogenides. I am also grateful to Dr. Adam Weber (Lawrence Berkeley National Laboratory) for helpful comments on phase-change degradation of catalyst layers.

I would like to extend special thanks to all my current and the former and labmates; Baoling Huang, Nikolai Sergeev, Gisuk Hwang, Jedo Kim, Seungha Shin, Charles Endouard, Corey Melnick, and Hang Chi for their guidance and extensive discussions related to research and everyday life. The Mechanical Engineering and Center for Solar and Thermal Energy Conversion staff, including Kelly Chantelois and Brenda Vyletel, have been of tremendous help to me. I would like to mention my appreciation for the help and support from Professor Mansoo Choi (Seoul National University) and from labmates in the Korea Institute of Science and Technology, through my years at those institutions.

Finally, special thanks to my wife Joung Min Seo and my daughters, Narin and Alice Nayeon. They have always cheered me up and stood by my side. Also, I greatly appreciate the constant support and love of my parents and parents-in-law for during many years of my education both in Korea and in the United States.

The work was supported by the Center for Solar and Thermal Energy Conversion at the University of Michigan, an Energy Frontier Research Center funded by the U.S. Department of Energy, Office of Science, Basic Energy Sciences under Award No. DE-SC-0000957.

Table of Contents

List of Figures

List of Tables

List of Appendices

Nomenclature

A	area
A_i	constant of component i
a	lattice parameter
B	bulk modulus
B_i	constant of component i
C_{ij}	elastic constant
c	constant
c_v	specific heat capacity
D_i	density-of-states of carrier i
D_{ij}	dynamical matrix
$\boldsymbol{d}$	displacement vector
d_g	grain diameter
E	energy
e_c	electron charge, 1.602×10^{-19} C
$\boldsymbol{F}$	force vector
F	free energy

F_i	force of component i
f	frequency
f_i°	distribution function of carrier i
G	shear modulus
H	Hamiltonian
$\hbar$	reduced Planck constant, 6.582×10^{-16} eV-s
j_i	flux of component i
$\boldsymbol{k}$	wave vector
k_B	Boltzmann constant, 8.617×10^{-5} eV/K
L_{ij}	coupling transport coefficient
l	length
M	molecular weight
M_{ij}	matrix
m	atomic mass
$m_{i,e}$	effective mass of carrier i
N	number of atoms in a cell
N_A	Avogadro constant, 6.022×10^{23} 1/mol
$N_{i,\alpha}$	orbital degeneracy of carrier i
$N_{\mathrm{L},\circ}$	Lorenz number, 2.44×10^{-8} W-Ω/K^2
n	number density
n_i	concentration of carrier i
$\boldsymbol{p}$	momentum

Q	heat flux
$\boldsymbol{q}$	heat current vector
q_e	electrical (effective) charge
$\boldsymbol{R}$	position vector of nuclei
R	atomic radius
R_{H}	Hall coefficient
$\boldsymbol{r}$	particle position vector
r	bond length, inter-particle separation
r_{H}	Hall factor
$r_\circ$	equilibrium bond length
S	entropy
T	temperature
t	time
$\boldsymbol{u}$	velocity vector
u_p	phonon speed
V	volume
V_α	effective cluster interactions
V_i	potential (or functional) of component i
$V_\circ$	average volume per atom
v_i	velocity of carrier i
z	atomic number

Greek symbols

α	coefficient of thermal expansion
α^2F	Eliashberg spectral function
α_{S}	Seebeck coefficient
Δ	difference
δ_{D}	Dirac delta function
$\epsilon_{\circ}$	vacuum permittivity
ϵ_e	relative permittivity
ε	porosity
ε_i	eigenvalue of state i
Γ_α	cluster basis function
Γ_{ij}	force constants
Γ_s	scattering parameter
γ_{G}	Grüneisen parameter
$\dot{\gamma}$	transition rate
κ_i	thermal conductivity of component i
μ_i	chemical potential of carrier i
ϕ	electron states (or orbitals)
ρ	density
σ_e	electrical conductivity
τ	time constant, relaxation time
τ_i	relaxation time of carrier i
φ	potential

$\varphi_\circ$	potential minimum
θ	bond angle
ψ	wave function
ω	angular frequency

Subscripts

A	acoustic
a	activation
c	crystal
D	Debye
d	defect
e	electron
eff	effective
e, g	electron bandgap
ep	polaron
ext	external
F	Fermi level
f	formation
g	group
H	Hartree
h	hopping
i	summation index, particle label

i, e	effective contribution of carrier i
ion	ionic contribution
j	summation index, particle label
KE	kinetic energy
L	lattice
L	longitudinal
lg	long-range
m	melting
min	minimum
mix	mixing
n	nuclei
O	optical
$\circ$	total
p	phonon
s	scattering
sh	short-range
spin	spin
T	transport
T	transverse
tr	transition
XC	exchange-correlation

Superscripts

$\circ$	equilibrium
V	vacancy
x	(doping or alloying) concentration
$*$	complex conjugate

Others

$\langle\ \rangle$	average
∞	infinity

Abbreviations

ADP	atomic displacement parameter
AIMD	*ab-initio* molecular dynamics
BCC	body-centered cubic
BTE	Boltzmann transport equation
CBM	conduction band minimum
CE	cluster expansion
CRs	combinative rules
CV	cross-validation
DFT	density-functional theory
EAIMD	equilibrium *ab-initio* molecular dynamics
ECI	effective cluster interactions
ECMD	equilibrium classical molecular dynamics
FCC	face-centered cubic
GGA	generalized gradient approximation
`GULP`	general utility lattice program
HCACF	heat current autocorrelation function

HF	Hellmann-Feynman
MC	Monte Carlo
MD	molecular dynamics
NEAIMD	non-equilibrium *ab-initio* molecular dynamics
NpT	isothermal-isobaric, constant of moles, pressure, and temperature
NVE	microcanonical, constant of moles, volume, and energy
PAW	projected augmented wave
PBE	Perdew-Burke-Ernzerhof
RDF	radial distribution function
RMS	root-mean-square
RTA	relaxation time approximation
TE	thermoelectric
`VASP`	Vienna *ab-initio* software package
VBM	valence band maximum
ZT	thermoelectric figure-of-merit

ABSTRACT

TUNING STRUCTURE AND THERMAL EVOLUTION OF HIGH-ZT THERMOELECTRICS USING FIRST PRINCIPLES

by

Hyoungchul Kim

Chair: Massoud Kaviany

In this study, using the first-principles based atomistic simulations, we address tuning of the atomic structure of thermoelectric (TE) materials manifested through the roles of phonons and charge carriers in the TE figure-of-merit (ZT). This computational work suggests new, systematic and extensive methods to analyze such temperature-dependent phonon scatterings and charge carrier mechanisms mediated with temperature-evolved lattice vibration. Through a unified and integrated approach we show that, bulk, homogeneous high-ZT materials take advantage of atomic displacements through their bond softening, phase change, anharmonicity, thermal disorder, and phonon red shifting to reduce their lattice thermal conductivity, while enhancing (or non-deteriorating) their charge transport properties. The TE conversion of intermediate waste heat ($600 < T < 900$ K) is most practical and we consider a range of structures (rocksalt-/antifluorite-based chalcogenides, filled/substituted skutterudites, and icosahedral-based borides) and show how each structure allows for atomic tuning for improved ZT.

Ab-initio molecular dynamics (AIMD) show the rocksalt structure (PbTe) ex-

periences thermal disorder (high-temperatures, off-lattice dislocation due to anharmonicity) and this leads to temperature-dependent effective mass and band convergence and suppression or the long-range acoustic phonon transport, resulting in high ZT. Through *ab-initio* phase diagram prediction we reveal that point and phase-boundary scatterings significantly reduce lattice thermal conductivity in filled skutterudites ($Ba_xCo_4Sb_{12}$). With AIMD we show in atomic substitution $Co_4(Sb,Ge,Te)_{12}$ configuring the pnicogen rings lowers lattice thermal conductivity and suggest the combination of filler and substitution will further reduce lattice thermal conductivity. With direct non-equilibrium AIMD we predict the anomalous temperature-independent behaviors of the Seebeck coefficient and lattice thermal conductivity of the icosahedral-based borides ($B_{13}C_2$). Our statistical entropy analysis supports this significant vibrational contribution (phonon softening) to the Seebeck coefficient. In antifluorite-based chalcogenides (β-Cu_2Se), the large displacement of the Cu^+ ions in the interstitial sites results in low lattice thermal conductivity, and we suggest alloying Se with Te for higher ZT.

We compare these first-principles based predictions with the available experiments and find good agreement. In this study, we have demonstrated the relations, metrics and tuning of the thermal evolution of the atomic displacements for optimal phonon and charge carrier TE properties.

Chapter 1

Introduction

Thermoelectricity is direct conversion of heat energy into electrical power (and vice versa) expected to have a significant impact in power generation from waste heat and sub-room-temperature cooling. Its efficiency is presented by the thermoelectric (TE) figure-of-merit (ZT),

$$ZT = \frac{\alpha_{\mathrm{S}}^2 \sigma_e T}{\kappa_e + \kappa_L}, \tag{1.1}$$

where T, α_{S}, σ_e, κ_e, and κ_L are temperature, the Seebeck coefficient, electrical conductivity, and electronic and lattice thermal conductivities. To consider improvement of ZT, it is divided into the power factor, $\alpha_{\mathrm{S}}^2 \sigma_e$, and the thermal transport, $\kappa = \kappa_e + \kappa_L$. Simultaneous increase in the power factor and decrease in the total thermal conductivity is a challenge, since they are highly coupled. So the goal is to increase ZT even though one of those two may change undesirably.

In this chapter, we discuss the analyses/computations of the TE transport processes involving phonon and charge carriers. We also discuss the goal/focus/objective

of our high-ZT materials search.

1.1 Tuning Atomic Structures for High ZT

In search for high-ZT materials, the bulk, homogeneous compounds have been receiving increased attention and have shown superior results compared the pure bulk materials. Nevertheless such compounds still have low TE efficiency (considering practical usage), thus requiring complex TE-module system for achieving the best performance possible. So, parallel to the advances in the nanostructured (e.g., superlattice, quantum dot, wire and well) TE materials, the bulk compounds using advances in tuning of atomic motion and displacement have evolved. There have been recent experimental and theoretical/computational prediction successes in this area.

Atomistic motion/displacement in TE materials allows for tuning properties for superior ZT. In classical mechanics, the Hamiltonian H($\boldsymbol{r}$,$\boldsymbol{p}$) is a function describing the energy state of a mechanical system. The total Hamiltonian of a system (N particle) is

$$\mathrm{H}(\boldsymbol{r},\boldsymbol{p}) = \sum_{i=1}^{3N} \frac{p_i^2}{2m} + \sum_{i=1}^{N}[\varphi_{\mathrm{ext}}(\boldsymbol{r}_i) + \sum_{i<j}^{N} \varphi_{ij}(\boldsymbol{r}_i - \boldsymbol{r}_j)], \tag{1.2}$$

where $\boldsymbol{r}$ is the position vector, $\boldsymbol{p}$ is the momentum, m is the mass, φ_{ext} is the external potential, and φ_{ij} is the interparticle pair potential. Neglecting the external effects, the total Hamiltonian is determined by the position, momentum and interactions of particles. In quantum mechanics, similarly, the Hamiltonian operator of the system

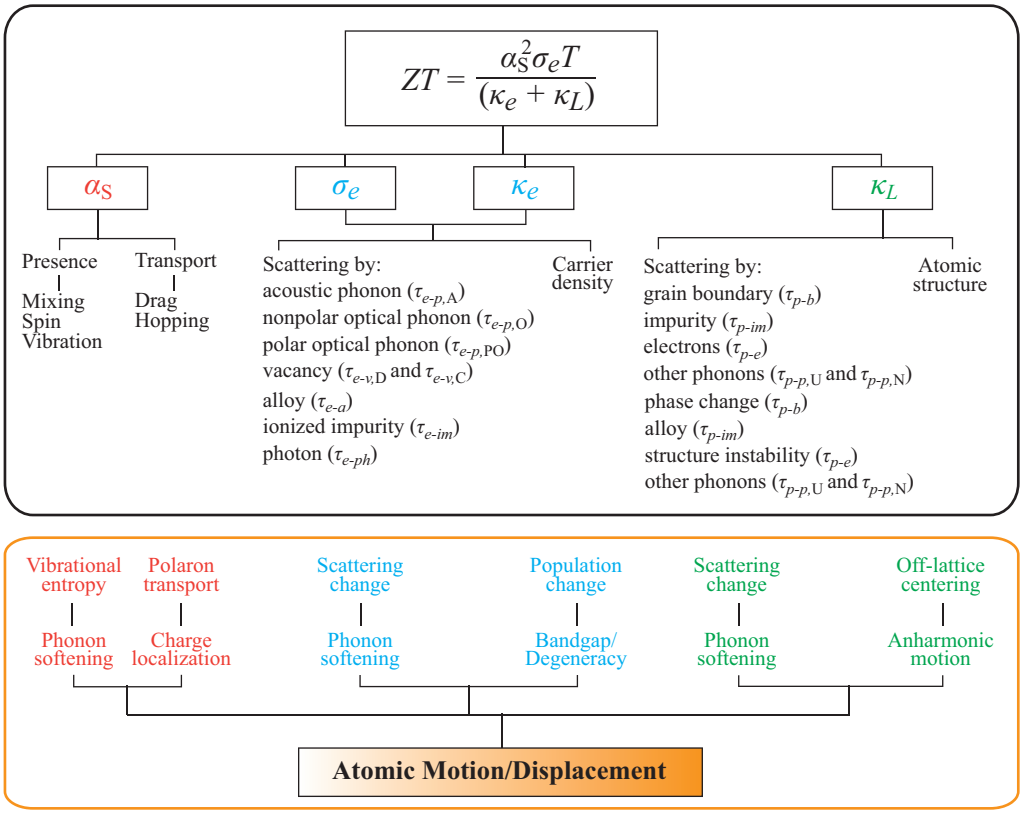

Figure 1.1: The TE figure-of-merit and the four transport properties within it (top panel). Each property is related to the atomic structure, displacement and motion (lower panel). By proper tuning of these atomic properties, the figure-of-merit is optimized.

is the sum of its kinetic and potential energy,

$$\mathrm{H} = -\frac{\hbar^2}{2m}\nabla^2 + \varphi(\boldsymbol{r}) \quad \text{and} \quad \varphi = \varphi_{\text{ext}} + \varphi_c + \varphi_s, \tag{1.3}$$

where $\hbar$ is the reduced Planck constant, φ_c is the crystal potential (in harmonic oscillator, $\varphi_c = \Gamma x^2/2$), and φ_s is the scattering potentials. As stated in Eqs. (1.2) and (1.3), the accurate description and prediction of the atomic motion/displacement is essential. Also these become even more important since the electronic and structural metrics derived from harmonic and quasi-harmonic approximations have several limits. These accurate predictions are now possible with the advances in multi-scale and multi-physics treatments of TE properties. So, using these and example structures [lead tellurides (Chapter 3), skutterudites (Chapters 4 and 5), boron carbides (Chapter 6), copper selenides (Chapter 7), and uranium dioxides (Appendix B)], we investigate the roles of atomic thermal displacement in these high ZT materials.

As shown in Fig. 1.1, enhancement of the TE transport properties, the Seebeck coefficient, electrical conductivity, and thermal conductivity, can be achieved by choosing/modifying the various independent and coupled contributions. We approach these with perspective of the effects of the atomic motions/displacements. Especially, the electronic metrics (e.g., charge localization, band convergence, and phonon-coupled effects) of the intrinsically or extrinsically displaced atoms are closely related with the power factor and electronic thermal conductivity. The structural metrics for these displacements (e.g., force constants, phase, mass difference, and displacement parameter) show their dominant roles in the lattice thermal conductivity.

This research examines the effects of tuned atomic motions/displacements on the TE transport, with the aim of gaining understanding and finding the fundamental solutions for achieving high-ZT. Employing the first-principles based analyses, we successfully predict the temperature- and constituent-dependent atomic motions. Detail explanations of each energy carriers are given in the following sections.

1.2 Phonon Roles in TE Properties

In most solids, the acoustic phonons are the dominant heat carriers, while the optical phonons dominate the scattering of the electrons in semiconductors. So, understanding and predicting the roles of phonons in TE materials is essential for tuning their transport properties. From Eq. (1.3), the Hamiltonian of the phonon (p) system is expressed as

$$\mathrm{H}_p = \sum_{\boldsymbol{r}} \frac{1}{2m} p^2(\boldsymbol{r}) + \frac{1}{2} \sum_{\boldsymbol{r},\boldsymbol{r'}} d_i(\boldsymbol{r}) D_{ij}(\boldsymbol{r} - \boldsymbol{r'}) d_j(\boldsymbol{r'}), \tag{1.4}$$

where D_{ij} is the dynamical matrix element, d_i is the displacement of atom i. As expected, the phonon properties, including their interactions with other carriers, are determined by the elemental constituents and their position and movement. Then in tuning the structural metrics of the high ZT materials, the simplest and most effective manners of achieving high ZT is the reduction of lattice thermal conductivity.

Figure 1.2 schematically illustrates the various phonon scattering strategies used in this research to reduce the lattice thermal conductivity. The lattice thermal con-

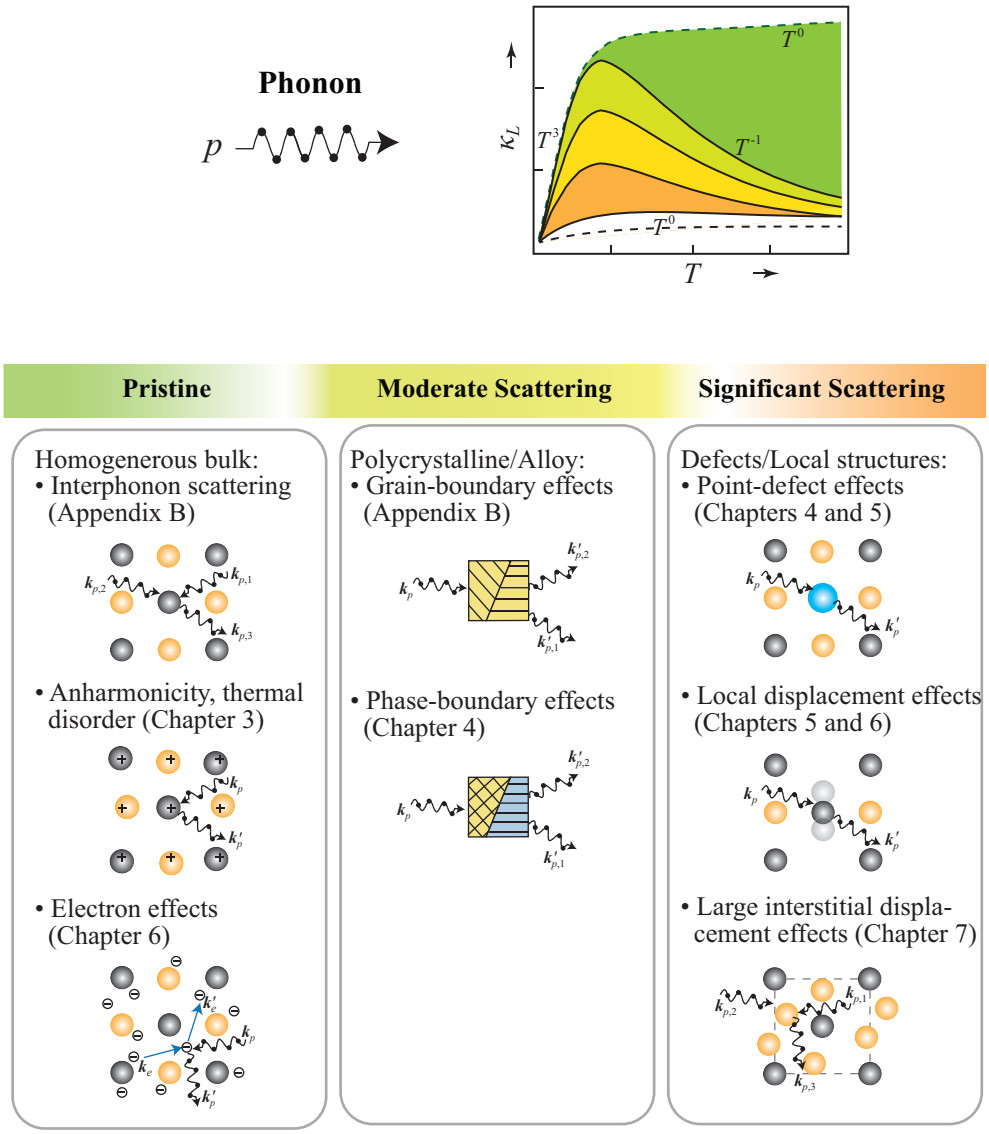

Figure 1.2: Tuning of the phonon scattering mechanisms with elemental constituents and their motions, and displacements. The reductions in the temperature-dependent lattice thermal conductivity, via different scattering mechanisms, are represented by the color coding of the mechanism (top graph).

ductivity of the bulk, homogeneous TE materials is very sensitive to the temperature. If the thermal vibration is harmonic, then in a perfect single crystal, at high temperatures the mean-free-path of the phonons is infinite (no interphonon scatterings occurs). We represent this ideal transport on top of Fig. 1.2, for high temperature ($T \gg T_{\mathrm{D}}$), as a large constant. Due to anharmonic atomic motions and the interphonon scatterings (mainly the Umklapp processes; Appendix B and Chapter 3) the real single-crystal solids show a T^{-1} temperature dependence at high temperatures. The scattering by electron-phonon interactions (Chapter 6), grain boundary (Appendix B), and impurity dominant ($\sim T^3$) are dominant at low temperature ($T \ll T_{\mathrm{D}}$). This is also shown in Fig. 1.2.

The high-temperature behavior is consistent with the Slack relation [98, 105, 185],

$$\kappa_{L,\mathrm{S}}(T) = \frac{3.1 \times 10^4 \langle M \rangle V_{\circ}^{1/3} T_{\mathrm{D},\infty}^3}{T \langle \gamma_{\mathrm{G}}^2 \rangle N^{2/3}}, \tag{1.5}$$

where $\langle M \rangle$ is the average atomic weight, N is the number of atoms, $V_{\circ}$ is the average volume per atom, $T_{\mathrm{D},\infty}$ is the Debye temperature, and $\langle \gamma_{\mathrm{G}} \rangle$ is the average Grüneisen parameter, over the temperature range considered. The Slack relation successfully describes the lattice thermal conductivity dominated by the long-range acoustic transport and interphonon scattering, including moderate anharmonicity. However, the modern TE materials are not limited to these bulk, homogeneous, moderate grain-boundary and impurities materials. Rather, the new materials have extended to compounds and alloys, so the accurate considerations of significant other scattering mechanisms (e.g., high anharmonicity, phase-boundary, large mass fluctuation, and

large displacement effects) are required. Interestingly these scattering mechanisms which are accompanied with unique defect (or local) structures, are highly temperature dependent (Fig. 1.2). Previous lack of systematic approach, including the thermal evolution and disorder, has been one of the shortcomings in the analyses. In this research, we suggest new, systematic and extensive analysis methods to analyze such temperature-dependent phonon scatterings based on first principles. In particular, the high anharmonicity and the large (local or interstitial) atomic displacement observed at high temperatures, which are significant but unexplored phonon scattering mechanisms, are considered with appropriate example structures (skutterudites in Chapters 4 and 5, boron carbides in Chapter 6, and copper selenides in Chapter 7). With these significant, structure-related scatterings, the long-range acoustic phonon transport is mostly suppressed, and the lattice thermal conductivity reaches a plateau (i.e., temperature independent, $\sim T^0$), similar to the minimum (amorphous) lattice thermal conductivity suggested by Cahill and Pohl [33, 34].

1.3 Charge Carriers and Their Roles in TE Properties

The electronic TE transport properties, the power factor and the electronic thermal conductivity, are governed by the transport/interaction mechanisms of the charge carriers (electron, hole, and polaron) with phonons, etc. As mentioned in the previous section, these properties are highly coupled, thus challenging to control them inde-

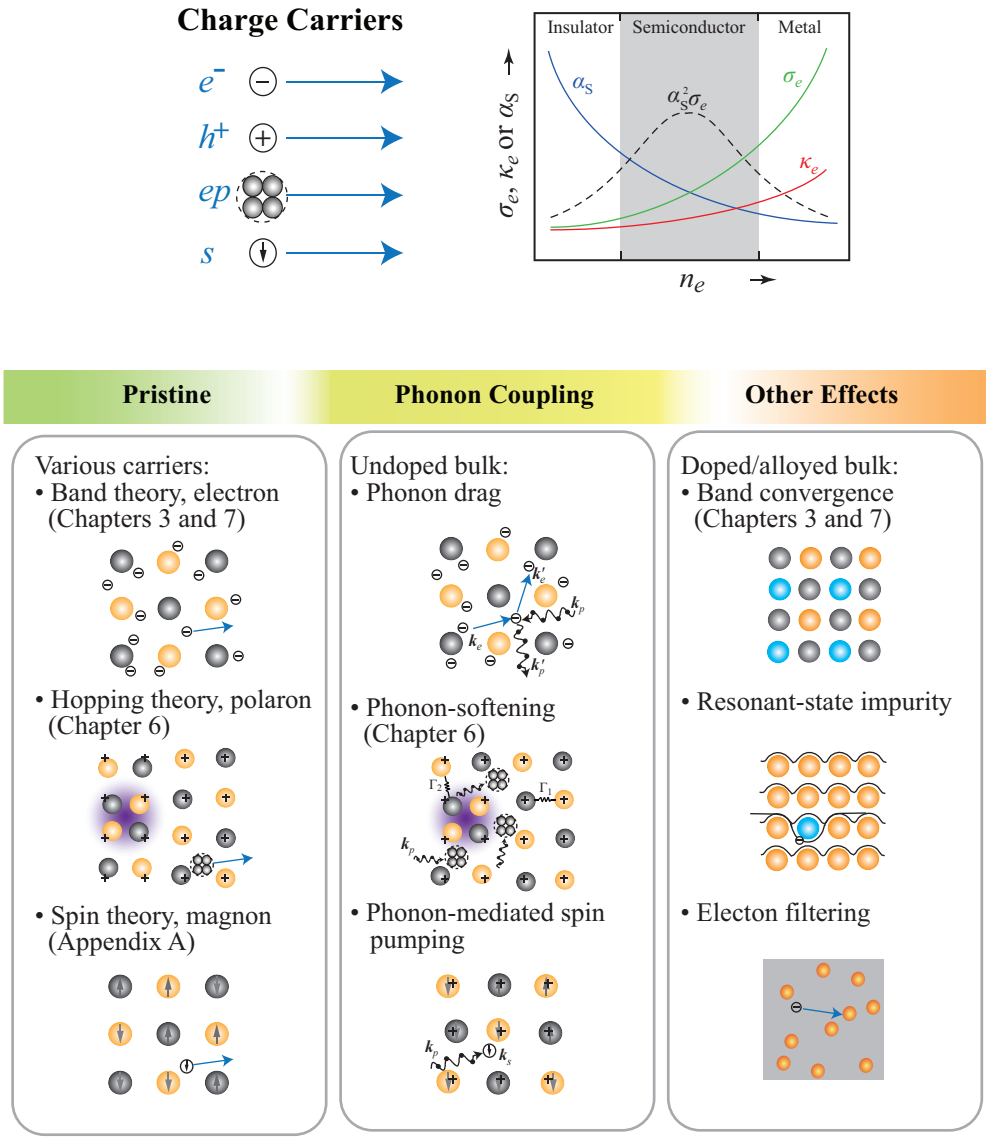

Figure 1.3: Tuning of the electronic transport mechanisms with respect to various charge carriers (electron, hole, polaron, and magnon). They are migrated TE properties as a function of carrier concentration are also shown (top graph).

pendently (Fig. 1.3 top, right image). From Eq. (1.3), the electronic Hamiltonian H_e with the relevant electron (e) and nucleus (n) potential energies, $\varphi = \varphi_{n-e} + \varphi_{e-e} + \varphi_{n-n}$, is given as

$$\mathrm{H}_e = -\sum_i \frac{\hbar^2}{2m}\nabla^2 - \frac{e_c^2}{4\pi\epsilon_\circ}\left(\sum_i^{N_e}\sum_I^{N_n}\frac{3I}{|\boldsymbol{R}_I - \boldsymbol{r}_i|} + \sum_i^{N_e}\sum_{j<i}^{N_e}\frac{1}{|\boldsymbol{r}_i - \boldsymbol{r}_j|} + \sum_I^{N_n}\sum_{J<I}^{N_n}\frac{z_I z_J}{|\boldsymbol{R}_I - \boldsymbol{R}_J|}\right), \tag{1.6}$$

where $\boldsymbol{R}$ is the position of nuclei and z is the atomic number. As expressed in Eq. (1.6), these electronic properties are also highly affected by the atomic structure, motion and displacement. So, the optimization of the structural metrics (e.g., charge localization, band convergence, and phonon-coupling effects) for achieving high ZT introduced in relation to phonons in Section 1.2 also induce negative changes in the electronic properties.

The overall tuning mechanisms for the charge carriers (electron, hole, polaron, and magnon) considered in this research are illustrated in Fig. 1.3. Each carrier contributes to the electronic TE transport properties and they are highly coupled with the phonons through the effects of the constituent atoms and the temperature-dependent atomic displacements.These relations allow for range of possible enhancements to the TE transport properties through each of the charge carrier. For the electron obeying the classic band theory, outlined in Fig. 1.3, the prominent tuning processes are the phonon drag, significant anharmonic lattice vibration (band convergence of lead tellurides in Chapter 3), and phonon softening (boron carbides in Chapter 6). For the polaron and magnon derived from the hopping and spin theories, phonon-assisted polaron hopping and the phonon-mediated spin pumping are possible. In addition, some

constituent-atom tuning may provide other effects (copper selenides in Chapter 7) in electronic state of the alloyed or doped TE materials. Although these effects have been examined in several experiments, no reliable confirmation or accurate prediction with the first principles has been reported yet. So, these complementary electronic tuning mechanisms, such as phonon assisted or resonant state, provide for simultaneous additional increases in the Seebeck coefficient and electrical conductivity which are useful for achieving high-ZT TE materials.

1.4 Thesis Objective and Organization

The major objective of this work is to understand/predict/tune the roles of the phonon and charged carriers in the four TE transport properties in search for high ZT bulk, homogeneous materials. The thesis is organized in eight chapters and two appendices as follows.

Chapter 2 introduces various computational methods used throughout this thesis. A brief overview/description of the multiple time- and length-scale treatments provides an integrated understanding for the calculations of the ground-state atomic structure, the electronic and phonon states, and their interactions and TE transport properties.

In Chapter 3, the effects of thermal-disordered anharmonicity in solids (here, PbTe) on phonons and electrons are examined using the density-functional theory (DFT) (including equilibrium *ab-initio* molecular dynamics, EAIMD) and equilibrium classical molecular dynamics (ECMD). The band convergence phenomenon occurring

with increased temperature is closely related to the structural thermal evolution (i.e., thermal disorder) and the TE properties of the p-doped PbTe. Lack of short-range order causes local overlap of the valence orbitals and increase in the density-of-states near the Fermi level. The effective mass becomes temperature dependent peaking in the converged-band regime. With ECMD and the Green-Kubo formula, the reduction in the lattice thermal conductivity (suppression of short- and long-range acoustic phonon transports) is also verified. The described thermal-disorder roles lead to high ZT, and in good agreement with the experimental results.

Chapter 4 proposes an unique structural ordering of a filler atom leading to multiphase scattering in the filled skutterudites, one of promising high-performance TE materials. Using the cluster expansion (CE) and the DFT, the solid-state phase diagram of $Ba_xCo_4Sb_{12}$ and several stable (ground-state) configurations of Ba ordering over the intrinsic voids are calculated. Their lattice thermal conductivity is greatly influenced by the topology of the filler species. The lattice thermal conductivity predicted using ECMD shows a minimum in the two-phase mixture regime, dominated by the significantly reduced long-range acoustic phonon transport.

In Chapter 5, substituting pnicogen rings of skutterudite crystals is suggested as tune and lower lattice thermal conductivity, a cage-breathing scattering. Based on DFT calculations, the substituted Ge atoms form the softest bonds in the compound acting as a pseudo-rattler with distinct mode-flattening features and a local phonon softener (comparable to rattlers in filled skutterudites). The collective modes of this lattice configuration induce the breathing mode in the cage which is highly correlated with the reduction in lattice thermal conductivity. The lattice thermal conductivity

predicted with non-equilibrium *ab-initio* molecular dynamics (NEAIMD) is in good agreement with the experimental results and the point-defect scattering model. We suggest that this new scattering mechanism can be combined with the conventional rattling mechanism, thus causing further reduction in lattice thermal conductivity in these hybrid structures.

Chapter 6 examines the anomalous temperature-independent behavior of the Seebeck coefficient and lattice thermal conductivity of $B_{13}C_2$ through the polaron and phonon evolutions observed using the first-principles calculations. The lattice dynamics analysis shows that the unique icosahedron structures dominate the optical phonon modes and C-B-C intericosahedral bonds dominate the local acoustic vibration. The temperature-induced Jahn-Teller distortion and the electron-phonon coupling in the icosahedron structures creating the small polarons (i.e., charge trapping and phonon softening) are identified. Using EAIMD and NEAIMD methods (including entropy and energy analyses), the Seebeck coefficient and its components, and the lattice thermal conductivity are predicted as a function of temperature and compared with experiments and good agreements are found. Softened and localized phonons make significant vibrational contribution to the Seebeck coefficient and allow for an amorphous-like lattice thermal conductivity.

In Chapter 7, comprehensive computational analyses of the phonon and electronic properties of the β-Cu_2Se and a few similar compounds (e.g., Cu_2Te), using the first principles. The temperature-dependent lattice dynamics show large interstitial displacement of the Cu^+ ions and a rather rigid Se framework. These results allows for significant suppression of the lattice thermal conductivity and weak temperature

dependence, $\sim T^{-0.3}$. We examine the roles of cations and anions such as Cu (or Ag) and Se (or Te) in the electronic TE properties. Then we suggest that the alloys of β-Cu_2Te and β-Cu_2Se are promising high ZT materials, since they have comparable electronic transport properties but reduced lattice thermal conductivity due to additional phonon scattering (e.g., mass fluctuation).

Chapter 8 summaries the highlights the findings of this study and proposes future directions for the related research.

Appendix A presents various contributions to the Seebeck coefficient through entropy analysis, phonon-softening, and charge-carrier interactions. The computational results for boron carbides provide examples of phonon softening effects on the Seebeck coefficient.

In Appendix B, the roles of various thermal energy carriers (i.e., electron, polaron, and lattice) in the total thermal conductivity $\kappa = \kappa_e + \kappa_{ep} + \kappa_L$ of UO_2 are treated and predicted. We show that the role of surface representing pores present in the common sintered-powder specimen used experiments, is the cause of the polaron formation. The predicted total thermal conductivity results are compared with the experiments and good agreement is found. With NEAIMD and ECMD simulations, we show that the long-range acoustic phonon transport dominates to high temperature ($T < 1500$ K) and the charge carriers (polarons and intrinsic electrons) contribute to the total thermal conductivity for $T > 1500$ K.

Chapter 2

Computational Methods

2.1 Overview

Understanding the roles of atomic structure and the thermal evolution of phonon and charge carriers would allow for the tuning of the TE properties for achieving superior TE figure-of-merit. Accurate description of the atomic structure is essential for predicting the behaviors of these carriers (their states and interaction mechanisms), and this is still changing and improving. These accurate predictions are now possible with advances in multiple time and length-scale [*ab-initio*, classical MD, Boltzmann (meso), and macro] treatments.

In this chapter, brief overview and description of the computational methods used in the later chapters are given. Figure 2.1 is a diagrammatic sketch of the overall computations performed in this work on the TE properties research, with a comparison with the equivalent conventional experiments on TE property characterizations. Each part will be explained in detail in the following sections.

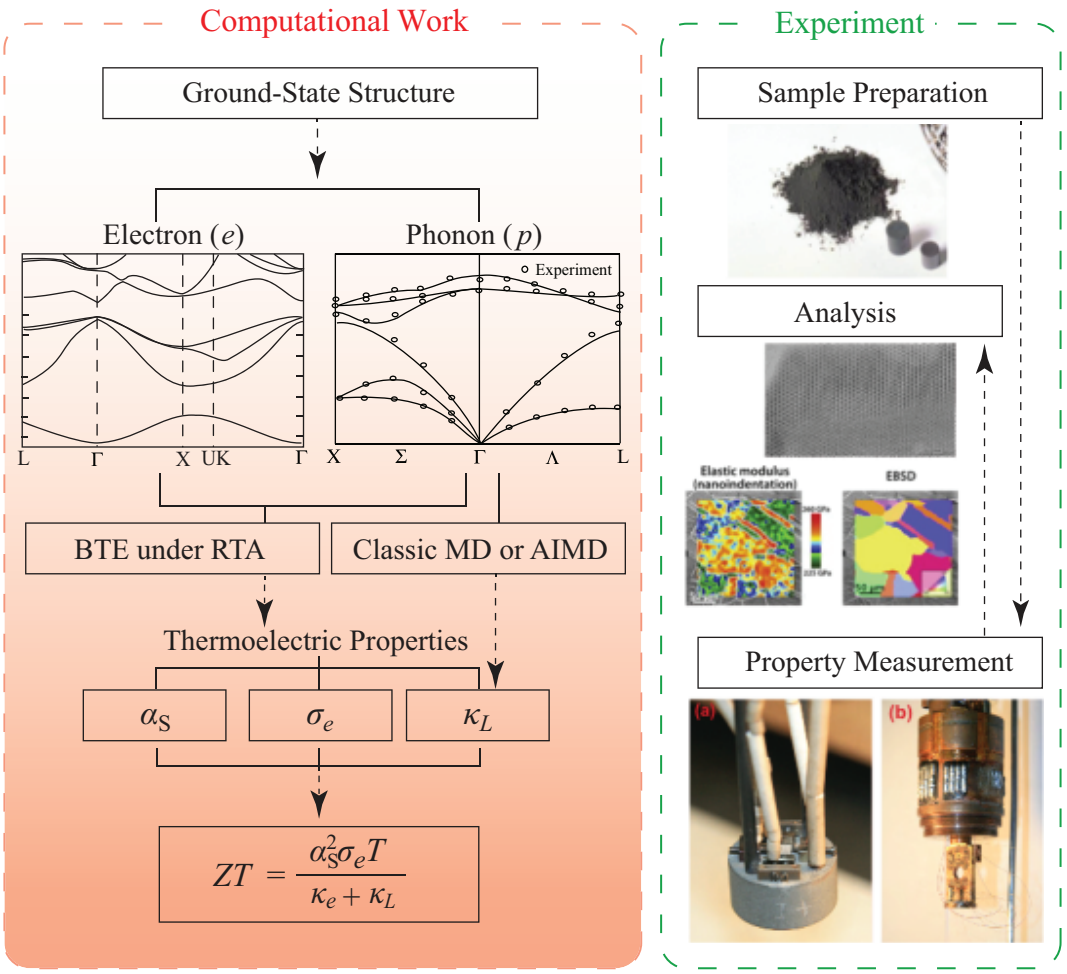

Figure 2.1: Diagram of overall calculation methodologies, from structure prediction to TE transport properties. Comparison between computational physics and experiments of TE research are also shown.

2.2 Structure Prediction and Electronic States

In order to mathematically describe the atomic configuration of the crystalline sublattice, the CE method is applied [173]. An occupation variable σ_i is used for the configurational variable, which takes a value 1 if the site has an occupant and -1 if it is vacant. The CE is constructed from this description, assuming an on-lattice Hamiltonian that can be expressed exactly as a series expansion of configurational basis functions of the form

$$E(\boldsymbol{\sigma}) = \sum_{\{\alpha\}} V_\alpha \Gamma_\alpha(\boldsymbol{\sigma}), \quad \Gamma_\alpha(\boldsymbol{\sigma}) = \prod_{i \in \alpha} \sigma_i, \tag{2.1}$$

where α denotes a cluster of sites (pairs, triplets and so forth, as well as lone sites), and all possible clusters of the sublattice sites are included in the sum. $\Gamma_\alpha(\sigma)$ represents the cluster basis function, which partially describes the occupancy state of the cluster α [173], and the coefficients V_α are the effective cluster interactions (ECI) that specify the contribution from each cluster. Many of the ECI are equivalent by crystal symmetry, and the series in Eq. (2.1) can be truncated to reflect the relatively small contribution from clusters comprised of many sites or those describing long length-scales.

To predict the total energy and the electronic states of (cluster-expanded) crystalline solid structures, the DFT, one of the most successful approaches (in both computing time cost and accuracy) is used. In fact, all matter and its physical and chemical phenomena are explained with the states and interaction of the nuclei

and electrons. So, for accurate description and prediction of matter, the quantum-mechanical methods, i.e., solving the Schrödinger's wave equations $\mathrm{H}\Psi = \mathrm{E}\Psi$, are the promising and fundamental (first principles) choice. In the beginning the era of this method (around 1930's), only the simple hydrogen-like atoms were dealt under limited conditions and accuracy. This followed by a long period where the underlying difficulties made it not possible for researchers to deal with real applications, e.g., the many-body problems. The breakthrough came with two important theorems (by P.C. Hohenberg, W. Kohn, L.J. Sham, *et al.*), the electron density $\rho(\boldsymbol{r})$ and the energy functional. The electron density $\rho(\boldsymbol{r})$ is

$$\rho(\boldsymbol{r}) = \sum_{i}^{N} |\phi_i(\boldsymbol{r})|^2, \tag{2.2}$$

where $\boldsymbol{r}$ is the position vector, ϕ is the electron states (or orbitals). The total (ground-state) energy $E_\circ$ is

$$\begin{aligned}
E_\circ &= E[\rho(\boldsymbol{r})] \\
&= E_{\mathrm{KE}}[\rho(\boldsymbol{r})] + E_{\mathrm{ext}}[\rho(\boldsymbol{r})] + E_{\mathrm{H}}[\rho(\boldsymbol{r})] + E_{\mathrm{XC}}[\rho(\boldsymbol{r})], \\
&= E_{\mathrm{KE}}[\rho(\boldsymbol{r})] + E_{\mathrm{eff}}[\rho(\boldsymbol{r})], \\
&= -\frac{\hbar^2}{2m}\sum_{i=1}^{N}\int \mathrm{d}\boldsymbol{r}\phi_i^*(\boldsymbol{r})\nabla^2\phi_i(\boldsymbol{r}) + \int \mathrm{d}\boldsymbol{r}V_{\mathrm{ext}}(\boldsymbol{r})\rho(\boldsymbol{r}) + \\
&\quad \frac{e_c^2}{2}\int \mathrm{d}\boldsymbol{r}\int \mathrm{d}\boldsymbol{r'}\frac{\rho(\boldsymbol{r})\rho(\boldsymbol{r'})}{|\boldsymbol{r}-\boldsymbol{r'}|} + \int \mathrm{d}\boldsymbol{r}\frac{\partial E_{\mathrm{XC}}[\rho(\boldsymbol{r})]}{\partial\rho(\boldsymbol{r})}\rho(\boldsymbol{r}),
\end{aligned} \tag{2.3}$$

where e_c is the electron charge, V_{ext} is the external potential (for a crystalline solid, the V_{ext} is simplified with the ionic interaction between nuclei and electrons, $V_{\mathrm{ext}} =$

V_{ion}). To determine the ground-state energy, above total energy functional, Eq. 2.3 should be minimized. At the energy functional minimum, the energy states ϕ_i are self-consistent solutions of the Kohn-Sham equations,

$$[-\frac{\hbar^2}{2m}\nabla^2 + V_{\text{ion}}(\boldsymbol{r}) + V_{\text{H}}(\boldsymbol{r}) + V_{\text{XC}}(\boldsymbol{r})]\phi_i(\boldsymbol{r}) = \varepsilon_i\phi_i(\boldsymbol{r}), \tag{2.4}$$

where ε_i is the Kohn-Sham eigenvalue associated with electronic state i, V_{H} is the Hartree potential of electrons, V_{XC} is the exchange-correlation functional. Depending on the system, one of approximate expressions of the exchange-correlation energy [i.e., local (LDA), semi-local (GGA, GGA-PW91, GGA-PBE), semi-nonlocal (meta-GGA), and hybrid (B3LYP)] can be choused. Nowadays, DFT method is capable of treating a few thousand atoms with very good accuracy and efficiency. Comparing with the classical MD, to generate good (empirical) interatomic potential has been always one of fundamental questions. In the DFT formalism, it do not depend on any external parameters (except given atomic numbers) although determining or constructing a good XC functional is important on results.

This DFT calculation is also applied to parameterize the ECI and determine the truncation of the series. Calculations is performed using the Vienna *ab-initio* Simulation Package (`VASP`) [116] within the Perdew-Burke-Ernzerhof (PBE) parameterization of the generalized gradient approximation (GGA) for exchange and correlation [154] and using the projector augmented wave (PAW) method [26, 117]. Truncation of the CE is performed using a genetic fitting method [88] to optimize the leave-one-out cross-validation (CV) score. Starting from the predicted ground-states, ensemble av-

erage quantities can be obtained from Monte Carlo (MC) using the cluster expanded Hamiltonian. Integration of these quantities permits the determination of the free energies, which can be used to construct a phase diagram of the configurational order on the crystalline sublattice.

2.3 Lattice Dynamics and Phonon Properties

As shown in Fig. 2.2, two different methods are used to predict the lattice dynamics and phonon properties. Starting with the ground-state structure confirmed with the computation (CE-DFT and MC in Section 2.3) or experiments, to model/simulate phonons in crystalline solids is possible with the empirical potential or DFT. Here, the DFT-based phonon calculation (i.e., finite displacement method) is focused and the ECMD (i.e., the Fourier transform of the velocity autocorrelation function) is used only for the high-temperature predictions.

The total energy of a system $E_\circ$ is

$$E_\circ = E[\boldsymbol{r}(\nu_1, \lambda_1), \cdots, \boldsymbol{r}(\nu_n, \lambda_N)], \tag{2.5}$$

where $\boldsymbol{r}(\nu, \lambda)$ is the point of the ν-th atom in the λ-th unit cell and n and N are the number of atoms in a unit cell and the number of unit cells. The force F and force constant Γ_{ij} are

$$F_i(\nu, \lambda) = -\frac{\partial E_\circ}{\partial r_i(\nu, \lambda)}, \tag{2.6}$$

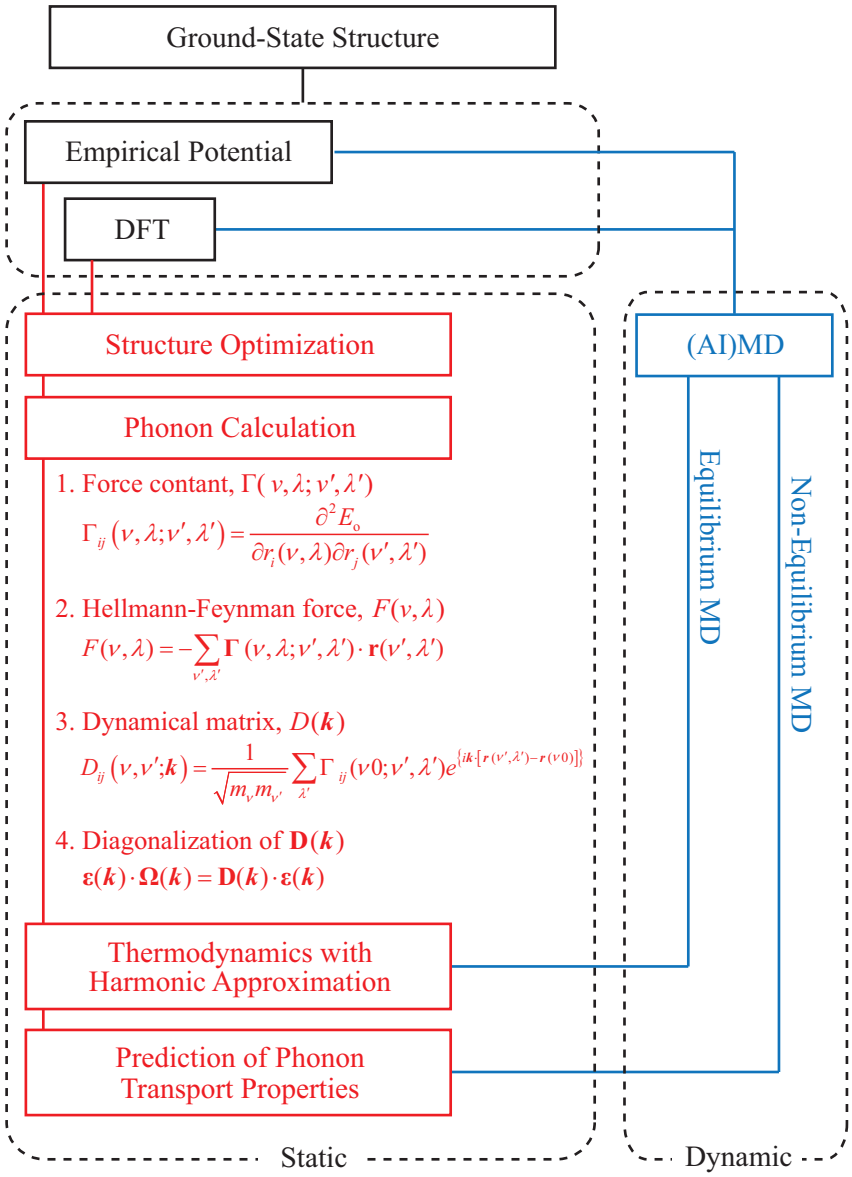

Figure 2.2: Diagram of lattice dynamics and phonon calculation including static and dynamic approaches. Important equations used in phonon calculation are also shown.

and

$$\Gamma_{ij}(\nu,\lambda;\nu',\lambda') = \frac{\partial^2 E_\circ}{\partial r_i(\nu,\lambda)\partial r_j(\nu',\lambda')} = -\frac{\partial F_j(\nu',\lambda')}{\partial r_i(\nu,\lambda)}, \tag{2.7}$$

where i (or j) is the Cartesian index, ν (or ν') is the index of atoms in a unit cell, and λ (or λ') is the index of unit cell. In finite displacement method, the force constant is approximated as

$$\Gamma_{ij}(\nu,\lambda;\nu',\lambda') \simeq -\frac{F_j(\nu',\lambda';\Delta x_i(\nu,\lambda)) - F_j(\nu',\lambda')}{\Delta r_i(\nu,\lambda)}, \tag{2.8}$$

where $F_j(\nu',\lambda';\Delta r_i(\nu,\lambda))$ is the force on atom with a finite displacement $\Delta r_i(\nu,\lambda)$ and usually $F_j(\nu',\lambda') = 0$. The dynamical matrix is

$$D_{ij}(\nu,\nu';\boldsymbol{k}) = \frac{1}{\sqrt{m_\nu m_{\nu'}}} \sum_{\lambda'} \Gamma_{ij}(\nu 0;\nu',\lambda')\exp\{i\boldsymbol{k}\cdot[\boldsymbol{r}(\nu',\lambda') - \boldsymbol{r}(\nu 0)]\}, \tag{2.9}$$

where m is the atomic mass and $\boldsymbol{k}$ is the wave vector. The equation of motion is given as

$$\sum_{\nu' j} D_{ij}(\nu,\nu';\boldsymbol{k})\varepsilon_j(\nu';\boldsymbol{k}\alpha) = m_\nu[\omega(\boldsymbol{k}\alpha)]^2\varepsilon_i(\nu;\boldsymbol{k}\alpha), \tag{2.10}$$

where ε is the eigenvalue and α is the band index of wave vector $\boldsymbol{k}$. Applying the diagonalization of $\mathbf{D}(\boldsymbol{k})$, phonon frequency ($\omega$) is obtained by

$$[\omega(\boldsymbol{k}\alpha)]^2\delta_{\mathrm{D},\alpha\alpha'} = \sum_{\nu i\nu' j} \varepsilon_i(\nu;\boldsymbol{k}\alpha)^* D_{ij}(\nu,\nu';\boldsymbol{k})\varepsilon_j(\nu';\boldsymbol{k}\alpha). \tag{2.11}$$

The static (or frozen) lattice dynamics and phonon properties of crystalline structure is calculated with various DFT calculations implemented in the `VASP` [116]

and PHONON [151] codes. The PBE parameterization of the GGA for the exchange-correlated functional [154] and the PAW method for modeling core electrons [26, 117] are generally used. All phonon and thermodynamic properties are predicted using fits of interatomic force constant tensors to the calculated Hellmann-Feynman (HF) forces. The total energy and HF forces are found starting from the fully-relaxed configuration, such that initial ionic forces were less than 10^{-5} eV/Å. Ionic displacements of 0.03 Å of each atom were sampled along all three directions. Diagonalization of the dynamical matrix yields the phonon dispersion curves, density-of-states (D_p), and many thermodynamic properties (e.g., atomic displacement, free energy, entropy, heat capacity, and internal energy) under the harmonic approximation.

The dynamic (or high-temperature) lattice dynamics and phonon properties are investigated by the atomic trajectories obtained from ECMD or EAIMD. The temperature-dependent phonon density-of-states are also obtained from EAIMD and the Fourier transform of the velocity autocorrelation function over enough time (at least 20 ps) and reasonable time-steps ($\sim$ 1 fs). MD simulations are performed on supercells prepared with enough atoms and thermally-expanded lattice parameters.

2.4 Coupling Effects of Electron and Phonon

The electron-phonon (*e-p*) interaction plays a central role in a variety of physical phenomena, including superconductivity, Peierls instability, and polaronic transport [105, 124]. The *e-p* coupling parameter is calculated from the self-consistent change in the potential of electrons interacting with a phonon mode with norm-conserving

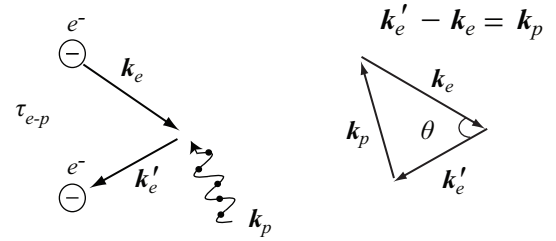

Figure 2.3: Scattering of a plane electron wave in a crystal demonstrating the electron-phonon interaction.

pseudopotential and a plane-wave cutoff energy. Fully-relaxed structures are simulated with an electron-momentum mesh and a phonon-momentum mesh grid. The *e-p* coupling parameter is calculated from the self-consistent change in the potential of electrons interacting with a phonon mode [75]. Here the *e-p* interaction matrix $M^{i,j,\nu}_{\boldsymbol{k'_e},\boldsymbol{k_e}}$ is

$$M^{i,j,\nu}_{\boldsymbol{k'_e},\boldsymbol{k_e}} = (\frac{\hbar}{2m\omega^{i,j}_{\boldsymbol{k_e},\boldsymbol{k'_e}}})^{1/2}\langle\psi^j_{\boldsymbol{k'_e}} \mid \delta\varphi^\nu_{\boldsymbol{k_p}} \mid \psi^i_{\boldsymbol{k_e}}\rangle, \tag{2.12}$$

where $\delta\varphi^\nu_{\boldsymbol{k_p}}$ is the phonon perturbation for a particular mode, and ψ is the wavefunction, $\boldsymbol{k_e}$ and $\boldsymbol{k'_e}$ are electron wave vectors with band indices i and j. $\boldsymbol{k_p}$ is phonon wave vectors with the mode number ν. This *e-p* matrix is a basic quantity giving the probability of electron scattering from an initial electron state with momentum $\boldsymbol{k_e}$ to a final electron state by a phonon with momentum $\boldsymbol{k_p}$ and mode index ν (Figure 3.3). Once the matrix elements are determined, the corresponding *e-p* scattering rate $\dot{\gamma}$ can be obtained by using the Fermi's golden rule [105]. This transition rate is represented in terms of the interaction matrix $M^{i,j,\nu}_{\boldsymbol{k'_e},\boldsymbol{k_e}}$ as

$$\begin{aligned}\dot{\gamma}(\text{initial} \to \text{final}) &= \frac{2\pi}{\hbar}|\langle\psi_{\text{final}}|\mathrm{H}_{e-p}|\psi_{\text{initial}}\rangle^2\delta_{\mathrm{D}}(E_f - E_i \mp \hbar\omega^\nu_{\boldsymbol{k_p}}) \\ &= \frac{2\pi}{\hbar}|M^{i,j,\nu}_{\boldsymbol{k'_e},\boldsymbol{k_e}}|^2\delta_{\mathrm{D}}(E^j_{\boldsymbol{k'_e}} - E^i_{\boldsymbol{k_e}} \mp \hbar\omega^\nu_{\boldsymbol{k_p}}),\end{aligned} \tag{2.13}$$

where δ_{D} is the Dirac-delta function. Here the - and + signs in the delta function with electron energies correspond to a phonon emission and absorption, respectively. Very often the energy change of the scattered electron due to the absorption or emission of a phonon is neglected because the scale of phonon energy is generally much smaller than that of electron energy.

The Eliashberg spectral function $\alpha^2F(\omega)$ is defined as the sum over contribution to the coupling from each phonon mode, [29, 36, 157]

$$\alpha^2F(\omega) = \frac{1}{D_e(E_{\mathrm{F}})} \sum_{\boldsymbol{k_e},\boldsymbol{k'_e},\boldsymbol{k_p}} |M^{i,j,\nu}_{\boldsymbol{k'_e},\boldsymbol{k_e}}|^2 \delta_{\mathrm{D}}(E^i_{\boldsymbol{k_e}}) \delta_{\mathrm{D}}(E^j_{\boldsymbol{k'_e}}) \delta_{\mathrm{D}}(\omega - \omega^\nu_{\boldsymbol{k_p}}), \tag{2.14}$$

where $D_e(E_{\mathrm{F}})$ is the density-of-states per atom and spin at the Fermi level (E_{F}).

2.5 TE Transport Properties

The TE energy conversion between heat and electrical power is evaluated by the conversion efficiency of TE system, ZT [Eq. (1.1)]. Based on the electron and phonon states of a system (see Fig. 2.1), all TE transport properties are predicted as below.

2.5.1 Electronic transport properties

The Onsager transport relation states that every flux j_i of quantity i within a system is given by the linear combination of each driving forces F_j,

$$j_i = \sum_j L_{ij} F_j, \tag{2.15}$$

where L_{ij} are the coupling transport coefficients. For the TE system, the electrical and heat flux are given in terms of the macroscopic gradients (i.e., electric field and temperature gradient) with coupling tensors. The electronic TE properties such as α_{S}, σ_e, and κ_e, are derived from the Onsager transport relation and the Boltzmann transport equation (BTE) with energy and temperature-dependent relaxation time $\tau_e(E_e,T)$ [3, 23, 89, 105, 106, 152, 156, 162, 206] as follows:

The differential electrical conductivity $\sigma_{d,e,\alpha}(E_e)$ is [148, 176]

$$\sigma_{d,e,\alpha}(E_e) = e_c^2 \tau_e(E_e) v_{e,\alpha}^2(E_e) D_{e,\alpha}(E_e)(-\frac{\partial f_e^\circ}{\partial E_e}), \tag{2.16}$$

where E_e is the electron energy, τ_e is the relaxation time, $v_{e,\alpha}$ is the group velocity, f_e° is the Fermi-Dirac equilibrium distribution, and $D_{e,\alpha}$ is the electronic density-of-states. Here $v_{e,\alpha}$ is given by

$$v_{e,\alpha} = \{\frac{2}{m_{i,e,\alpha}} \gamma_\alpha(E_e)[\frac{\mathrm{d}\gamma_\alpha(E_e)}{\mathrm{d}E_e}]^{-2}\}^{1/2}, \tag{2.17}$$

and $D_{e,\alpha}(E_e)$ is given by

$$D_{e,\alpha}(E_e) = \frac{2^{1/2} m_{i,e,\alpha}^{3/2}}{\pi^2 \hbar^3} \gamma_\alpha(E_e)^{1/2}[\frac{\mathrm{d}\gamma_\alpha(E_e)}{\mathrm{d}E_e}], \tag{2.18}$$

where $m_{i,e,\alpha}(T)$ is the temperature-dependent density-of-states effective mass at α point, $\gamma_{\mathrm{L}}(E_e) = E_e(1 + E_e/\Delta E_{e,g,\mathrm{L}})$ for the non-parabolic bands, while $\gamma_\Sigma(E_e) = E_e$

for the parabolic band [3, 23, 87, 156, 206]. The carrier concentration n_i is

$$\begin{aligned} n_i &= \int_{E_{\rm CBM}}^{\infty} D_{e,{\rm C}}(E_e) f_e^{\circ}(E_e) {\rm d}E_e - \{ \int_{-\infty}^{E_{\rm VBM,L}} D_{e,{\rm L}}(E_e)[1 - f_e^{\circ}(E_e)] {\rm d}E_e \\ &+ \int_{-\infty}^{E_{\rm VBM,\Sigma}} D_{e,\Sigma}(E_e)[1 - f_e^{\circ}(E_e)] {\rm d}E_e \}. \end{aligned} \tag{2.19}$$

The electrical conductivity σ_e is

$$\sigma_{e,\alpha} = \int_0^{\infty} \sigma_{d,e,\alpha}(E_e) {\rm d}E_e \quad \text{and} \quad \sigma_e = \sum_{\alpha} \sigma_{e,\alpha}. \tag{2.20}$$

The Seebeck coefficient $\alpha_{\rm S}$ is

$$\alpha_{{\rm S},\alpha} = \frac{1}{e_c T} [\frac{\int_0^{\infty} \sigma_{d,e,\alpha}(E_e)(E_e - E_{\rm F}) {\rm d}E_e}{\int_0^{\infty} \sigma_{d,e,\alpha}(E_e) {\rm d}E_e}] \quad \text{and} \quad \alpha_{\rm S} = \frac{\sum_{\alpha} \alpha_{{\rm S},\alpha} \sigma_{\alpha}}{\sum_{\alpha} \sigma_{\alpha}}. \tag{2.21}$$

The electronic thermal conductivity κ_e is

$$\begin{aligned} \kappa_{e,\alpha} &= \frac{1}{e_c^2 T} \{ \int_0^{\infty} \sigma_{d,e,\alpha}(E_e)(E_e - E_{\rm F})^2 {\rm d}E_e - \frac{[\int_0^{\infty} \sigma_{d,e,\alpha}(E_e)(E_e - E_{\rm F}) {\rm d}E_e]^2}{\int_0^{\infty} \sigma_{d,e,\alpha}(E_e) {\rm d}E_e} \} \\ &\text{and} \quad \kappa_e = \sum_{\alpha} \kappa_{e,\alpha}. \end{aligned} \tag{2.22}$$

In the DFT-based electronic transport calculations, the crystal structure and eigen-energies obtained from DFT (i.e., `VASP` of `WIEN2k` platform) are employed in the `BoltzTraP` code. Within the Boltzmann transport theory the temperature- and doping-level-dependent conductivity $\sigma_e(T, \mu_e)$ and the Seebeck coefficient $\alpha_{\rm S}(T, \mu_e)$

are given by

$$\sigma_{e,\alpha\beta}(T,\mu_e) = \frac{1}{V}\int \sigma_{e,\alpha\beta}(E_e)[-\frac{\partial f_e^{\circ}(T,E_e)}{\partial E_e}]\mathrm{d}E_e, \tag{2.23}$$

$$\alpha_{\mathrm{S},\alpha\beta} = \sum_{\gamma}(\sigma_e^{-1})_{\alpha\gamma}\nu_{e,\beta\gamma}, \tag{2.24}$$

with

$$\nu_{e,\alpha\beta}(T,\mu_e) = \frac{1}{e_c TV}\int \sigma_{e,\alpha\beta}(E_e)(E_e-\mu_e)[-\frac{\partial f_e^{\circ}(T,E_e)}{\partial E_e}]\mathrm{d}E_e, \tag{2.25}$$

where μ_e is the chemical potential. The energy projected conductivity tensor is

$$\sigma_{e,\alpha\beta}(E_e) = \frac{1}{N}\sum_{i,\boldsymbol{k}} e_c^2\tau_{e,i,\boldsymbol{k}}v_{e,\alpha}(i,\boldsymbol{k})v_{e,\beta}(i,\boldsymbol{k})\frac{\delta(E_e-E_{e,i,\boldsymbol{k}})}{\mathrm{d}E_e}, \tag{2.26}$$

where i is the band index, N is a normalization depending on the number of k-points sampled in the Brillouin zone, and $v_{e,\alpha}(i,\boldsymbol{k})$ is the i component of band velocity $\nabla_{\boldsymbol{k}}E_e(\boldsymbol{k})$.

2.5.2 Lattice thermal conductivity

The ECMD with Green-Kubo formula are one of the well-known techniques to predict lattice thermal conductivity. In general, ECMD presents the behavior of a group of atoms by solving Newton's 2nd law of motion for the atoms with a given set of empirical potentials. With the derivation from M.S. Green [83] and R. Kubo [118], a formalism that linear transport coefficients are related to the time dependence of equilibrium fluctuations in the conjugate flux [134], lattice thermal conductivity is given with the heat current autocorrelation function (HCACF) decay [99, 105, 111,

133, 134], i.e.,

$$\kappa_L = \frac{V}{k_{\mathrm{B}}T^2}\int_0^\infty \frac{\langle \boldsymbol{q}(t)\cdot\boldsymbol{q}(0)\rangle}{3}\mathrm{d}t, \tag{2.27}$$

where t is time, and $\langle \boldsymbol{q}(t)\cdot\boldsymbol{q}(0)\rangle$ is the HCACF. The heat current vector ($\boldsymbol{q}$) is given by

$$\boldsymbol{q} = \frac{1}{V}\frac{\mathrm{d}}{\mathrm{d}t}\sum_i E_i\boldsymbol{r}_i = \frac{1}{V}[\sum_i E_i\boldsymbol{u}_i + \frac{1}{2}\sum_{i,j}(\boldsymbol{F}_{ij}\cdot\boldsymbol{u}_i)\boldsymbol{r}_{ij}], \tag{2.28}$$

where E_i, $\boldsymbol{r}_i$, and $\boldsymbol{u}_i$ are the energy, position, and velocity vectors of particle i, and $\boldsymbol{r}_{ij}$, and $\boldsymbol{F}_{ij}$ are the interparticle separation and force vectors between particle i and j. The resultant HCACFs were then directly integrated and the κ_L was set as the average value in the stable regime of the integral.

Non-equilibrium (or direct) method is another computational technique to predict lattice thermal conductivity. Here, it is derived from the law of heat conduction (i.e., Fourier's law), the time rate of heat transfer is proportional to the negative gradient in the temperature and to the area [105, 106]. The lattice thermal conductivity using NEAIMD is computed as the ratio of an applied heat flux to the resulting temperature gradient [190, 207],

$$\kappa_L = -[\overline{Q(t)}/A](\overline{\mathrm{d}T/\mathrm{d}x})^{-1}, \tag{2.29}$$

where the overbar designate the time average, $Q(t)$ is the heat flux, and A is the cross-sectional area of a simulation cell. As shown in Fig. 2.4, the heat flux is imposed by dividing the simulation cell into sections of equal width, and exchanging kinetic energy between hot and cold sections. The temperature gradient along the x axis is computed from the mean temperature of adjacent sections. For simulations we use the

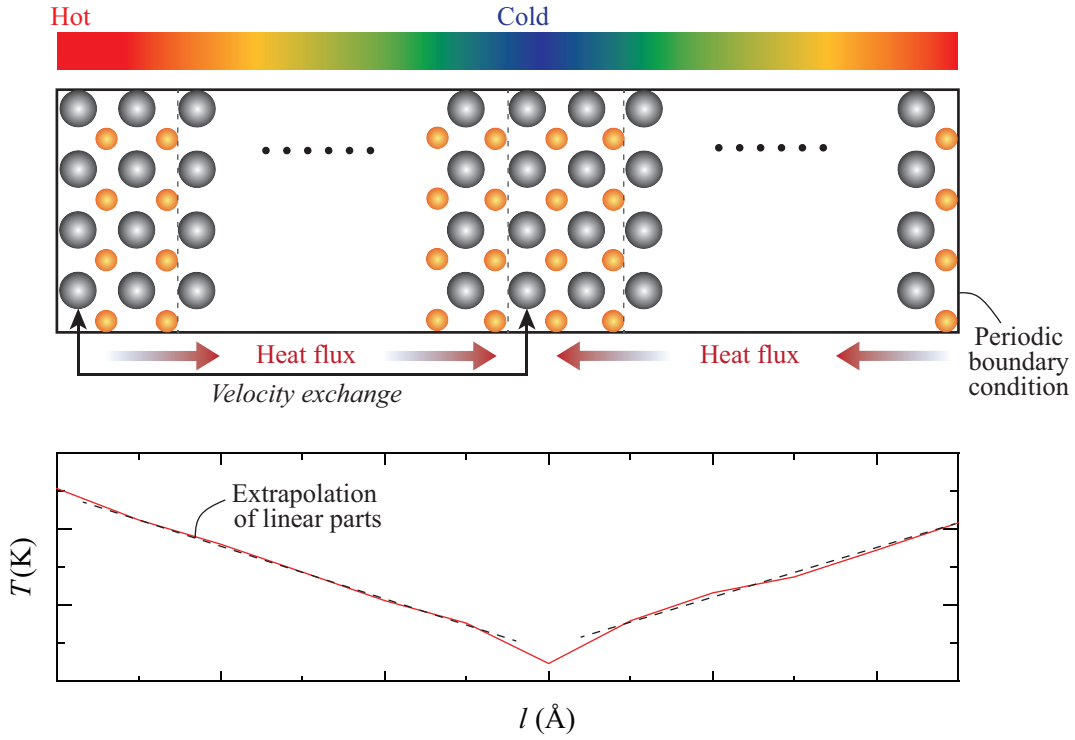

Figure 2.4: Schematic illustration of the simulation box for the NEAIMD. Periodic boundary conditions are applied for all boundaries. The corresponding temperature profile in a specific direction is also shown.

VASP code modified to perform NEAIMD-energy exchange [103, 142] as reported in [190, 207]. Because the exchange of kinetic energy results in non-Newtonian dynamics in the hot and cold sections, only the linear portion of the temperature gradient is considered in calculating the lattice thermal conductivity.

2.6 Summary

Computational approaches offer a range of complementary insights. We have developed systematic and balanced (accuracy and computation-time cost) computational methods for predicting the ground-state structure, and the electron and phonon properties. In TE (coupled carrier transport and multicomponent systems), computational methods are contributing more than ever to the development of new, superior TE materials and their applications.

Chapter 3

Roles of Thermal Disorder in Lead Tellurides

3.1 Introduction

Thermoelectricity allows for direct conversion of heat into electrical power with significant potential for power generation. Lead telluride (PbTe), a chalcogenide with simple rocksalt structure (space group $Fm\bar{3}m$, see Fig. 3.1), is a well-known mid-temperature TE material for power generation [145, 152, 186]. Its recent studies as a high-ZT material has shown (i) resonant-state enhancement of the Seebeck effect [2, 92], (ii) reduced thermal conductivity using embedded nanostructures [24, 76, 89], and (iii) band convergence by dopant tuning [152, 153]. In addition, there have been experimental and theoretical studies of its anharmonic lattice dynamics (ferroelectric instability) [31, 48, 223], however, this has not been related to its electronic band convergence and TE properties. In this chapter, we examine the thermal disorder

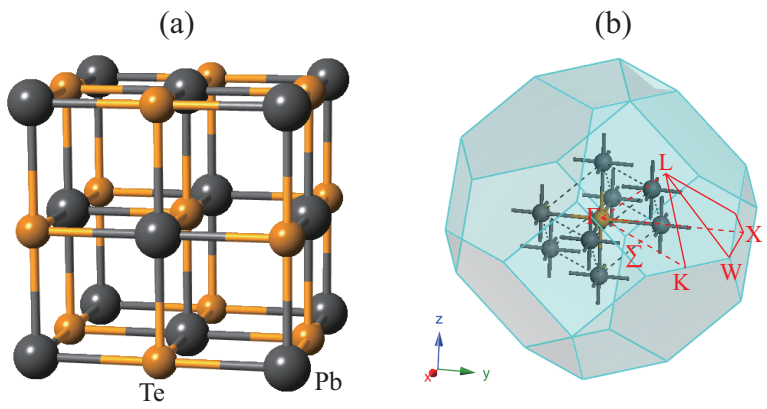

Figure 3.1: The crystal structure of PbTe. (a) Conventional cell of PbTe showing simple cubic structure. (b) The first Brillouin zone for the primitive cell of PbTe and its high symmetry k-points.

caused PbTe electronic band convergence, using first-principles calculations (including EAIMD) and investigate the roles of disorder and convergence in the charge- and phonon-related TE properties.

PbTe has octahedral coordination (rocksalt structure, see Fig. 3.1) and its lattice dynamics manifests high degree of anharmonicity [31, 140, 145, 223]. This reduces the phonon conductivity [48, 140]. In the thermal-disordered structure of Pb compounds, the Pb atoms are moved further off-centered compared to the chalcogen atoms, with the following trend among dislocation of compounds: PbS $<$ PbSe $<$ PbTe. Based on these, the origin of low thermal conductivity of PbTe has been explained [48, 140, 223]. The abnormal temperature-dependent bandgap energy (i.e., increase with increase in temperature) has also been explained by lattice dynamics using the Debye-Waller factor calculations (larger Pb displacements compared to Te) [108]. In comparison, studies of band convergence in PbTe are very limited. Although the existence of a second valence band edge was first proposed by Allgaier [6] based on the temperature

dependence of the Hall effect, no exact physical explanation or direct evidence of the band convergence of PbTe has yet been reported [182]. However, recent studies of band convergence and its analytic model have pointed to improved TE properties in PbTe [24, 153]. A three-band model accounts for the non-parabolicity and anisotropy of the conduction-band and the valence-band at L <111> points using the Kane model, while using the parabolic and isotropic behavior for the secondary valence-band along the Σ <110> direction [8, 87, 153, 162, 206].

3.2 Calculation Methods

3.2.1 Thermal-disordered structures from EAIMD

We investigate the high-temperature behavior of PbTe structure by obtaining the thermal-disordered structure of PbTe using EAIMD with the `VASP` code [116], i.e., we find with increase in temperature anharmonic lattice vibration distort crystal symmetry and in turn the electrons respond to the displaced ionic positions. Using the Born-Oppenheimer approximation, the atomic positions and velocities are updated with the Verlet algorithm. The forces on ions at each configuration are used to update the ionic positions at an elapsed time step and we iterate to calculate the trajectory of the system. The EAIMD simulations are performed on supercells consisting 54-atoms ($3\times3\times3$ primitive cells) and 64-atoms ($2\times2\times2$ conventional cells) along with and the PAW-based DFT (also used for the static calculations) [26]. Considering thermal expansion with temperature changes, we prepare the PbTe supercells with experimental

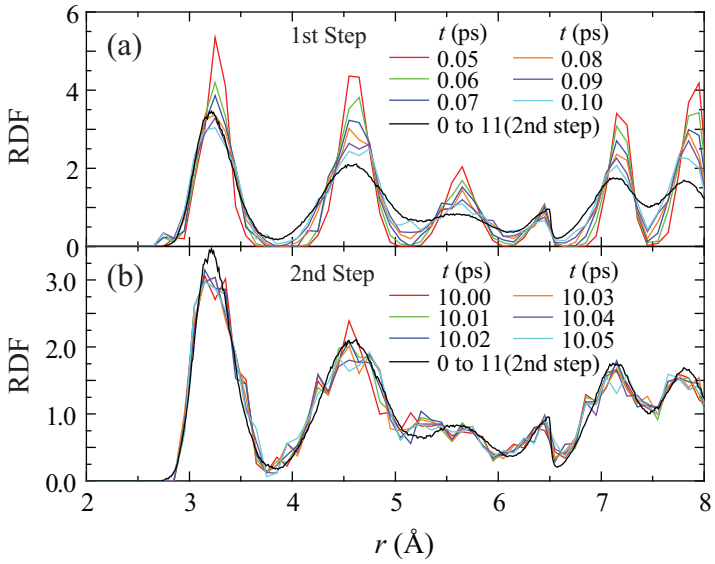

Figure 3.2: Time-dependent radial distribution function evolutions of PbTe supercell at $T = 700$ K. Each snapshot is average of 64 displaced coordinates obtained from (a) initial, and (b) a well-converged EAIMD step. Average radial distribution functions of all snapshots (2nd step, 0 to 11 ps) are also shown.

results for thermally-expanded lattice parameter, $a(T) = 6.422 + (0.9546\times10^{-4})T + (2.615\times10^{-8})T^2$ for 293 to 973 K [205]. The proper cell volume at each temperature is locked during EAIMD calculations. The Brillouin zone is sampled at only the gamma point. We carry out constant-temperature simulations using Nosé thermostat for 6 ps (0.2 fs time steps). After reaching equilibrium using a NVT ensemble, another calculation is performed for 11 ps (1 fs time steps), and we find good energy convergence and temperature stability. During EAIMD calculations, the Fermi-Dirac smearing factor ($k_{\mathrm{B}}T$, where k_{B} is the Boltzmann constant) for each temperature was also applied to ensure reliable thermal-disordered atomic coordinates. Finally, all temperature-dependent atomic coordinates are obtained from EAIMD snapshots at each temperature.

To verify the snapshots are represent stable structures and motion, we addressed

the statistical uncertainty. As noted above, two step approach is used to find a stable snapshot. As shown in Fig. 3.2, we find our second step simulations are fully relaxed and it provides energy-converged structures with low statistical uncertainty. Every snapshot is average of 64 displaced coordinates of PbTe and is used in the calculations of the transport properties. (The error bars of the atomic displacement of each atom will be shown in Fig. 3.3, indicate the statistical uncertainty.) These verification processes are used to ensure shots are indeed representative.

3.2.2 Electronic structures and transport properties

Our electronic calculations employs the full-potential linearized augmented plane-wave method [183] as implemented in the `WIEN2k` code [25]. We calculate all TE transport properties of thermal-disordered p-type PbTe using `WIEN2k` and `BoltzTraP` [127] codes, and a ECMD code written for this problem. All PbTe transport properties are calculated from the common DFT band energies (0 K). However, those DFT band energies obtained from thermally-disordered structure (EAIMD snapshots at each temperature) and the Fermi-Dirac smearing factors are also used in the transport-property calculations. We expect/show these two temperature effects (atomic configurations and smearing) are sufficient to illustrate the abnormal changes of PbTe properties with temperature. The muffin-tin radii are chosen to be 2.5 a.u. for all atoms. The plane-wave cutoff $Rk_{\max} = 7.0$ suffices for good convergence. Due to the large atomic masses (Pb and Te), spin-orbit interaction is included for the relativistic effects. Convergence of the self-consistent calculation cycle is performed

using 2769 (for frozen structure) and 36 (for high-temperature structure) k-points inside the reduced Brillouin zone to within 0.0001 Ry with a cut-off of -6.0 Ry between the valence and the core states. Since TE transport properties are sensitive to band structures near the Fermi surface, we use the Engel-Vosko generalized gradient approximation to avoid the underestimation of bandgap energy (a well-known problem with DFT calculations) [67]. The spin-orbit interaction is also included for the relativistic effects. In the transport calculations, the original k-mesh is interpolated onto a mesh five times as dense and the eigenenergies are found with `BoltzTraP` code. Within the Boltzmann transport theory the temperature- and doping-level-dependent conductivity $\sigma_e(T, \mu_e)$ and the Seebeck coefficient $\alpha_{\mathrm{S}}(T, \mu_e)$ are given in Section 2.5.1 [see Eqs. (2.23), (2.24), (2.25), and (2.26)].

3.2.3 ECMD and lattice thermal conductivity calculations

Previous lattice thermal conductivity results of PbTe using classic MD [42, 159] are limited and require special attention due to the strong anharmonic coupling effects [48]. Using atomic substitutions [42] and various vacancy configurations [159], reduced lattice thermal conductivity of PbTe has been predicted using classical MD. In order to consider the anharmonic behaviors of PbTe structures, we use the thermal-disordered configurations (from EAIMD) and the potential models appropriate for the covalent and rigid-ionic bonds. For these bonds, we use the Morse and the three-cosine interatomic potentials with effective ionic charges [223], parameterized for two-body

Table 3.1: The Morse and the three cosine interatomic potential parameters for PbTe. The effective atomic charges of Pb and Te are 0.72 and -0.72 [223], respectively.

Two-body	$\varphi_\circ$ (eV)	a (1/Å)	$r_\circ$ (Å)	Three-body	φ_θ (eV)	$\theta_\circ$ (°)
Pb-Te	0.465	0.863	3.68	Te-Pb-Te	0.680	90.0
Te-Te	0.394	1.51	4.22			

(Pb-Te and Te-Te) and three-body (Te-Pb-Te) interactions, i.e.,

$$\varphi(r_{ij}) = \varphi_\circ\{[1 - \exp(-a(r_{ij} - r_\circ))]^2 - 1\}, \tag{3.1}$$

$$\varphi(\theta_{ijk}) = (1/2)\varphi_\theta(\cos\theta_{ijk} - \cos\theta_\circ)^2, \tag{3.2}$$

where $\varphi_\circ$, r_{ij}, and θ are the dissociation energy, interatomic separation distance, and bond angle. The parameters $\varphi_\circ$, r_{ij}, and θ are determined by fitting to both the *ab-initio* calculated total energy and the experimental elastic constants. Utilizing a multi-variable fitting procedure in the `GULP` code [72], we obtain the parameters listed in Table 3.1. The fitted pair potential undergo `GULP` optimization of the crystal structure under constant pressure. All related thermo-mechanical properties (e.g., elastic constants, bulk modulus, shear modulus, the Grüneisen parameter, and thermal expansion coefficient) are listed in Table 3.2 and compared with the reported experiments with good agreements.

The ECMD with the Green-Kubo formalism is used for the prediction of lattice thermal conductivity κ_L. It is expressed with HCACF decay equation and heat current vector [99, 105, 111, 133, 134], Eqs. (2.27) and (2.28). Details are given in Section 2.5.2. After checking the size effect of ECMD, average are found over all three directions for a system consisting of 8×8×8 conventional unit cells (4096

Table 3.2: Comparison of bulk mechanical properties found from the interatomic potentials with those from experiments. C_{ij}, B, G, γ_{G}, and α are elastic constants, bulk modulus, shear modulus, Grüneisen parameter, and thermal expansion coefficient.

	C_{11} (GPa)	C_{12} (GPa)	B (GPa)	G (GPa)	γ_{G}	α (10^{-5}/K)
Reference [96]	128.1	4.4	-	-	-	-
Reference [57]	105.3	7.0	39.8	21.4	-	-
Reference [5]	108.0	7.7	41.1	-	-	-
Reference [208]	-	-	-	-	1.45	-
Reference [60]	-	-	-	-	-	1.8
This work	108.0	7.5	41.0	21.0	1.66	1.78

atoms). The Verlet leapfrog algorithm with the Nosé-Hoover thermostat and the Berendsen barostat are used in NpT ensemble for 200 ps and then in NVE for 100 ps to reach the equilibrium. Then 3000 ps raw data are obtained for the calculation of heat current vector. The resultant HCACFs are then directly integrated and the κ_L is set as the average value in the stable regime of the integral.

3.2.4 Analytic models for TE properties

The TE properties are obtained using the Onsager TE coupling and the Boltzmann transport equation (BTE) with relaxation time approximation (RTA). [3, 23, 89, 152, 156, 162, 206]. Detail derivations and descriptions about all electronic TE properties are presented in Section 2.5.1. Here $\Delta E_{e,g,\alpha}$ is the bandgap energy at α point. The carrier mobility depends on $\tau_e(E_e)$ and effective mass $m_{i,e,\alpha}$ which are also temperature dependent. The $\tau_e(E_e)$ is phonon dominated (three mechanisms). The EAIMD calculated $m_{i,e,\alpha}(T)$ for all bands are used in Eqs. (2.17) and (2.18). Including the lattice thermal conductivity from ECMD, then ZT is obtained from Eq. (1.1).

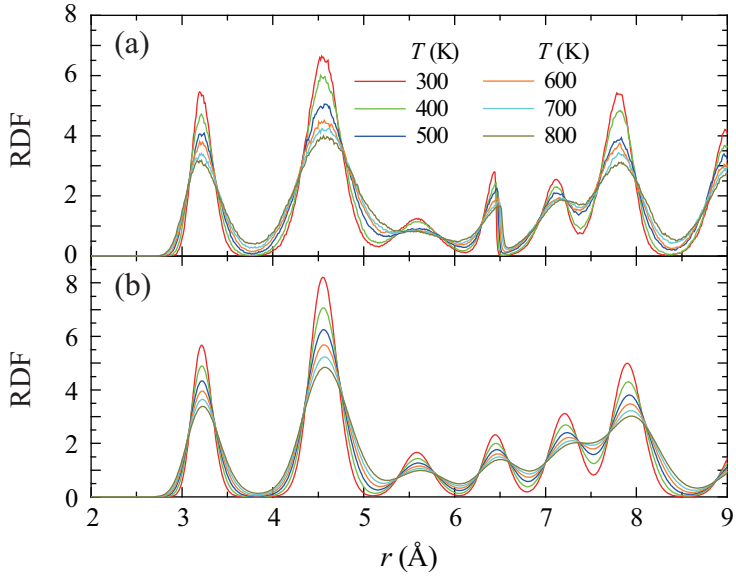

Figure 3.3: Calculated radial distribution functions of PbTe supercell obtained from (a) EAIMD, and (b) ECMD.

3.3 Results and Discussion

3.3.1 Lattice dynamics of thermal-disordered structures

Using EAIMD and ECMD simulations, we verified the abnormal anharmonic lattice dynamics of PbTe over the temperature range. The lattice coordinates of each atom for each time step is collected, and the results are averaged to obtain overall radial distribution function (RDF), as shown in Fig. 3.3. Our simulations successfully reproduce all related lattice dynamics results [31, 223], peak broadening with rising temperature and non-Gaussian asymmetry.

Figure 3.3 shows the RMS atomic off-centering (compared to 0 K) of the ions as a function of temperature. Under the Debye harmonic approximation for isotropic

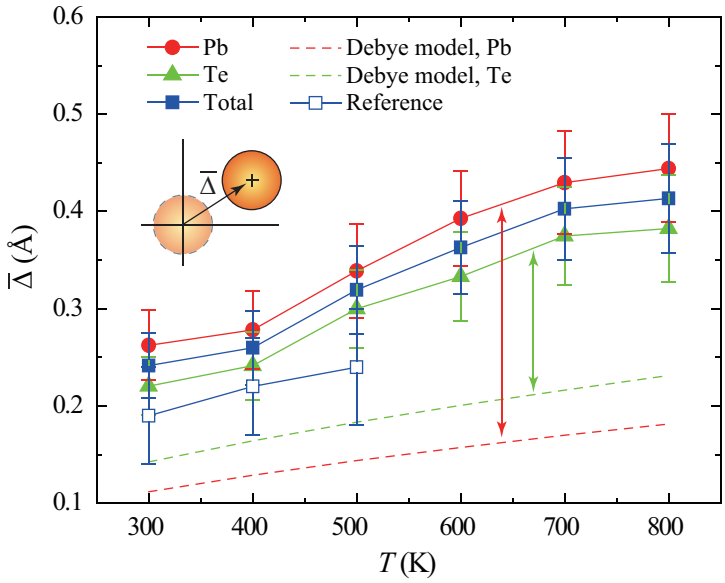

Figure 3.4: Variation of the RMS atomic local off-centering in PbTe, as a function of temperature. The Debye harmonic model prediction and reference results [31] is also shown, with markers for differences with EAIMD results. The inset image marks this RMS displacement.

lattice, the RMS displacement $\overline{\Delta}$ is [105]

$$\overline{\Delta} \equiv \langle[(\boldsymbol{d}_j - \boldsymbol{d}_\circ)\cdot \boldsymbol{s}_j]^2\rangle^{1/2} = \{\frac{3\hbar}{m\omega_{\mathrm{D}}}[\frac{1}{4} + (\frac{T}{T_{\mathrm{D}}})^2 \int_0^{T_{\mathrm{D}}/T} \frac{x\mathrm{d}x}{e^x - 1}]\}^{1/2}, \tag{3.3}$$

where $\boldsymbol{d}_j$ and $\boldsymbol{d}_\circ$ are the displacement vectors of the atom j and the central atom, $\boldsymbol{s}_j$ is the equilibrium position unit vector of the atom j, T_{D} is the Debye temperature, and ω_{D} is the Debye frequency ($= k_{\mathrm{B}}T_{\mathrm{D}}/\hbar$). The Debye model is more realistic model than the Einstein model, all atoms vibrate as harmonic oscillator with one frequency. The Debye model also assumes the atoms vibrate as harmonic oscillators, but now with a distribution of frequencies which is proportional to ω^2 and extends to the Debye frequency ω_{D}. So, we can compare the difference between the Debye model and our EAIMD predictions in terms of the anharmonicity. The results for this relation

are also shown in Fig. 3.4 and the contrast (shown with vertical arrows) demonstrates the anharmonic effect predicted by EAIMD. Among the symmetry-equivalent displaced sites, the amplitude of the Pb displacement is larger than that of Te atoms. This result is highly consistent with the Debye-Waller factor calculation [108], i.e., abnormal bandgap energy increase with temperature. In addition to that, two well-known physical properties related to solid anharmonicity, the Grüneisen parameter and thermal expansion coefficient, are also listed in Table 3.2. The calculated results are in good agreement with the reported values in the literatures [60, 208] and show the extent of anharmonicity. The vibration-mode frequencies of Pb and Te are noticeably different, i.e., the Te ions constitute the optical frequency peak ($f_{\circ,\mathrm{Te}} \sim 2.3$ THz), while the Pb ions dominate in the acoustic regime ($f_{\circ,\mathrm{Pb}} \sim 1.5$ THz). These features cannot be explained with the harmonic or quasi-harmonic models for the lattice dynamics.

3.3.2 Temperature-dependent electronic structures

From the orbital model perspective, the thermal disorder causes local orbital overlapping. Figures 3.5(a) to (d) show the equilibrium atomic positions at 0, 300, 700, and 1100 K along with their charge density distribution. In the presence of thermal disorder, the orbital overlaps increase significantly with temperature. At high temperature, local charge densities are distorted and the valence band distributions are altered.

Also, the distorted D_e (total and partial) plots are shown in Fig. 3.6. At high

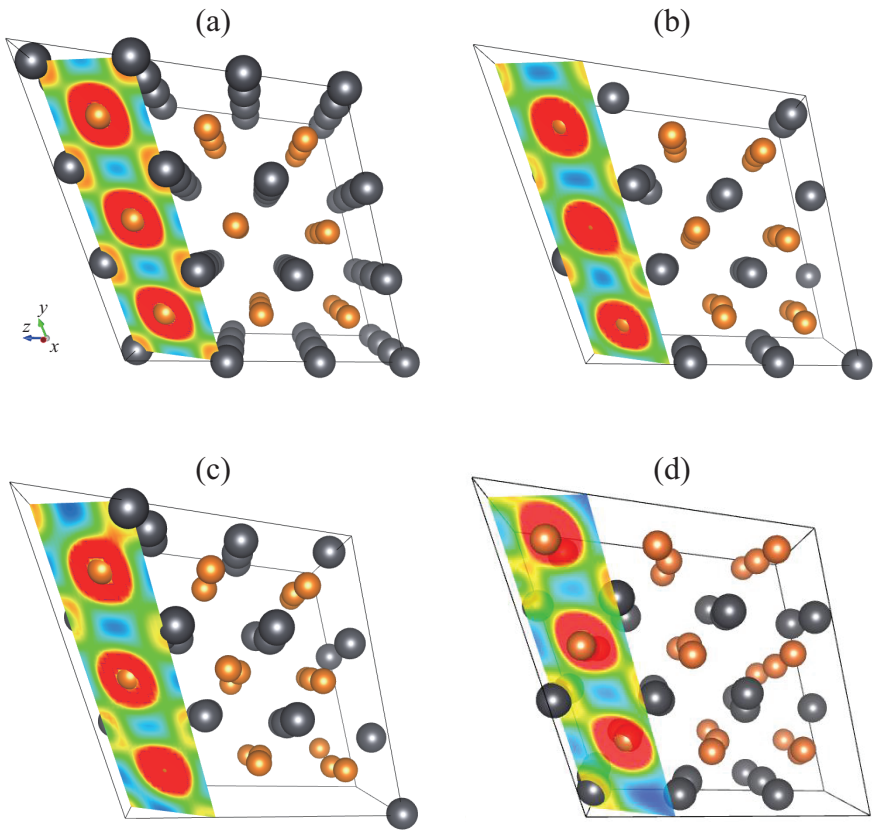

Figure 3.5: The charge densities and atomic positions of PbTe, for (a) $T = 0$, (b) 300, (c) 700, and (d) 1100 K. A slice (101) illustrates the electron-density distribution (a distance from origin of 16.8 Å). The charge density contours are for 0 (blue) to 0.289 (red) $e\text{Å}^{-3}$.

temperatures the vibration amplitudes are substantial and modify the screening properties of the electron density [49]. The D_e for the structures at 300 and 700 K are compared with the frozen structure in Fig. 3.6(a). The static $D_e(T = 0$ K) is not populated at the top of the valence bands, indicating the light hole at L-point, a non-parabolic Kane distribution at the valence edge. The onset of appearance of much larger hole effective mass starting at $\sim$ -0.2 eV below the edge, is manifestation of a resonance near -0.25 eV. It results from the heavy hole in the Σ-direction [182]. At 0 K, this strongly increases $D_e(T)$ below -0.2 eV and is the reason for the unusual doping and temperature dependence of the TE power factor [182]. Compared to $D_e(T$

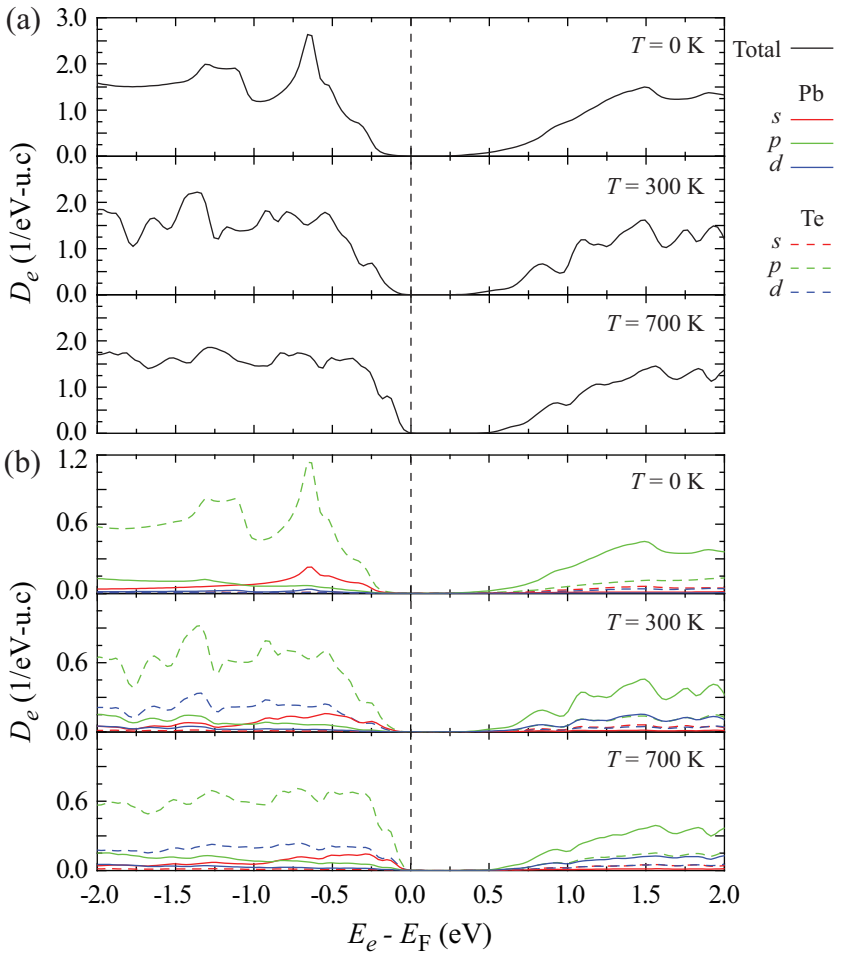

Figure 3.6: (a) Electronic density-of-states for PbTe using static DFT (0 K) and EAIMD calculations (300 and 700 K). (b) Projected electronic density-of-states for PbTe, showing the s, p, and d orbital contributions. Frozen (0 K) and thermal-disordered structure at 300 and 700 K are shown.

= 0 K), the thermal disorder of PbTe structure makes for unique modifications in the $D_e(T)$, as shown in Fig. 3.6(a). The EAIMD results for $D_e(T)$ show the band convergence of the heavy and light holes at high temperatures. First, there is a transition from the non-parabolic (low T) to parabolic (high T) $D_e(T)$ in a principal valence band. Second, comparing 0 and 700 K, the sharp $D_e(T)$ peak (near -0.2 eV, 0 K) splits into two peaks (near -0.12 and -0.4 eV, 700 K). These are highly related with the band convergence at high temperatures. The projected D_e plots [Fig. 3.6(b)] for $T = 0$, 300, and 700 K indicate the orbital contributions to valence band change with temperature. Also they demonstrate that the local orbital overlaps and the valence band distortion become significant with increased temperature. For $T = 0$ K, the Te $5p$ orbital dominate contribution to the first and second valence bands of PbTe. Contributions from Pb ($6s$) and Te ($4d$ and $5p$) to the formation of valence band are found at high temperatures, while contribution from Te $5p$ slightly diminishes. As a result, the thermal disorder and the corresponding increase in the local orbital overlaps (i.e., contribution from Pb $6s$, Te $4d$, and Te $5p$ orbitals at $T = 700$ K) alter the distribution of the valence bands of PbTe at high temperatures.

Thermal-disorder bond anharmonicity leads to the phonon-phonon Umklapp and normal scatterings and reduction of phonon conductivity at high temperatures [48, 49, 140]. In such rocksalt group IV-VI semiconductors, the outer s electrons and part of the p electrons are non-bonding and are expected to form a shell of relatively large radius [140]. This is the well-known reason for the high anharmonicity of the bonds in these materials and the ultimate cause of their low lattice thermal conductivity [48, 49, 140]. Further results on thermal-disorder lattice thermal conductivity (using

Table 3.3: The calculated longitudinal and transverse components of the effective electron (or hole) masses (divided by m_e) at the L- and Σ-points, as a function of temperature.

T (K)	Longitudinal			Transverse		
	$\lvert m_{e,e,\mathrm{L},l}\rvert$	$\lvert m_{h,e,\mathrm{L},l}\rvert$	$\lvert m_{h,e,\Sigma,l}\rvert$	$\lvert m_{e,e,\mathrm{L},t}\rvert$	$\lvert m_{h,e,\mathrm{L},t}\rvert$	$\lvert m_{h,e,\Sigma,t}\rvert$
300	0.141	0.167	1.66	0.0438	0.0563	0.243
400	0.102	0.161	1.75	0.0459	0.0704	0.168
500	0.208	0.134	2.50	0.0420	0.0592	0.198
600	0.204	0.186	2.12	0.0521	0.0876	0.162
700	0.196	0.231	1.25	0.0495	0.113	0.198
800	0.185	0.441	0.96	0.0651	0.122	0.219

ECMD) will be given in later paragraphs.

The calculation of the band structures (Fig. 3.7) and bandgap energies (Fig. 3.8) as a function of temperature are important in explaining the band convergence. The calculated band structures of PbTe supercell provide a clear evidence for band convergence at high temperature (above 450 K), the secondary valence band in the Σ-direction is overcome by the first valence band of L-point and PbTe becomes an indirect bandgap. From the band structures and the electronic density-of-states, we have also verified the bandgap energy changes with temperature (Fig. 3.8). The temperature dependence of the bandgap energy $\Delta E_{e,g}$ for PbTe is modeled [3] as $\Delta E_{e,g}$ $= 0.19 + (0.42\times10^{-3})T$ for $T \leq 400$ K and $\Delta E_{e,g} = 0.358$ eV for $T > 400$ K, in good agreement with experimental results [196]. Noting that the general underestimation of the bandgap energy in DFT calculation, the calculated results have a similar behavior as the experiment.

Such thermal disorder electronic band alterations are quantified by temperature-dependent $m_{i,e,\alpha}(T)$. Some previous analyses treated this as constant value $m^{\circ}_{i,e,\alpha}$, or semi-temperature dependent $m_{i,e,\alpha}(T) = m_{i,e,\alpha}(0)[\Delta E_{e,g,\alpha}(T)/\Delta E_{e,g,\alpha}(0)]$ [87, 89, 92,

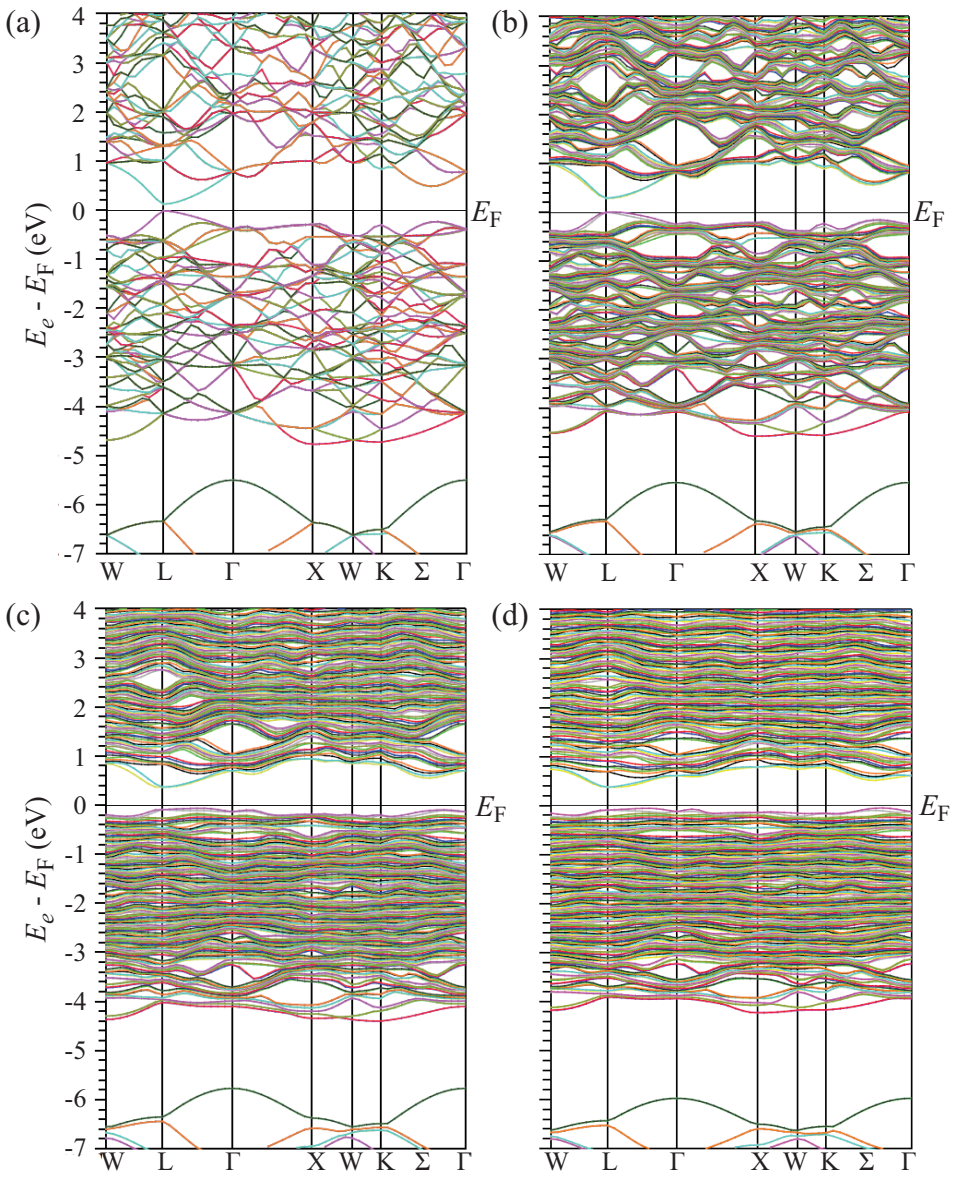

Figure 3.7: Calculated band structures of PbTe supercell (3×3×3 primitive cells) at (a) $T = 0$, (b) 300, (c) 700, and (d) 1100 K.

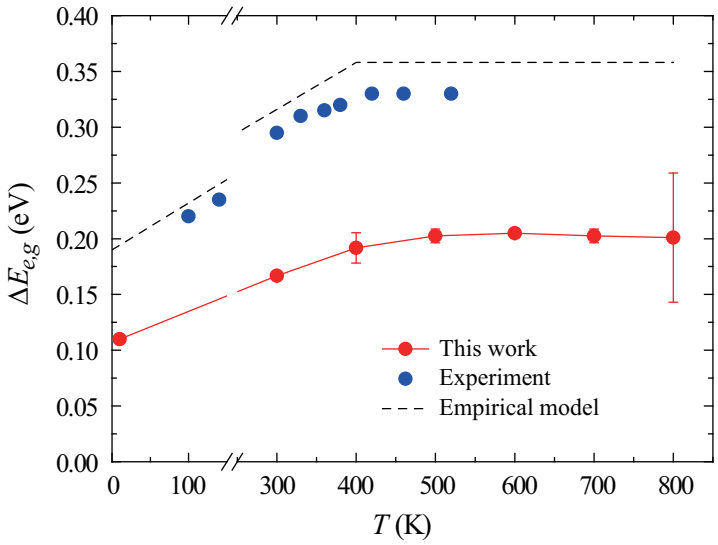

Figure 3.8: Variations of PbTe bandgap energy as a function of temperature. The experimental results [196] and the proposed empirical model results [3] are also shown.

145, 153, 206]. Using the DFT band structure of the thermal-disordered PbTe, we calculate the effective masses for each band in at Brillouin zone points and direction (fitted to parabolic model) as a function of temperature. The band effective mass $(m_{i,e,\alpha})_b$ is $1/(m_{i,e,\alpha})_b = (1/\hbar^2)[\partial^2 E_e(\boldsymbol{k})/\partial \boldsymbol{k}^2]_\alpha$ ($i = h$ or e and α is location in Brillouin zone) [105, 153]. This can be written in the tensor form as

$$M_{ij}^{-1} = \frac{1}{\hbar^2}\frac{\partial^2 E_e(\boldsymbol{k})}{\partial \boldsymbol{k}_i \partial \boldsymbol{k}_j} \text{ and } m_{e,e} = [\det|M_{ij}|]^{1/3}. \tag{3.4}$$

With the assumed parabolic E_e-k relationship at band extrema, the parabolic E_e can be generalized to

$$E_e = E_{e,\circ} + A_x(k_x - k_{\circ,x})^2 + A_y(k_y - k_{\circ,y})^2 + A_z(k_z - k_{\circ,z})^2, \tag{3.5}$$

where coefficient A_i is constant and $(k_{\circ,x},\ k_{\circ,y},\ k_{\circ,z})$ is the coordinate of band min-

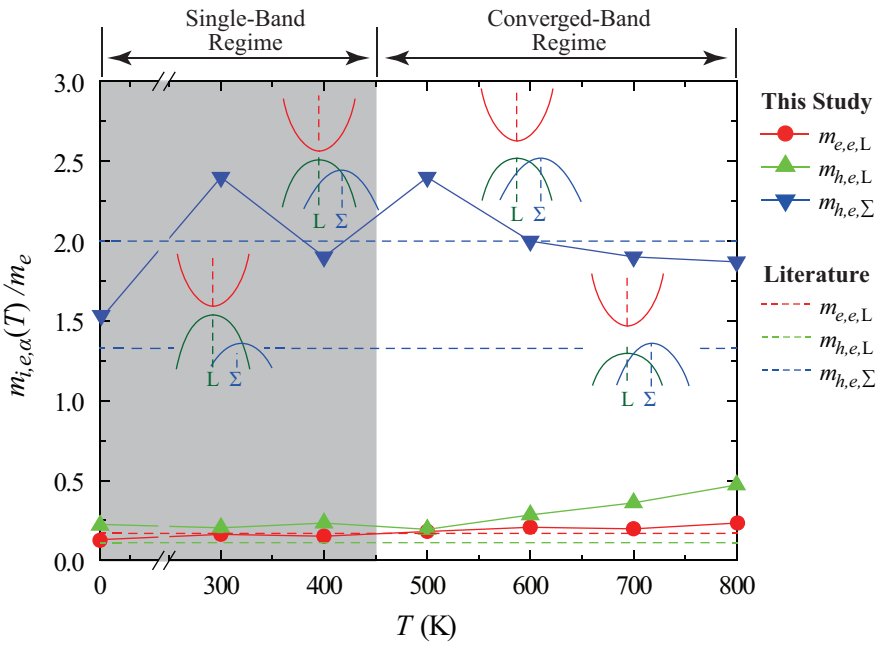

Figure 3.9: Temperature dependent the density-of-states effective masses $m_{i,e,\alpha}(T)$ obtained from DFT-EAIMD. Two regimes, single- and converged-band, are also defined. The band-alignment evolution with temperature, is also illustrated. m_e is electron mass. Literature results [8, 162] are also shown in dashed lines

ima/maxima. Assuming isotropic dispersion at specific point, the effective mass tensor has equal diagonal tensor elements $m_{e,e,xx} = m_{e,e,yy} = m_{e,e,zz}$ (off-diagonal elements are zero $m^{-1}_{e,e,ij} = 2A_i\delta_{ij}$) and all A_i's are equal. Thus the effective mass tensor reduces to $m_{e,e} = 1/2A_i$. In order to maintain such scalar calculation, each components, longitudinal and transverse, of effective mass is calculated independently. The electron/hole pockets of PbTe can be characterized by a longitudinal mass ($m_{i,e,l}$) along the corresponding direction and two transverse masses ($m_{i,e,t}$) in the plane perpendicular to the longitudinal direction (with above parabolic-isotropic assumption). The value for each direction is quite different (i.e., longitudinal components are always larger than transverse) and this holds for the temperature range. This is in good agreement with a well-known feature of PbTe. The calculated effective mass

components are shown in Table 3.3. The density-of-states effective mass $m_{i,e,\alpha} = N_{i,\alpha}^{2/3}(m_{i,e,\alpha})_b = N_{i,\alpha}^{2/3}(m_{i,e,\alpha,l}m_{i,e,\alpha,t}^2)_b^{1/3}$, where $N_{i,\alpha}$ is orbital degeneracy of each valley ($N_{e,\mathrm{L}} = N_{h,\mathrm{L}} = 4$ and $N_{h,\Sigma} = 12$ [87, 145, 153]). The results for the electron and hole $m_{i,e,\alpha}$, as a function of temperature, are shown in Fig. 3.9. Note that the electron/hole effective mass at $T = 0$ K and band locations L- and Σ-points are $m_{e,e,\mathrm{L}} = 0.130m_e$, $m_{h,e,\mathrm{L}} = 0.225m_e$, and $m_{h,e,\Sigma} = 1.51m_e$. These are very close to those reported in [8]. Below 450 K, labeled as the "single-band regime", the L-point dominates and it is a light hole band. For $450 < T < 800$ K, labeled as the "converged-band regime", the heavy hole of Σ-point band become curved (be lighter) and matches with the light hole L-point band. Simultaneously, the promotion of the holes from the light to heavy valence bands increases $m_{h,e,\Sigma}$ in the converged regime. Thus the two bands converge and play a central role as the combined first valence band (light and heavy hole). So, the resultant effective mass increases and peaks around 500 K. These clearly show the band convergence effect in $450 < T < 800$ K.

3.3.3 TE transport properties with thermal-disordered structures

As described in the methods (Section 3.2), the transport calculations are done using the Boltzmann transport equations with energy-dependent relaxation time $\tau_e(E_e)$.

Although $\tau_e(E_e)$ can be determined from the wave function and the perturbation potential obtained from the first-principle calculations, this is very challenging. Here

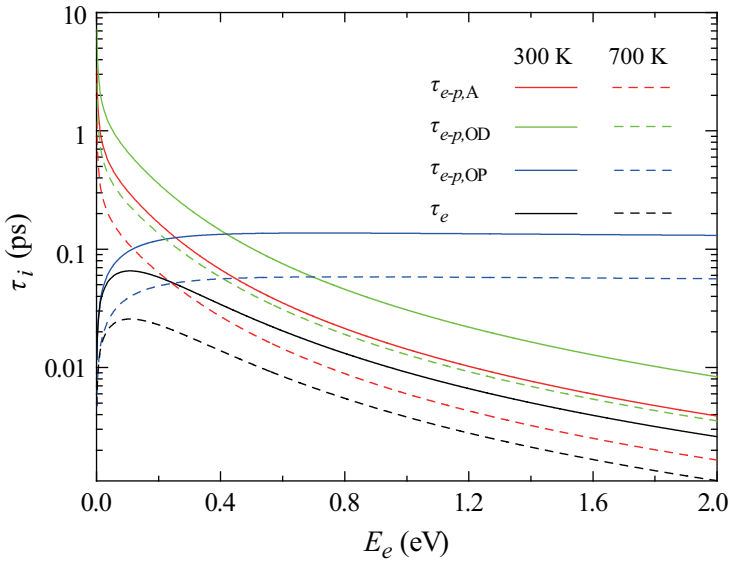

Figure 3.10: Calculated energy-dependent electron-phonon relaxation times, for 300 and 700 K. The subscripts A, OD, and OP refer to acoustic, optical with deformation potential couplings, and optical with polar coupling.

instead we use the relaxation time models [23, 89, 140, 156, 206, 216] with three dominant electron scattering mechanisms [156, 216], namely, i) acoustic (A), ii) optical with deformation potential couplings (OD), and iii) optical phonons with polar coupling (OP). The total $\tau_e(E_e)$, using the Matthiessen rule, is

$$\frac{1}{\tau_e(E_e)} = \sum_{i=1-3} \frac{1}{\tau_{e-p,i}(E_e)}, i = \mathrm{A, OD, or\ OP}. \tag{3.6}$$

The models and their parameters are given in [23, 89, 140, 156, 206, 216]. Figure 3.10 shows the calculated energy-dependent relaxation times as a function of electron energy, for $T = 300$ and 700 K. At low E_e (practical doping), the electron-optical phonons scattering with polar coupling is dominant.

The calculated transport properties are illustrated in Figs. 3.11(a) to (c), namely α_{S}, σ_e, and $\kappa = \kappa_e + \kappa_L$ (κ_e is calculated with `BoltzTraP`), as a function of tem-

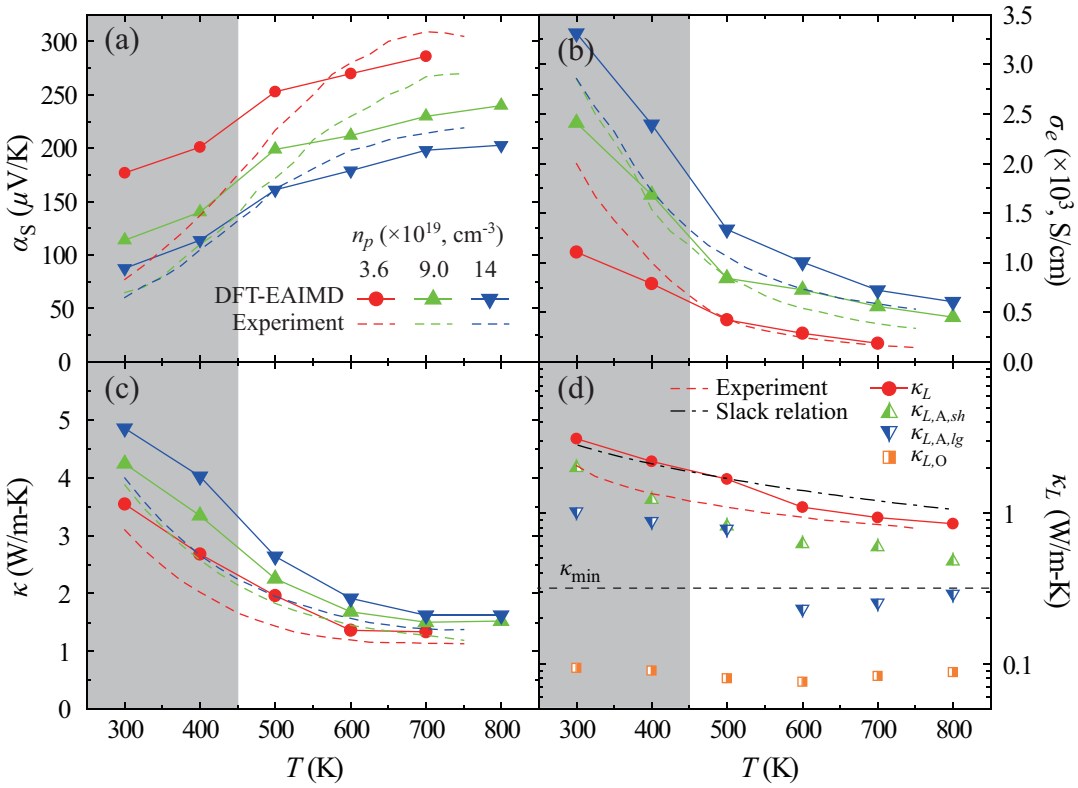

Figure 3.11: Predicted TE properties of PbTe, and comparison with experiments [152]. (a) Temperature dependence of the Seebeck coefficient, (b) electrical conductivity, and (c) total thermal conductivity, for three different carrier concentrations n_p. (d) Temperature variations of lattice thermal conductivity and its short- and long-range acoustic and optical components. Cut-off frequency of 1.5 THz is used [99, 105, 111]. The amorphous-phase minimum lattice thermal conductivity is also shown.

perature, for three different hole concentrations n_p (the Fermi energy). The available experimental results [152] are also shown. The Hall factor $r_{\rm H}$ and the Hall coefficient $R_{\rm H}$, $n_p = r_{\rm H}/e_c R_{\rm H}$, are used in the calculations of n_p [87, 153, 206], i.e.,

$$r_{{\rm H},\alpha} = \frac{\int_0^\infty (-\frac{\partial f_e^\circ}{\partial E_e})\gamma_\alpha(E_e)^{3/2}{\rm d}E_e \int_0^\infty (-\frac{\partial f_e^\circ}{\partial E_e})\tau_e(E_e)^2\gamma_\alpha(E_e)^{3/2}[\frac{{\rm d}\gamma_\alpha(E_e)}{{\rm d}E_e}]^{-2}{\rm d}E_e}{\{\int_0^\infty (-\frac{\partial f_e^\circ}{\partial E_e})\tau_e(E_e)\gamma_\alpha(E_e)^{3/2}[\frac{{\rm d}\gamma_\alpha(E_e)}{{\rm d}E_e}]^{-1}{\rm d}E_e\}^2}. \qquad (3.7)$$

The trends in the temperature dependence of the TE properties are highly correlated with the thermal-disorder behavior of PbTe. The Seebeck coefficient reaches a plateau

after 500 K because the parabolic Σ-band is dominant above this temperature. For more complete calculation, the Seebeck coefficient can be expressed as the sum of $\alpha_{\mathrm{S,presence}}$ and $\alpha_{\mathrm{S,transport}}$ [64]. Here $\alpha_{\mathrm{S,presence}}$ is the sum of contributions to the carrier-induced entropy change, i.e., $\alpha_{\mathrm{S,presence}} = \alpha_{\mathrm{S,mix}} + \alpha_{\mathrm{S,spin}} + \alpha_{\mathrm{S,vibration}}$, where the right hand side terms are change of the entropy-of-mixing, spin entropy, and vibrational entropy upon adding a charge carrier, respectively. The other contribution $\alpha_{\mathrm{S,transport}}$ is equal to the net energy transferred in moving a carrier divided by $q_e T$, where q_e is the carrier charge. In this study, we approximate that $\alpha_{\mathrm{S,mix}}$ is the dominant and the only contribution, since $\alpha_{\mathrm{S,spin}}$, $\alpha_{\mathrm{S,vibration}}$, and $\alpha_{\mathrm{S,transport}}$ are estimated to be negligible. These are justified due to (i) not including the magnetic properties, (ii) negligible vibrational contribution, and (iii) no significant change in the mechanism of charge transport over entire temperature range (300 to 800 K). The reduction in the electrical conductivity and the decrease in the total thermal conductivity also result from the thermal disorder and the effective mass changes. The heavy- and light-hole band convergence has a dominant role in the charge transport. As the band effective mass increases, the electronic contribution to the thermal conductivity is reduced [158]. The D_e slope and its peaks near the band edge often dictate the overall performance, and semiconductors with heavy electron masses and multiple valleys have high ZT potential. For all predicted properties, there are good agreement with experiments [152].

The lattice thermal conductivity κ_L is determined using the ECMD results and the Green-Kubo HCACF decay [99, 105, 111]. Figure 3.11(d) shows the predicted κ_L as a function of temperature, and demonstrates the suppression of the lattice thermal

conductivity in the thermal-disordered structures (> 500 K). The ECMD results are: κ_L(300 K) = 3.1 and κ_L(700 K) = 0.9 W/m-K. The results show that κ_L decreases noticeably with increased temperature. The minimum conductivity $\kappa_{\min}$ [33, 34] for the amorphous phase is also shown, and gives $\kappa_{\min} \approx 0.32$ W/m-K (for $T > 2T_{\rm D}$, where $T_{\rm D,PbTe} = 130$ K [140, 152]) using the PbTe properties [208]. Figure 3.11(d) includes the results reported in [152] using the total thermal conductivity and the Wiedemann-Franz law. The results of the Slack relation [98, 105, 185] for the lattice thermal conductivity of crystal at high temperatures ($T > 0.1T_{\rm D}$) are also shown in Fig. 3.11(d), using the properties listed in Table 3.2. Prior to the onset of significant thermal disorder ($T < 500$ K), the ECMD results are in good agreement with the Slack relation (T^{-1} dependence). For $T > 500$ K, the thermal-disorder scattering becomes significant the lattice thermal conductivity becomes independent of temperature. This shows that the κ_L in thermal-disordered PbTe structure has two phonon transport regimes, pseudo-symmetry (single-band) and pseudo-amorphous (converged-band). The thermal-disordered structures represent a pseudo-amorphous phase which has high temperature anharmonic vibrations. In Fig. 3.11(d), we also decompose $\kappa_L(T)$ of PbTe into three components, namely, the acoustic short-range, acoustic long-range, and optical [99, 105, 111], i.e.,

$$\kappa_L = \frac{1}{k_{\rm B} V T^2} \left(A_{{\rm A},sh}\tau_{{\rm A},sh} + A_{{\rm A},lg}\tau_{{\rm A},lg} + \sum_i \frac{B_{{\rm O},i}\tau_{{\rm O},i}}{1+\tau_{{\rm O},i}^2} \right) = \kappa_{L,{\rm A},sh} + \kappa_{L,{\rm A},lg} + \kappa_{L,{\rm O}}, \quad (3.8)$$

where the τ_i is time constant, A_i and B_i are constants, and the subscripts sh, lg, A, and O refer to short-range, long-range, acoustic, and optical. From Fig. 3.11(d), the

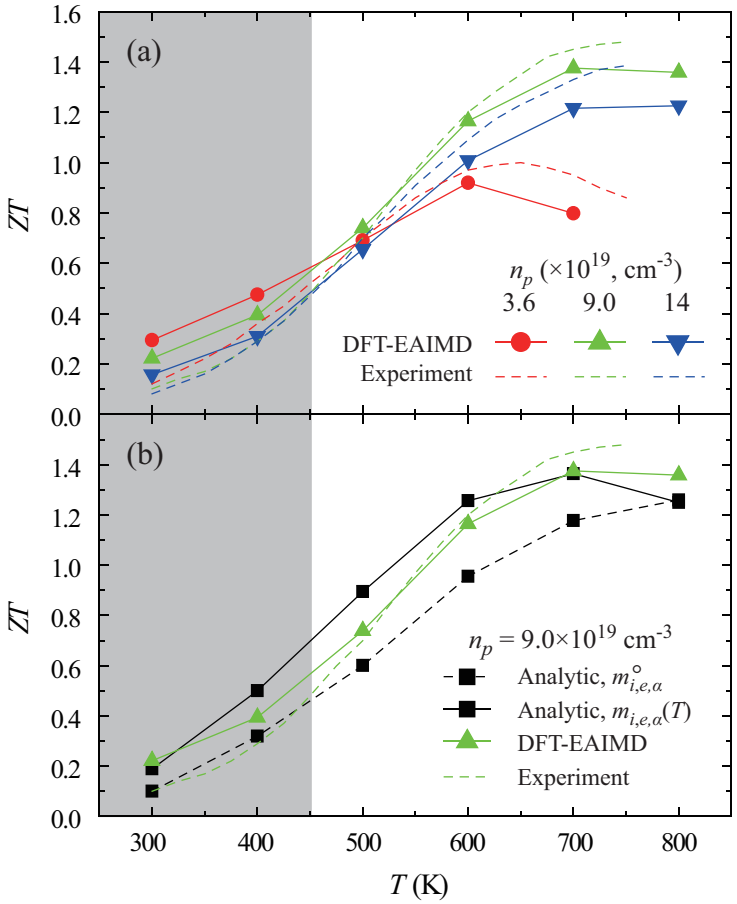

Figure 3.12: (a) Variations of the DFT-EAIMD predicted ZT as a function of temperature for the p-type PbTe, at three different carrier concentrations n_p. The corresponding experimental results [152] are also shown. (b) Variation of $ZT(T)$ obtained from the analytic model using constant $m^{\circ}_{i,e}$ and temperature-dependent $m_{i,e}(T)$, for the 9.0×10^{19} cm^{-3}.

short- and long-range acoustic phonon contributions are dominant and most affected by the thermal disorder. The long-range acoustic contribution is almost saturated to the amorphous κ_L limit, but short-range is still changing up to 800 K. Note that κ_L decreases most noticeably in the converged-band regime.

Combining all four TE properties from DFT and ECMD/Green-Kubo calculations, the predicted ZT of p-doped PbTe as a function of temperature, is shown in Fig. 3.12(a), along with the experimental results [152]. The results are for three dif-

ferent carrier concentrations n_p, including peak performance at $n_p = 9.0{\times}10^{19}$ cm^{-3}. The results for thermal-disordered structures are in good agreement with the experiments [152]. In order to confirm the thermal-disorder effective mass calculations, the results of two analytical models [constant $m^{\circ}_{i,e,\alpha}$ and temperature-dependent $m_{i,e,\alpha}(T)$] are shown in Fig. 3.12(b). With the temperature-dependent effective mass (Fig. 3.9), the analytical model prediction matches the DFT and the experimental results. In contrast, the constant effective mass [$m^{\circ}_{e,e,\mathrm{L}} = m^{\circ}_{h,e,\mathrm{L}} = 0.13$, $m^{\circ}_{h,e,\Sigma} = 1.3$] results [8], i.e., neglecting the band convergence ($450 < T < 800$ K) and divergence ($T <$ 450 K and $T > 800$ K), underestimate ZT over the entire temperature range. The thermal-disorder model and its effective mass of the altered band structures reveal the high-ZT PbTe behavior.

Due to the computation resource and time limitations, the time and length domains of EAIMD simulations are limited. So, we have used the number of atoms in the periodic cell to simulate the extended system effects. In order to reliably predict the thermal-disordered structure and its electronic structures, by minimizing the statistical uncertainties, we use i) long enough simulation time to find well-converged structures, and ii) large number of atom in a simulation cell to minimize the drawbacks of the periodic boundary condition. These highly correlate with transport properties such as the phonon/electron lifetime and mean free path. Because of these limitations on the EAIMD simulaitions, we pursued quantitative verifications such as the ones on the selection of representative snapshots, before entering the transport property calculations.

3.4 Summary

In summary, we investigate the abnormal band convergence and TE properties of PbTe using *ab-initio* thermal-disordered structures, i.e., at high temperatures the atoms do not occupy the ideal lattice positions, thus affecting the charge and phonon transports. Thermal disorder modifies the charge effective mass and suppresses the phonon short- and long-range acoustic contributions, resulting in high ZT for the converged-band, pseudo-amorphous structure (acoustic phonon suppression). Understanding of the thermal disorder provides an insight into design of improved TE chalcogenides.

Chapter 4

Order-Disorder Transition of Filled Skutterudites

4.1 Introduction

High-performance TE materials including skutterudites [135, 147, 170, 201, 202], metal silicides [69], complex chalcogenide compounds [97], clathrates [43, 163], half-Heusler alloys [112], and oxide materials [197] are sought for efficient power generation. Skutterudites are particularly promising due to their robust mechanical properties [171] and allow for single or multiple filling with rare-earth and alkaline-earth metals that reduce the lattice thermal conductivity κ_L [135, 139, 146, 147, 170, 201].

Binary skutterudites are compounds with the general formula MX_3 (M = Co, Rh, Ir and X = P, As, Sb) having a crystal structure with a BCC lattice and belonging to the space group $Im3$. The structure consists of a periodic array of trigonally distorted and tilted MX_6 octahedrons. The metal M at the center is octahedrally coordinated

by the pnicogen X [169]. The tilt of the MX_6 octahedrons gives rise to empty spaces (icosahedral voids) that form a body-centered sublattice. As first shown in [102], the voids are large enough and can be filled by foreign species entering as cations, however, the filler solubility limit is less than a full filling of all available voids [178, 201].

Binary skutterudites possess very high charge carrier mobilities and the interest in these compounds as novel TE materials for power generation followed a suggestion [186] and observation [139] that their κ_L can be dramatically reduced upon filling the structural voids. Recent research has resulted in the TE figure-of-merit (ZT), Eq. 1.1, of n-type skutterudites approaching the value of 1.5 at 800 K [121]. While the presence of the filler species in the skutterudite matrix seems to be essential for achieving low κ_L and hence high ZT, whether the filler acts as a rattling local vibration mode [135, 147, 170, 201] or plays some other important role [43, 100, 115, 210] remains controversial. So far the only insight into the role of ordered phases on the κ_L of partially-filled skutterudites has been the observation in [147] that the random distribution of filler ions scatter phonons more effectively than when most voids are filled.

In this chapter, we address the issue of ordering of the filler species, a topic that has not yet been explored and that has a great influence on scattering of heat-conducting phonons. To this end we examine $Ba_xCo_4Sb_{12}$, a skutterudite with a large filling fraction limit for Ba, using theoretical and computational treatments.

4.2 Calculation Methods

4.2.1 Cluster expansions

We explored the ground-state configurations among all possible ways of arranging Ba atoms on sites of the fillers in $CoSb_3$ using DFT calculations, guided by the CE method. To fit the ECI of the CE, we calculated the total energy of 28 Ba-vacancy configurations over the void sites (BCC sublattice) of $CoSb_3$ using DFT. The DFT calculations were performed using the `VASP` code [116] within the PBE parameterization of the GGA for exchange and correlation [154] and using the PAW method [26, 117]. Details are given in Section 2.2. In the total energy calculations all atomic positions as well as the unit cell dimensions were fully relaxed. The ECI were fit to reproduce the formation energies (ΔE_f) of $Ba_xCo_4Sb_{12}$, defined as

$$\Delta E_{f,i} = E^x_{\circ,i} - [(1-x)E^{\mathrm{V}}_{\circ,i} + xE^{\mathrm{Ba}}_{\circ,i}], \tag{4.1}$$

where $E^x_{\circ,i}$ is the total energy of the crystal with Ba atoms (concentration x), $E^{\mathrm{V}}_{\circ,i}$ is the total energy of the crystal without any Ba (i.e., $CoSb_3$), and $E^{\mathrm{Ba}}_{\circ,i}$ is the total energy of the crystal when all Ba sites are filled (i.e., $BaCo_4Sb_{12}$). Figure 4.1 shows the DFT formation energies ΔE_f as well as those predicted by the CE. The CE was also used to predict energies of other Ba-vacancy configurations not considered with DFT. The ground-state structures are those that lie on the convex hull. These are stable ordered phases that should be stable at low temperature. The weighted CV score, an estimate of the predictive error of the CE, which is considered reasonably

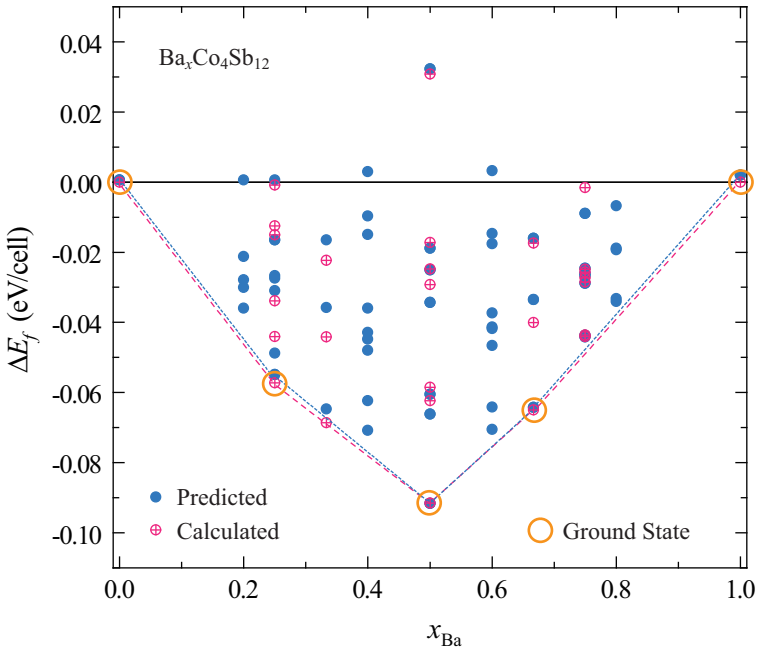

Figure 4.1: Convex hull of $Ba_xCo_4Sb_{12}$ compounds computed through the formalism of CE. Formation energies predicted from the CE and calculated from DFT as a function of Ba composition. The large orange circles indicate ground-state atomic structures and are confirmed by the DFT calculations.

small. The optimized CE includes 10 ECI and has a cross validation score of 6 meV/site and an RMS error of 4 meV/site.

4.2.2 Molecular dynamics simulations

In order to obtain the empirical MD potentials of compounds in the intermediate concentration, we used the combinative rules (CRs) with the empty $CoSb_3$ and fully-filled $BaCo_4Sb_{12}$ potentials from [100]. The Morse potential is useful for covalent bonds and is

$$\varphi(r_{ij}) = \varphi_\circ\{[1 - \exp(-a(r_{ij} - r_\circ))]^2 - 1\}, \tag{4.2}$$

where $\varphi_\circ$ is the depth of the potential energy minimum, a is a parameter related to the depth and width of the potential well, and $r_\circ$ is the equilibrium bond length. For the Morse parameters for A-B compounds (e.g., half-filled, $x = 0.5$), we used the Lorentz-Berthelot mixing rules [68, 129, 161]. The A-B structural parameters ($\varphi_\circ$, a, and $r_\circ$) are assumed to have the form of

$$\varphi_\circ^{\mathrm{AB}} = \frac{\varphi_\circ^{\mathrm{A}} + \varphi_\circ^{\mathrm{B}}}{2}, \tag{4.3}$$

$$r_\circ^{\mathrm{AB}} = (r_\circ^{\mathrm{A}} r_\circ^{\mathrm{B}})^{1/2}, \tag{4.4}$$

$$a^{\mathrm{AB}} = (a^{\mathrm{A}} a^{\mathrm{B}})^{1/2}, \tag{4.5}$$

where A and B are denoted as an empty ($x = 0$) and fully-filled structure ($x = 1$), respectively. In our CRs method, the `GULP` code [72] was used for the prediction of the phonon properties.

We use the Morse and three-cosine potentials, parameterized for two-body (Co-Sb, Co-Co, Sb-Sb, and Ba-Sb) and three-body (Co-Sb-Sb) interactions [100, 129]. Interatomic potentials are simplified fields and the CRs are approximations, therefore these potentials cannot accurately predict for example compound formation energy. As related to κ_L, the structural parameters (Co-Sb first neighbor bond length $r_\circ$), elastic properties (bulk modulus B and elastic constant C_{ij}), average phonon speeds $u_{p,g,\mathrm{A}}$, and specific heat capacity c_v (at 300 K) found from these potentials and from DFT are summarized in Table 4.1.

Using CRs, the ECMD with the Green-Kubo formalism is used for the prediction of lattice thermal conductivity at intermediate Ba composition. It is expressed with

Table 4.1: Comparison of $Ba_{0.25}Co_4Sb_{12}$ properties obtained from CRs and DFT. The available results for $CoSb_3$ are also listed. The $u_{p,g,A}$ is along the Γ-N and Γ-H directions.

	$r_\circ$ (Å)	B (GPa)	C_{11} (GPa)	C_{44} (GPa)	$u_{p,g,A}$ (m/s)	c_v (J/mol-K)
CRs	2.56	78	155	37	3098	22.9
DFT	2.54	82	126	54	2526	23.0
Literature		82[222]	158[222]	57[222]	2934[135]	

HCACF decay equation and heat current vector [99, 105, 111, 133, 134], Eqs. (2.27) and (2.28). Details are given in Section 2.5.2. To minimize computation time and size effects, the ECMD simulations were mostly performed on systems consisting of many conventional unit cells ($\sim$ 3600 atoms). While κ_L results are for a specific direction for each atomic configuration, we verified that the phonon transport in that direction is not noticeably affected by the small dimensions in the other two directions. We also checked that the size effects were minor when using the supercell system consisting of $\sim$ 3600 atoms [100]. The Verlet leapfrog algorithm with the Nosé-Hoover thermostat and the Berendsen barostat were used in NpT ensemble for 200 ps and then in NVE for 100 ps to reach the equilibrium. Then 3000 ps raw data were obtained for the calculation of heat current vector. The resultant HCACFs were then directly integrated and the κ_L was set as the average value in the stable regime of the integral.

According to the results of thermodynamic calculations [Figs. 4.1 and 4.5(a)], we used five different atomic configurations as input structures of ECMD simulations at 300 K: empty ground-state [$x = 0$, Fig. 4.2(a)], solid-solution ($x = 0.03$ and 0.14), γ-phase ground-state [$x = 0.25$, Fig. 4.2(b)], two-phase mixture ($x = 0.33$, 0.38, and

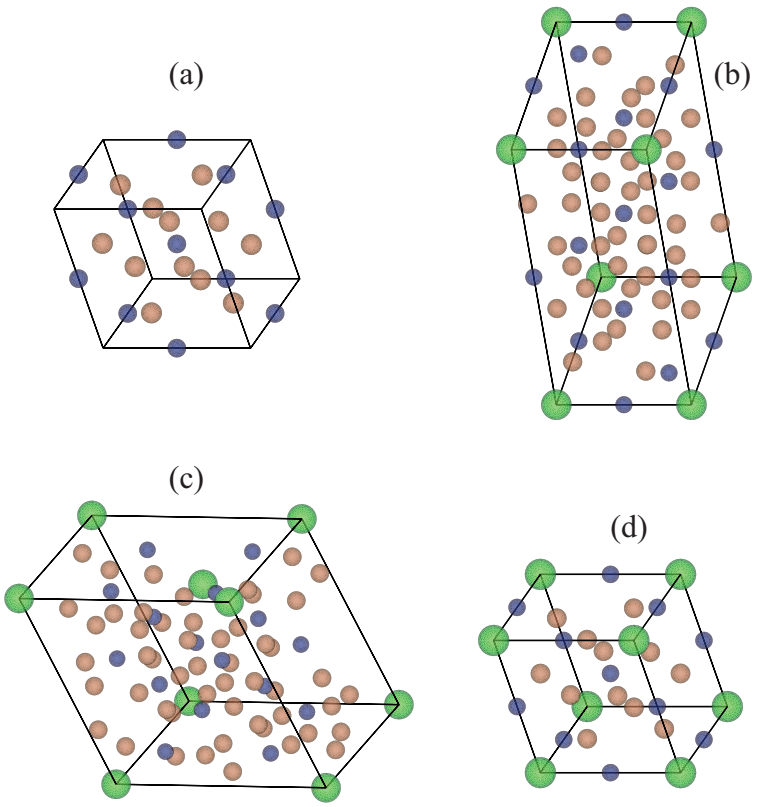

Figure 4.2: Various atomic structures (configurations) of $Ba_xCo_4Sb_{12}$ compounds. For $Ba_xCo_4Sb_{12}$, the green large spheres represent the Ba atoms, the small blue spheres represent the Co atoms, and the small brown spheres represent Sb atoms. (a) Empty ($x = 0$), (b) γ-phase (ground-state of $x = 0.25$), (c) α-phase (ground-state of $x = 0.5$), and (d) fully-filled structure ($x = 1$).

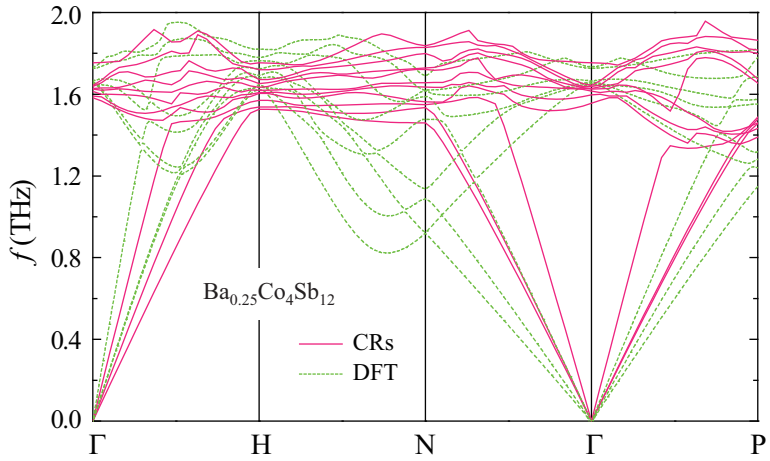

Figure 4.3: Calculated phonon dispersions of the $Ba_{0.25}Co_4Sb_{12}$ compounds using empirical potentials (with the CRs) and DFT. Most optical phonon branches are omitted.

0.44), and α-phase ground-state [$x = 0.5$, Fig. 4.2(c)]. When temperature increased to 800 K, all configurations of different Ba concentrations were obtained from solid-solution structure (MC snapshot). During the ECMD simulation time of 3000 ps, these atomic structures were very stable and confirmed with ECMD movie.

In the two-phase regime ($0.25 < x < 0.5$), the atomic structures used in ECMD calculations, are divided into $CoSb_3$ host and Ba filler atoms. We use two steps to set up the mixture, first we construct a full-atomic configuration 14×2×2 supercells (system volume $\sim$ 86,700 Å^3) of α-phases. And then, we modify the Ba atom' positions to reach a composition (e.g., for $x = 0.38$, mixture is made first half with $x = 0.25$ and then second half with $x = 0.5$), keeping the desired Ba positions of the $x = 0.25$ and $x = 0.5$ in the $CoSb_3$ host structures. Then in the ECMD simulations of these mixture structures we use the empirical potentials from CRs. All ECMD two-phase structures have a single two-phase interface and periodic boundary conditions in all three directions.

4.2.3 Phonon calculations

The DFT method directly calculates the force field using the `VASP` and `PHONON` [151] codes. Details are given in Section 2.3. This *ab-initio* calculation of the HF forces begins by the displacement of the Co, Sb, and Ba atoms along the x, y, and z directions, ± 0.03 Å. For the case of $x = 0.25$ ground-state structures, each displaced configuration generates $2\times3\times65 = 390$ components of the HF forces. The calculated HF forces for quarter-filled structure and used in the `PHONON`.

Figure 4.3 shows the phonon branches for $x = 0.25$ (ground-state, γ-phase) from using CRs and from DFT methods. The three acoustic branches have similar trends (on the average). We compared the acoustic phonon characteristics, predicted using CRs and DFT, and found good agreement in their predicted phonon density of states and its integrated value. Comparison of the total phonon density-of-states $D_p(\omega)$ from two methods is shown in Figs. 4.4(a) to (d). These are the total phonon density-of-states of $x = 0.25$ (ground-state, γ-phase) compounds with respect to frequency. Also, the integrated phonon density-of-states is given in Figs. 4.4(c) and (d). The integrated phonon density-of-states is defined by

$$N(\omega) = \int_0^{\omega} D_p(\omega)\mathrm{d}\omega. \tag{4.6}$$

Even though there are some apparent deviations for the group velocity and the energy along the Γ-N direction, the results show the overall sound speed and specific heat capacity (includes all the modes) would agree well between the two methods calculation.

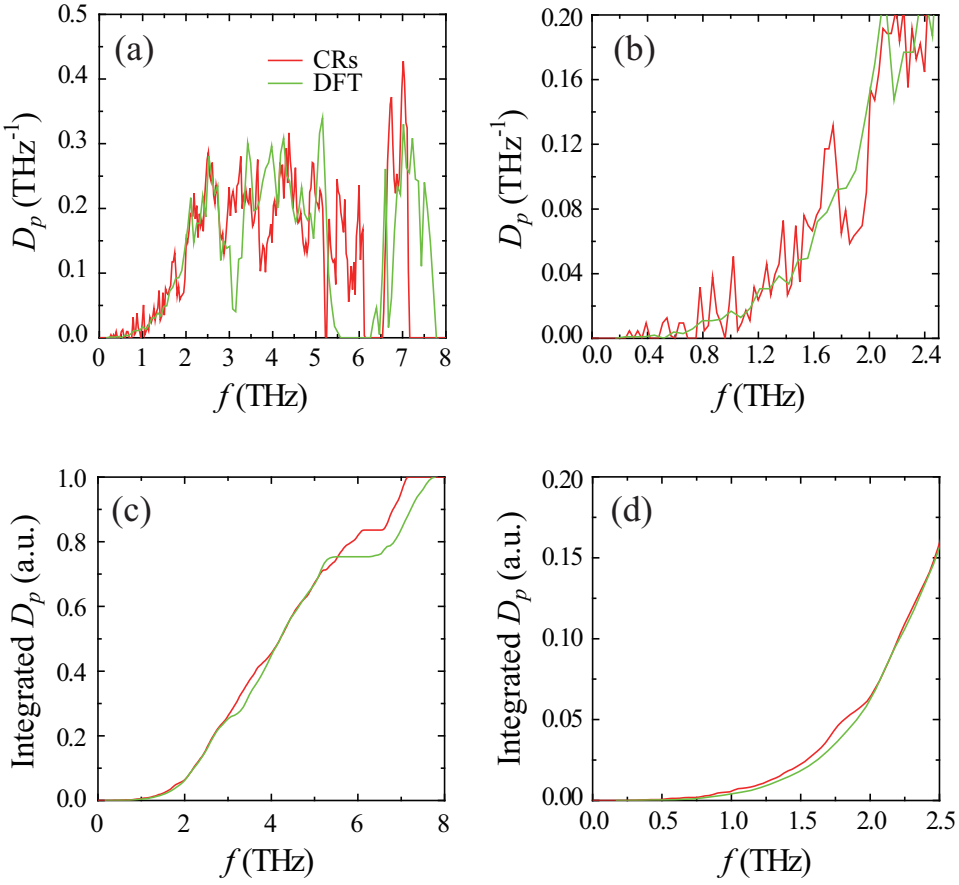

Figure 4.4: Calculated phonon density-of-states (and its integrated value) of the $Ba_{0.25}Co_4Sb_{12}$, as a function of frequency, using CRs and DFT. Here (b) and (d) are magnifications of (a) and (c).

4.2.4 Analytical lattice thermal conductivity

The Cahill-Pohl thermal conductivity [33, 34] assumes all phonons have a mean free path equal to one-half of their wavelength and is assumed to give the thermal conductivity of the amorphous phase. So, it is designated as the minimum thermal conductivity $\kappa_{\min}$ of solid-state materials. The thermal conductivity in this model is given by

$$\kappa_{\min} = (\frac{\pi}{6})^{1/3} k_{\mathrm{B}} n^{2/3} \sum_{i=1}^{3} u_{p,g,i} (\frac{T}{T_{\mathrm{D},i}})^2 \int_0^{T_{\mathrm{D},i}/T} \frac{x^3 e^x}{(e^x - 1)^2} \mathrm{d}x. \tag{4.7}$$

When $T > T_{\mathrm{D}}$, above equation reaches its classical limit,

$$\kappa_{\min} = \frac{1}{2} (\frac{\pi}{6})^{1/3} k_{\mathrm{B}} n^{2/3} \sum_{i=1}^{3} u_{p,g,i} = 0.4 k_{\mathrm{B}} n^{2/3} (u_{p,g,\mathrm{L}} + 2u_{p,g,\mathrm{T}}), \tag{4.8}$$

where n is atomic number density, $u_{p,g,\mathrm{L}}$ is longitudinal and $u_{p,g,\mathrm{T}}$ is transverse phonon speed [33, 34]. This gives $\kappa_{\min} \approx 0.37$ W/m-K using $CoSb_3$ properties and this $\kappa_{\min}$ result is also shown in Fig. 4.6(a).

Starting with κ_L of $CoSb_3$ dominated by phonon-phonon scattering, we consider phonon-point defects scattering and two-phase scattering for the compounds. In Regime I, we considered only point-defects scattering. Using the Matthiessen rule [105], the overall κ_L with the inclusion of phonon-point defects scattering is

$$\frac{1}{\kappa_L(x)} = \frac{1}{\kappa_L(0)} + \frac{1}{\kappa_{L,\mathrm{d}}}. \tag{4.9}$$

Here

$$\kappa_L(x) = \frac{\kappa_L(0)}{1 + c(x)[x(1-x)]^{1/2}}, \tag{4.10}$$

where $c(x)$ is the coefficient for point-defects scattering with respect to x [1, 37, 113, 135, 147], and the results are shown in Fig. 4.6(a) predicting a significant phonon scattering in Regime I. For $\kappa_{L,\mathrm{d}}$, we start with mass fluctuation scattering parameter Γ_s is given by

$$\Gamma_s = \sum x(1-x)[\frac{M(\mathrm{Ba})}{M}]^2, \tag{4.11}$$

where M is the mass of an average ternary cluster ($\mathrm{Ba}_x\mathrm{Co}_4\mathrm{Sb}_{12}$), $M = 4M(\mathrm{Co}) + 12M(\mathrm{Sb}) + xM(\mathrm{Ba})$ with $0 < x < 1$. The lattice thermal conductivity limited by the point-defects scattering $\kappa_{L,\mathrm{d}}$ is

$$\kappa_{L,\mathrm{d}} = \frac{k_\mathrm{B}}{4\pi u_{p,g,\mathrm{A}}(a_1 CT)^{1/2}}, \tag{4.12}$$

where CT is the relaxation time for interphonon scattering. The CT can be estimated from the κ_L of empty CoSb_3 [$\kappa_L(0) = 7.9$ W/m-K from ECMD simulation], i.e.,

$$CT = \frac{(6n)^{1/3} k_\mathrm{B}}{2\pi^{4/3}\kappa_L(0)}, \tag{4.13}$$

where n is the atomic number density. This yields $CT = 4.758\times10^{-16}$ s. The parameter a_1 is the coefficient for the Rayleigh point-defects scattering rate, which is given by

$$a_1 = \frac{V_c \Gamma_s}{4\pi u_{p,g,\mathrm{A}}^3}, \tag{4.14}$$

Table 4.2: Data used in the analytical model of Regime I (point-defects scattering) for various Ba concentrations.

x	M	Γ_s	a_1	$\kappa_{L,\mathrm{d}}$	c	κ_L(W/mK)
0	1696.85	-	-	-	-	7.9
0.02	1699.60	1.28e-04	3.12e-43	30.7	1.83	6.3
0.04	1702.35	2.50e-04	6.10e-43	22.0	1.82	5.8
0.06	1705.09	3.66e-04	8.93e-43	18.2	1.82	5.5
0.08	1707.84	4.76e-04	1.16e-42	15.9	1.82	5.3
0.10	1710.59	5.80e-04	1.42e-42	14.4	1.81	5.1
0.12	1713.33	6.78e-04	1.66e-42	13.4	1.81	4.9
0.14	1716.08	7.71e-04	1.88e-42	12.5	1.81	4.8
0.16	1718.83	8.58e-04	2.09e-42	11.9	1.80	4.7
0.18	1721.57	9.39e-04	2.29e-42	11.3	1.80	4.6
0.20	1724.32	1.02e-03	2.48e-42	10.9	1.80	4.6
0.22	1727.07	1.09e-03	2.65e-42	10.6	1.80	4.5
0.24	1729.81	1.15e-03	2.81e-42	10.3	1.79	4.4
0.25	1731.19	1.18e-03	2.88e-42	10.1	1.79	4.4

where V_c is the unit cell volume. The data are summarized in Table 4.2, and for example, $\Gamma_s(x = 0.5)$ is 1.513×10^{-3}. This value matches that in [147] $\Gamma_s(x = 0.5)$ $= 1.5464 \times 10^{-3}$. $\kappa_L(0) = 7.9$ W/m-K is the average of ECMD results ($x = 0$). The analytical model results for point defects scattering are shown in Fig. 4.6(a).

In the two-phase mixture ($0.25 < x < 0.5$, Regime II), the mixture of two ordered phases (γ and α) creates significant two-phase scattering. Using the Matthiessen rule,

$$\frac{1}{\kappa_L(\mathrm{two-phase})} = \frac{x_\gamma}{\kappa_{L,\gamma}} + \frac{1 - x_\gamma}{\kappa_{L,\alpha}} + \frac{1}{\kappa_{L,\mathrm{d}}}, \tag{4.15}$$

where x_γ is the fraction of γ-phase in a γ-α mixture [135, 113, 37]. This overall two-phase resistivity [κ_L(two-phase)] considers each phase resistivity ($\kappa_{L,\alpha}$ and $\kappa_{L,\gamma}$) and the interfacial resistivity ($\kappa_{L,\mathrm{d}}$) simultaneously. So, we denoted this as two-phase scattering. In this calculation, both phase phonon conductivities, $\kappa_{L,\alpha}$ and $\kappa_{L,\gamma}$, are

from the ECMD simulations. The thermal resistivity due to the interfacial two-phase scattering is derived from $CT = 4.578 \times 10^{-16}$ s, $\Gamma_s \approx 0.0953x(1-x)$, $u_{p,g,\mathrm{A}} = 2934$ m/s [135], $a_1 = 2.326 \times 10^{-40}$, and $1/\kappa_{L,\mathrm{d}} = 0.888[x_\gamma(1-x_\gamma)]^{1/2}$ (m-K/W).

4.3 Results and Discussion

4.3.1 Determination of ground-state structures

We begin with a determination of a temperature composition phase diagram of $\mathrm{Ba}_x\mathrm{Co}_4\mathrm{Sb}_{12}$ by combining *ab-initio* calculations with the CE method and the MC simulations. Thereafter, using ECMD simulations and the Green-Kubo fluctuation-dissipation linear response theory and lattice thermal conductivity decomposition, along with the phase diagram, we predict the lattice thermal conductivity of partially-filled $\mathrm{Ba}_x\mathrm{Co}_4\mathrm{Sb}_{12}$ as a function of concentration and temperature.

A prediction of phase stability at finite temperature requires the use of statistical mechanics to account for entropic contributions to the free energy. The most important source of entropy in a partially-filled skutterudite arises from configurational degrees of freedom associated with all possible ways of distributing Ba and vacancies over the BCC sites of the filler sublattice. A mathematical description of these configurational degrees of freedom is possible with the CE method [173]. An occupation variable σ_i is specified for each Ba site i, which takes a value 1 if the site has a Ba-atom occupant and -1 if it is vacant. The CE is constructed from Eq. (2.1). The $\Gamma_\alpha(\boldsymbol{\sigma})$ are cluster basis functions that form a complete and orthonormal basis within

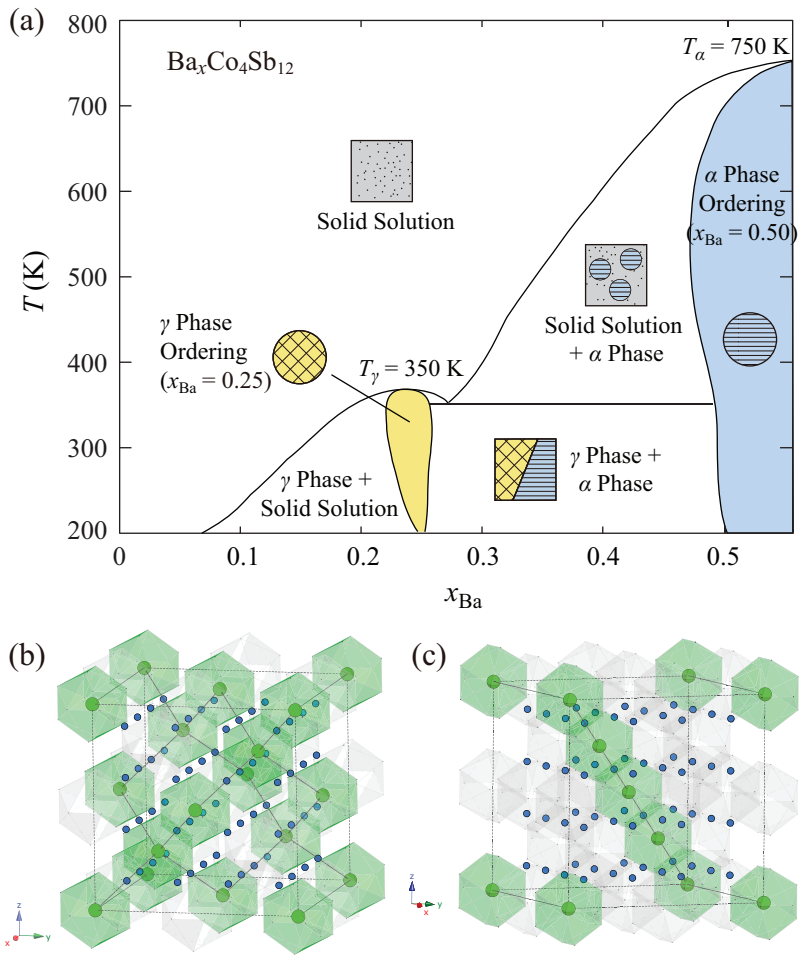

Figure 4.5: (a) The solid-state phase diagram of $Ba_xCo_4Sb_{12}$ showing the order-disorder transition temperatures (T_α and T_γ). (b) Atomic structure of γ and (c) α phases. The Ba atoms (green circles) are shown in the ordered network structures. The Co atoms are shown with small blue circles. To avoid crowding, the Sb atoms at the polyhedron vertices are not shown.

the Ba-vacancy configuration space [173]. The expansion coefficients V_α are referred to as ECI and can be determined from first principles. The CE describes the fully relaxed energy of the crystal as a function of Ba-vacancy order/disorder and can be viewed as a generalized Ising model with physically realistic interaction parameters.

The series in Eq. (2.1) can be truncated to reflect the relatively small contribution from clusters comprised of many sites or those describing long-length scales. As a result, DFT total energy calculations can be used to parameterize the ECI and determine the truncation of the series. This was done using the DFT energies of 28 Ba-vacancy configurations over the filler sites of $CoSb_3$ (see Figs. 4.1 and 4.2).

By applying MC simulations to the cluster expanded Hamiltonian, it is possible to construct a temperature-composition phase diagram. The calculated phase diagram shown in Fig. 4.5(a) exhibits prominent ordered phases at Ba compositions below or near the experimental filling limit ($x \approx 0.44$) [39]; the γ-phase has $x = 0.25$ and the α-phase has $x = 0.5$. As shown in Figs. 4.5(b) and (c), the γ-phase is highly anisotropic with Ba-Ba nearest neighbors along [111] and Ba-vacancy nearest neighbor pairs along the other $\langle 111 \rangle$ family axes; it disorders at $T_\gamma \approx 350$ K. Compared to that, the α-phase has a higher symmetry with the filled Ba sites forming a diamond network; it disorders at $T_\alpha \approx 750$ K. Because all relevant phase transitions are first order, phase coexistence of the two phases can be obtained at intermediate x and low temperature. At higher temperatures coexistence of each phase with a solid solution is obtained.

4.3.2 Prediction of lattice thermal conductivity

The calculation of κ_L, and the interatomic potentials used in the ECMD simulations for the intermediate concentrations of Ba were based on the CRs applied to the empty $CoSb_3$ and fully-filled $BaCo_4Sb_{12}$ potentials from [100].

From Fig. 4.5(a), there are six qualitatively different structural configurations possible for Ba concentrations between $0 \leq x \leq 0.5$, at 300 K: three ordered ground-state structures ($x = 0$, 0.25, and 0.5), a solid solution ($0 < x \leq 0.16$), a mixture of γ-phase and solid solution ($0.16 < x < 0.25$), and a two-phase mixture of ordered phases ($0.25 < x < 0.5$). Figure 4.6(a) shows the predicted κ_L of $Ba_xCo_4Sb_{12}$ as a function of Ba concentrations. As input configurations in the ECMD simulations, we used the ground-state ordered Ba configurations at $x = 0$, 0.25 and 0.5, Ba solid solutions as obtained from MC snapshots ($x = 0.03$ and 0.14) and two-phase mixtures with a single interface (e.g., for $x = 0.38$ ECMD cell consisted of one half having the γ ordering at $x = 0.25$ and the other half having α ordering at $x = 0.5$; $x = 0.33$, 0.38, and 0.44). The results are in good agreement with experiment [39], showing that as the Ba concentration increases, κ_L decreases noticeably. The minimum conductivity relation $\kappa_{\min}$ for amorphous phase is also shown, and this gives $\kappa_{\min} \approx 0.37$ W/m-K using $CoSb_3$ properties. Starting with κ_L of $CoSb_3$ dominated by phonon-phonon scattering, we consider only phonon-point defects scattering and two-phase scattering for the compounds. On the top of Fig. 4.6(a), the state of Ba-vacancy ordering and two-phase mixtures are marked. Since Ba more or less randomly fills the voids of $CoSb_3$ in the solid-solution regime, phonons propagate through the $CoSb_3$

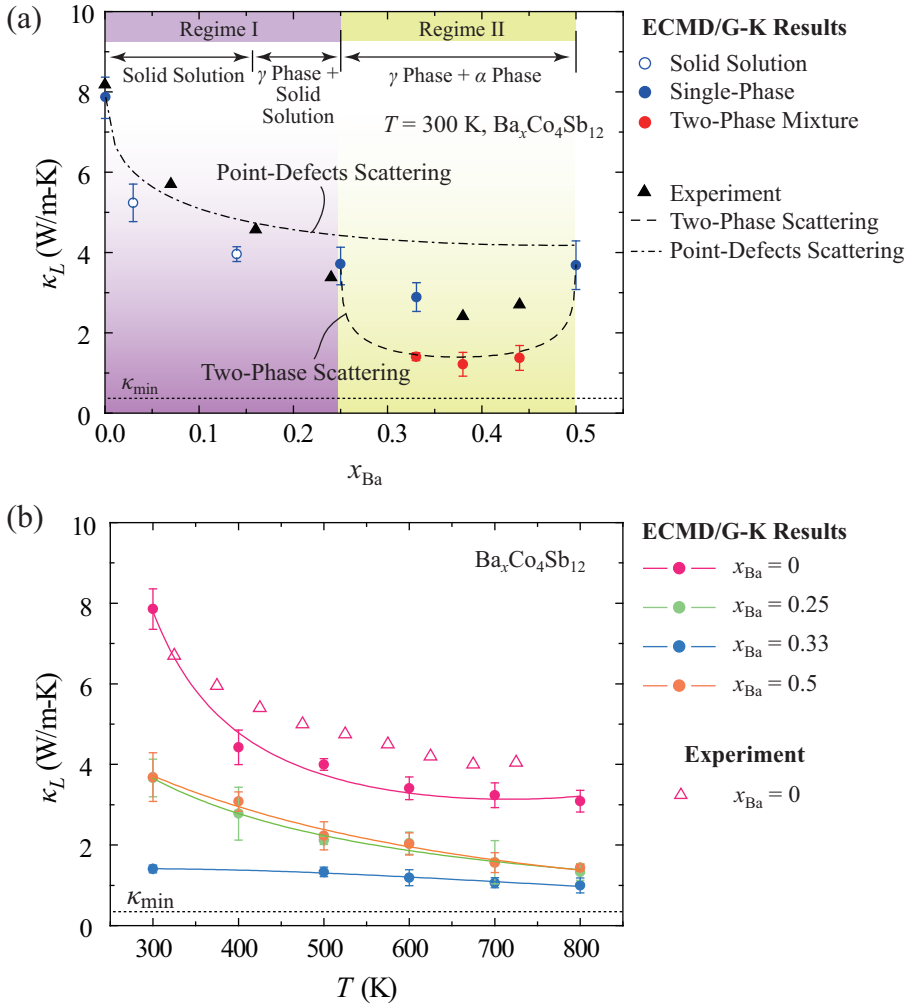

Figure 4.6: Variation of predicted lattice thermal conductivity of $Ba_xCo_4Sb_{12}$. (a) Dependency on various Ba concentration at 300 K. The available experimental results [39], and the results of two analytical models in Section 4.2.4 are also shown. (b) Temperature effects for several fill fractions. The available experimental results for $CoSb_3$ [107] are also shown. All error bars represent the standard errors.

host structure with the randomly distributed Ba atoms acting as point defects. As the phonon-boundary scattering is negligible except at low temperatures, this can persist up to $x = 0.25$ (fully-ordered γ-phase). The overall κ_L with the inclusion of phonon-point defects scattering is given by Eq. (4.10), and results are shown in Fig. 4.6(a) predicting significant phonon scattering in Regime I. In the two-phase mixture ($0.25 < x < 0.5$), the mixture of two ordered phases (γ and α) creates significant interfacial scattering. This overall resistivity includes each phase resistivity ($1/\kappa_{L,\gamma}$ and $1/\kappa_{L,\alpha}$) and the interfacial resistivity ($1/\kappa_{L,\mathrm{d}}$) simultaneously. While isolated point defects scatter phonons due to a point discontinuity in bonding and mass distribution, interfaces between two phases are two-dimensional discontinuities that scatter phonons. This interfacial resistivity had been previously treated the same as the point-defects scattering, so following that we use the treatment of Section 4.2.4, i.e., $1/\kappa_{L,\mathrm{d}} = 0.888[x_\gamma(1-x_\gamma)]^{1/2}$ (m-K/W). We note that a more appropriate model would include the interface concentration and the impedance mismatch between the two phases as in the phonon boundary resistance [180]. Then, we have Eq. (4.15). The dash line in Fig. 4.6(a) is for this two-phase scattering model and is in agreement with ECMD predictions. We note that it is the two-phase mixture causing the significant reduction in κ_L, by comparing with a hypothetical single-phase and the two-phase structures, for $x = 0.33$. The ECMD results for these structures are κ_L(single-phase, one of non-ground states) = 2.9 and κ_L(two-phase) = 1.4 W/m-K [data points and their uncertainties are given in Fig. 4.6(a)]. The point-defects and two-phase scattering are two main reasons for the κ_L reduction in partially-filled structures, compared with the empty structure. We also note that in the empty skutterudites the Umklapp

scattering is important in the overall thermal conductivity as the point-defects and two-phase scattering mechanisms are absent. In Fig. 4.6(a), the ECMD predicted κ_L ($\sim$ 1.0 W/m-K) and the two-phase scattering model show a minimum near $x = 0.38$, and this minimum is close to $\kappa_{\min}$, predicted for the amorphous-phase κ_L.

Figure 4.6(b) shows the predicted κ_L for $x = 0$, 0.25, 0.33, and 0.5, as a function of temperature, along with the experimental results [107]. The transition temperatures (T_α and T_γ) of two ordered phases are marked in Fig. 4.5(a), and at $T = 800$ K there is no ordered structure. So, we use the fully-disordered structures (configuration snapshots of the MC simulations). The single-phase crystal follows the Slack relation ($\kappa_L \sim T^{-1}$ dependence for $T > 0.1T_{\rm D}$) [98, 105, 185], while the two-phase mixtures reaches a plateau, similar to amorphous solid $\kappa_{\min}$ [105]. This reconfirms that the two-phase mixtures can be considered as pseudo-amorphous structures with significant reduction in κ_L for such crystalline TE materials.

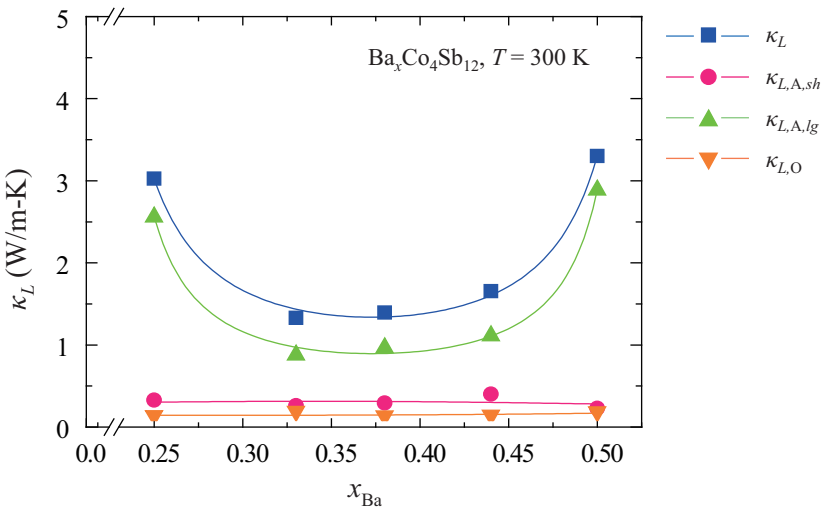

Figure 4.7: Lattice thermal conductivity decomposition and their variations with respect to Ba concentrations. Decompositions were done using singular ECMD simulation results - each concentration [as compared to Figs. 4.6(a) and (b) where average over several simulations was used].

In general, the heat is carried through skutterudites mostly by the acoustic phonons, which are altered by the presence of this fillers [39, 43, 100, 115]. This significantly reduces κ_L for the two-phase mixtures and is also confirmed in an analysis of a decomposition of κ_L into the short-, long-range acoustic, and optical phonon components [105], Eq. (3.8). After removing the high-frequency components of HCACF with the Fourier low-pass filter ($f_{\text{cut}-\text{off}} = 1.5$ THz determined from the acoustic phonon dispersion results), the low-frequency acoustic portion are fitted with two exponential decay terms. Each component of HCACF in Eq. (3.8) was then integrated independently and Fig. 4.7 shows the results. The long-range acoustic phonon contribution is dominant and most affected by Ba concentrations, while the short-range acoustic and optical components are not. The $\kappa_{L,\text{A},lg}$ decreases most noticeably by the two-phase scattering in the two-phase regime.

4.4 Summary

Our ECMD calculations indicate that in order to find a high-performance skutterudite-based TE materials, one can greatly benefit from the presence of order-disorder phase transitions of the filler species in the voids of the skutterudite structure, which leads to two-phase coexistence and the presence of interfaces.

Chapter 5

Cage-Breathing Lattice Dynamics of Substituted Skutterudites

5.1 Introduction

Filling structural cages in the $CoSb_3$ skutterudite crystal has lowered the lattice thermal conductivity [139, 186], making filled skutterudites one of the best novel TE materials for mid-temperature power generation applications [121, 177, 201]. An alternative approach to lowering thermal conductivity is to distort the near-square pnicogen (e.g., Sb) atomic rings, which are a characteristic feature of the skutterudite structure, $Im3(T_h^5)$ [149]. Since vibration modes involving Sb rings dominate the spectrum of heat-conducting phonons [52, 70], distortions of the rings should be particularly effective in disrupting heat transport. A charge-compensated alloy (see Fig. 5.1) can be obtained by substitution of IV-VI species (e.g., Sn-Te [123] or Ge-Te [193, 194]), which has recently been shown to enhance Te solubility and, in the

case of Ge-Te, imbalanced Ge/Te induces formation of finely dispersed Ge-Te-rich skutterudite nanodots in the Sb-rich matrix. The enhanced point-defect scattering and presence of nanoinclusions in these double-substituted skutterudites enabled them to attain a TE figure-of-merit (ZT) of 1.1, competitive with the best values for single-filled skutterudites.

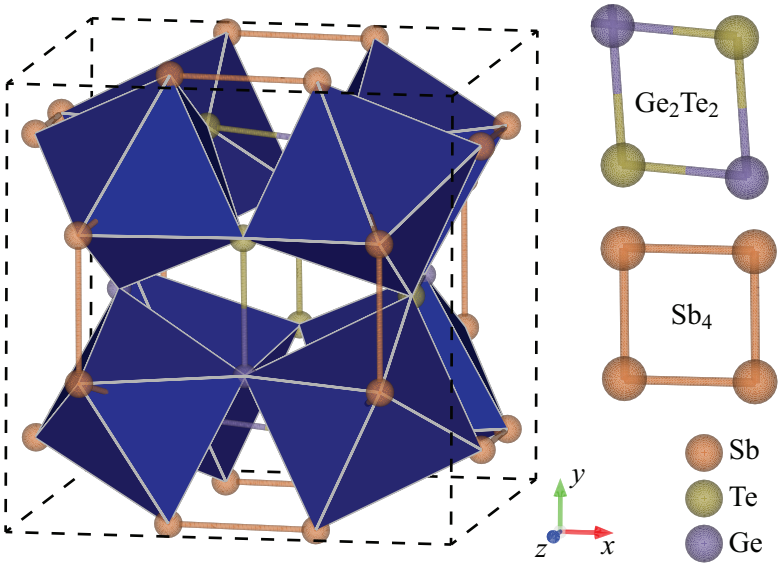

Figure 5.1: A typical crystal structure (left) of double-substituted skutterudite $CoSb_{3(1-x)}Ge_{1.5x}Te_{1.5x}$ at $x = 0.5$, which mixes a variety of rings (right) of counter-diagonal Ge_2Te_2 and Sb_4. Orange, chartreuse, and purple spheres represent Sb, Ge, and Te respectively.

The goal of this chapter is to understand the lattice dynamics of double-substituted skutterudite $CoSb_{3-m-n}Ge_mTe_n$ using DFT calculations (including *ab-initio* molecular dynamics AIMD). Extensive computational and analytical works on low energy structures reveal a compelling theoretical puzzle surrounding the role of pnicogen rings in skutterudite heat transport.

Table 5.1: Calculated properties of $CoSb_3$ and $CoGe_{1.5}Te_{1.5}$. The literature results for $CoSb_3$ are also listed. T_D, γ_G, B, C_{ij}, and c_v are the Debye temperature, the Grüneisen parameter, bulk modulus, elastic constant, and specific heat capacity.

	T_D (K)	γ_G	B (GPa)	C_{11} (GPa)	C_{44} (GPa)	c_v (J/mol-K)
$CoSb_3$	305.9	1.11	91.89	174.6	66.34	22.9
$CoGe_{1.5}Te_{1.5}$	283.5	1.28	55.87	125.6	29.35	22.9
Ref., $CoSb_3$	307 [35, 135]	0.95 [35]	82 [222]	158 [222]	57 [222]	-

5.2 Calculation Methods

5.2.1 Phonon calculations

The `VASP` [116] and `PHONON` [151] codes were used for the *ab-initio* phonon calculations. The `VASP` calculation were performed with the PBE parameterization of the GGA for exchange and correlation [154] and using the PAW method [26, 117]. Details are given in Section 2.3. All phonon and thermodynamic properties (Table 5.1, with literature results for $CoSb_3$ also listed [35, 135, 222]) are predicted using a fit of interatomic force constant tensors to the calculated HF forces. Diagonalization of the dynamical matrix yields the phonon dispersion, from which density of states and atomic displacement tensors are obtained. The trace of the diagonalized atomic displacement tensor is the atomic displacement parameter (ADP), a scalar measure of single-atom vibration amplitude based on finite-temperature phonon mode occupancy.

5.2.2 AIMD simulations

The lattice thermal conductivity using NEAIMD is computed as the ratio of an applied heat flux to the resulting temperature gradient [190, 207], Eq. (2.29). Details are given in Section 2.5.2. For simulations we use the `VASP` code modified to perform NEAIMD-energy exchange [103, 142] as reported in [190, 207]. The simulations are performed on supercells of 192 atoms (3×1×2) and 384 atoms (6×1×2), constructed as a solid-solution of pnicogen rings, based on the phase diagram of [41]. We equilibrate each simulation using EAIMD for 1 ps with 0.5 fs time steps. Equilibration is followed by 22 ps of NEAIMD using a 1 fs time step. This duration proved sufficiently long to obtain converged lattice thermal conductivity. Because the exchange of kinetic energy results in non-Newtonian dynamics in the hot and cold sections, only the linear portion of the temperature gradient is considered in calculating the lattice thermal conductivity.

5.3 Results and Discussion

5.3.1 Lattice dynamics of configured pnicogen rings

Based on the phase diagram calculation given in [41], the strong energetic preference for short-range order of Ge/Te substituted on the pnicogen sublattice and charge-balanced (i.e., counter-diagonal) rings are predicted. In here, we have focused our investigation of heat transport mechanisms on the charge-balanced $CoSb_{3(1-x)}Ge_{1.5x}Te_{1.5x}$ alloy.

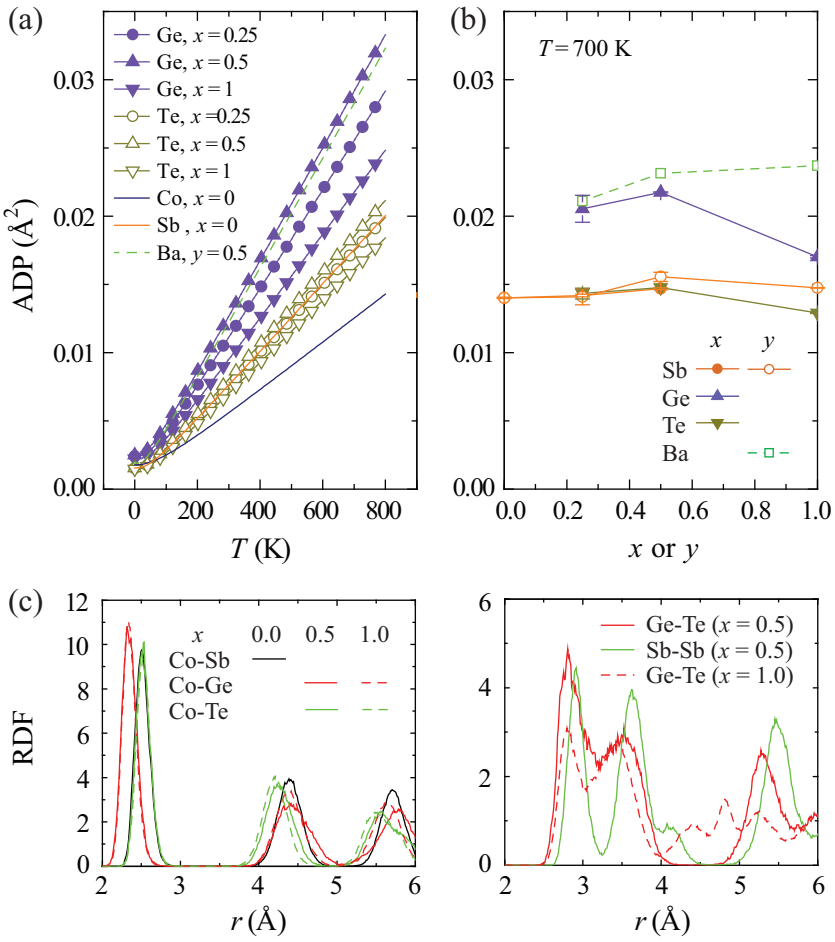

Figure 5.2: (a) Temperature and (b) composition dependence of atomic displacement parameter for individual atoms in $CoSb_{3(1-x)}Ge_{1.5x}Te_{1.5x}$ and $Ba_yCo_4Sb_{12}$. (c) The radial distribution functions of the octahedron (upper) and pnicogen ring (bottom) bonds are shown.

The ADP values of various low-energy configurations of $CoSb_{3(1-x)}Ge_{1.5x}Te_{1.5x}$ containing counter-diagonal Ge_2Te_2 rings (x = 0.25, 0.5 and 1) are shown in Figs. 5.2(a) and (b). Due to the strong covalent bonds of the rings, the ADPs of substitutional atoms are not expected to be large. Surprisingly, the calculated ADP of Ge is significantly larger than that of Sb for all three low-energy configurations considered at x = 0.25 and 0.5. For comparison, Figs. 5.2(a) and (b) shows values for the Ba-filled skutterudite $Ba_yCo_4Sb_{12}$ at several values of y. The large ADP of the Ba filler atom, relative to most atoms on the pnicogen rings, indicates the rattling behavior of Ba. The rattling behavior of the Ba filler species is believed to cause a reduction in the lattice thermal conductivity of partially-filled skutterudites. The RDFs obtained from EAIMD also show the large displacement of Ge substitutional atoms. Comparing with the RDFs of Sb atoms, as shown in Fig. 5.2(c), those of Ge atoms are broadened and shifted while those of Te atoms are not changed. These observations are clearly verified the RDFs of different structural view-points (i.e., octahedra and pnicogen rings).

While the Ge ADP is large for all compositions, it is maximized at x = 0.5 where it becomes comparable to that of a Ba filler atom. This suggests that Ge atoms on the counter-diagonal Ge_2Te_2 ring could play a similar role as a rattler. As reported in references [20, 53, 115] rattler species inhibit heat transport by both (i) reducing average vibrational frequencies via local bond-softening, and (ii) giving rise to low-frequency "guest" vibrational modes decoupled from the host crystal. In addition to having a large ADP, Ge exhibits similar projected phonon dispersion curves to those of Ba, as shown in Figs. 5.3 and 5.4. Phonon modes arising predominantly

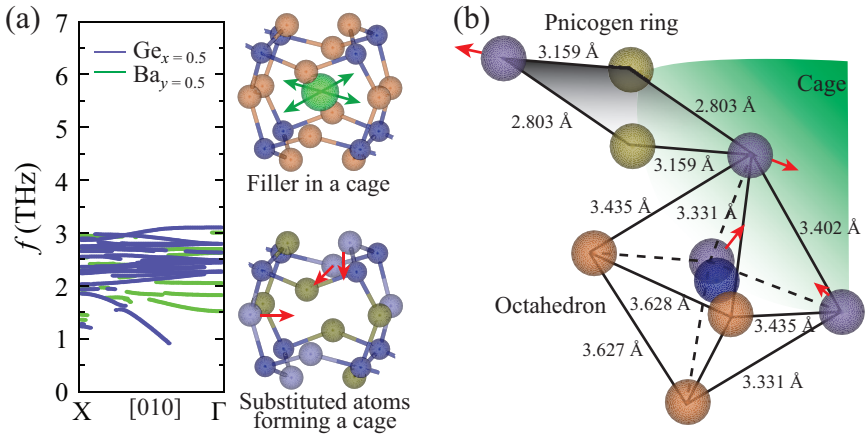

Figure 5.3: (a) Projected phonon dispersion curves for $x = 0.5$ and $y = 0.5$ using DFT. Atomistic configurations of each vibration mode for filler and double-substitution are also shown. Blue and green spheres represent the Co and Ba filler atoms respectively. (b) Atomistic configurations showing a pnicogen ring and octahedron consisting of substituted atoms ($x = 0.5$).

from either Ba or Ge displacements show negligible dispersion, characteristic of local deformational modes with low group velocity (see the color maps of sound speed in Fig. 5.4).

Note that full phonon dispersion curves and phonon density-of-states (D_p) of various substituted and filled compounds [$CoSb_{3(1-x)}Ge_{1.5x}Te_{1.5x}$ and $Ba_yCo_4Sb_{12}$] are shown in Fig. 5.4. In spite of this similarity to Ba filler, the collective modes of substituted Ge deform different segments of the skutterudite crystal structure and have different modal frequencies [i.e., Fig. 5.3(a) for Ge and Ba show 2.27 and 1.52 THz at Γ; 1.24 and 1.45 THz at X]. Additionally, the dominant vibrational distortions of Ge responsible for its large ADP are along the diagonal of the counter-diagonal Ge_2Te_2 rings, as illustrated in Fig. 5.3(b). Collectively, this corresponds to a breathing mode (i.e., expansion/shrinkage) of the cage [see Fig. 5.3(a)]. We consider whether the distinct highly-displaced Ge modes and rattler modes of Ba

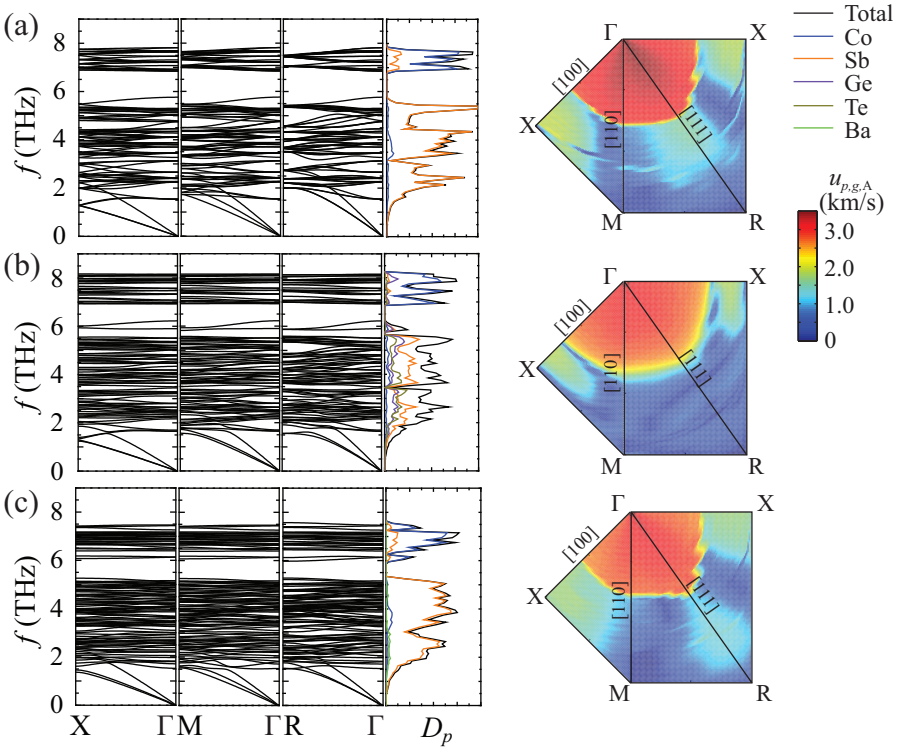

Figure 5.4: Calculated phonon dispersion curves, phonon density-of-states, and sound speed for (a) $x = 0$, (b) 0.5, and (c) $y = 0.5$. The site-projected density-of-states are also shown.

can influence the phonon transport by simultaneously affecting different portions of the phonon spectrum. Our preliminary *ab-initio* calculations show this hybrid skutterudite structure ($x = 0.5$ and $y = 0.5$, which is close to the filling limit [179]), will retain these distinct features. In particular, our results indicate mode flattening in specific direction (Ge at X; Ba at Γ), overall phonon downshift (Ba), and distinct softening induced in the guest vibrational mode frequencies.

5.3.2 Prediction of lattice thermal conductivity

Experimental measurements [41] on charge-balanced $CoSb_{3(1-x)}Ge_{1.5x}Te_{1.5x}$ solid solutions show a dramatic decrease in the thermal conductivity with increasing x,

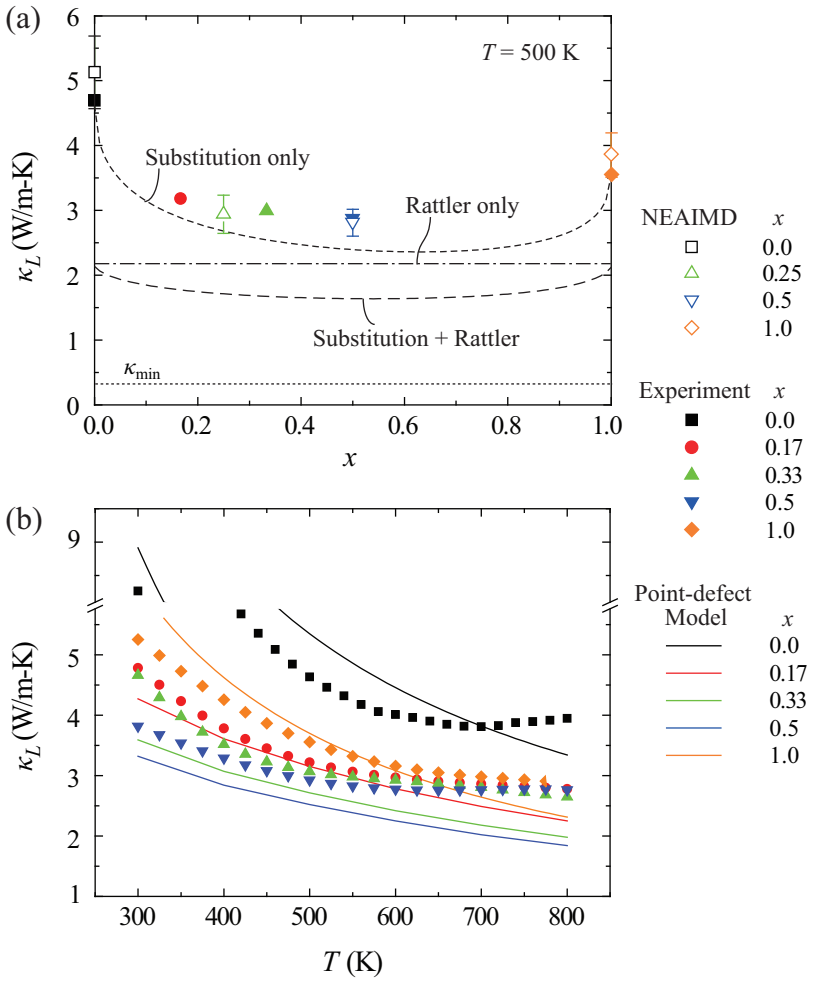

Figure 5.5: Variations of the predicted lattice thermal conductivity of $CoSb_{3(1-x)}Ge_{1.5x}Te_{1.5x}$, (a) concentration dependence at $T = 500$ K, and (b) temperature dependence for several compositions. The experimental results [41] (using the Wiedemann-Franz law) and the results of the point-defect model and NEAIMD are shown. The minimum conductivity κ_{min} (~ 0.37 W/m-K) for the amorphous $CoSb_3$ phase [111] is also shown.

as shown in Fig. 5.5(a). In fact, the minimum in the measured κ_L near $x = 0.5$ coincides with the maximum of the calculated Ge ADP. The total measured thermal conductivity can be decomposed as $\kappa = \kappa_L + \kappa_e$, where κ_L and κ_e are the lattice and electronic thermal conductivity, respectively. An experimental value of κ_L is calculated by approximating and subtracting κ_e which, in turn, is determined from the Wiedemann-Franz law. Here $\kappa_e = N_{\mathrm{L},\circ}\sigma_e T$, where σ_e is the measured electrical conductivity and $N_{\mathrm{L},\circ}$ is the Lorenz number, determined from the experimental Seebeck coefficient by assuming a single parabolic band [81]. The experimental value of κ_L obtained in this way, which Fig. 5.5(a) shows for several compositions at 500 K, quickly decreases with initial substitution before reaching a plateau at intermediate composition. The temperature dependence of κ_L, shown in Fig. 5.5(b), exhibits a decreasing trend at all compositions.

In order to analyze the effect of pnicogen ring substitution on κ_L, we use experimentally- and DFT-parameterized analytical models for phonon-phonon and point-defect scattering [1, 37, 111, 113, 135, 147], as well as NEAIMD simulations [190].

Starting with κ_L of $CoSb_3$ and $CoGe_{1.5}Te_{1.5}$, which are dominated by phonon-phonon scattering, we add an analytical factor for point-defect scattering at intermediate alloy compositions [1, 37, 105, 111, 147]. Using the Matthiessen rule [105], the overall κ_L with the inclusion of the point-defect scattering [100, 111] is

$$\frac{1}{\kappa_L(x,T)} = \frac{x}{\kappa_L(0,T)} + \frac{1-x}{\kappa_L(1,T)} + \frac{1}{\kappa_{L,\mathrm{d}}}. \tag{5.1}$$

Here $\kappa_L(0,T)$ and $\kappa_L(1,T)$ are obtained from the Slack relation [98, 105, 185],

$$\kappa_{L,\mathrm{S}}(T) = \frac{3.1 \times 10^4 \langle M \rangle V_\circ^{1/3} T_{\mathrm{D},\infty}^3}{T \langle \gamma_\mathrm{G}^2 \rangle N^{2/3}}, \tag{5.2}$$

where $\langle M \rangle$ is the average atomic weight, N is the number of atoms, $V_\circ$ is the average volume per atom, $T_{\mathrm{D},\infty}$ is the Debye temperature, and $\langle \gamma_\mathrm{G} \rangle$ is the average Grüneisen parameter. For the $\kappa_{L,\mathrm{d}}$, the point-defect scattering parameter Γ_s, including mass fluctuation and atomic displacement [1, 22, 143, 191] is

$$\Gamma_s = x(1-x)[(\frac{\Delta M}{M})^2 + 3\gamma_\mathrm{G}^2(\frac{\Delta R}{R})^2], \tag{5.3}$$

where M is the molecular weight of the $CoSb_{3(1-x)}Ge_{1.5x}Te_{1.5x}$ alloy and R is the average atomic radius. The lattice thermal conductivity limited by the point defect scattering $\kappa_{L,\mathrm{d}}$ is

$$\kappa_{L,\mathrm{d}} = \frac{k_\mathrm{B}}{4\pi u_{p,g,\mathrm{A}} (a_1 CT)^{1/2}}, \tag{5.4}$$

where CT is the relaxation time for phonon-phonon scattering including normal, N-processes, and U-processes. Here CT can be estimated from the experimentally-determined $\kappa_L(0,T = 300\ \mathrm{K})$ of 8.3 W/m-K for $CoSb_3$. Using

$$CT = \frac{(6n)^{1/3} k_\mathrm{B}}{2\pi^{4/3} \kappa_L(0)}, \tag{5.5}$$

where n is the atomic number density, yields $CT = 4.758 \times 10^{-16}$ s [111]. The param-

eter a_1 is the coefficient for the Rayleigh point-defects scattering rate, given by

$$a_1 = \frac{V_c \Gamma_s}{4\pi u_{p,g,\mathrm{A}}^3}, \tag{5.6}$$

where V_c is the unit cell volume. To clarify this effect with a rattler, the analytical results for the partially-filled ($y = 0.5$) and for the hybrid structure (various x with $y = 0.5$) are also shown in Fig. 5.5(a). Here the overall κ_L is given as [100, 111]

$$\frac{1}{\kappa_{L,y=0.5}(x,T)} = \frac{x}{\kappa_{L,y=0.5}(0,T)} + \frac{1-x}{\kappa_{L,y=0.5}(1,T)} + \frac{1}{\kappa_{L,\mathrm{d}}}, \tag{5.7}$$

assuming $\kappa_{L,y=0.5}(0,T)$ is equal to $\kappa_{L,y=0.5}(1,T)$. Here $\kappa_{L,y=0.5}(0,T)$ is obtained from the classical molecular dynamics results in [111]. Using this combined strategy (see Fig. 5.3.2), we predict a further 33% reduction in κ_L (much closer to the theoretical minimum, $\kappa_{\min}$, of an amorphous phase).

The juxtaposition of the point-defect scattering model and our experimental measurements in Figs. 5.5(a) and (b) indicates favorable agreement between the two, suggesting that the reduction in κ_L at intermediate substitution composition can largely be attributed to scattering from point-defects, which take the form of mass disorder and local atomic relaxations. Our analytical model does not account for the effect of bipolar carrier transport in our calculation of κ_e, likely resulting in overestimation of experimental κ_L values at high temperature. As shown in Figs. 5.5(a) and (b) the NEAIMD prediction agrees with experimental and analytical results.

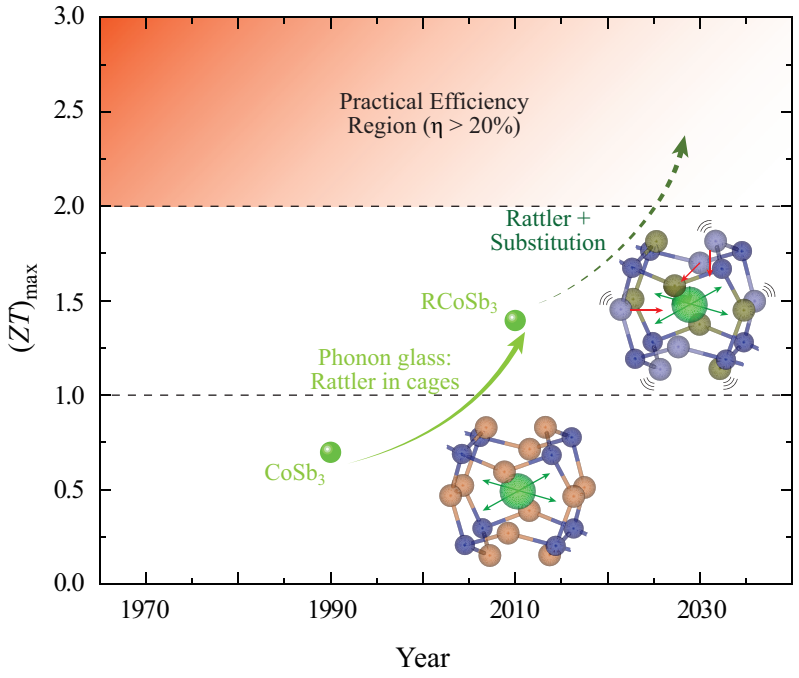

Figure 5.6: The change of $(ZT)_{\max}$ as a function of time. New skutterudite design (or mechanism) proposed in this chapter is also shown.

5.4 Summary

We have demonstrated that Ge/Te double substitution on pnicogen rings is an effective means of lowering the lattice thermal conductivity of skutterudites. Although comparable in magnitude to the filler effect, substitution targets vibrational modes are qualitatively different from those of fillers. So, we expect a combination of the filler and substitution is likely to act in a complementary manner in suppressing the thermal conductivity. This combined strategy (see Fig. 5.3.2) should therefore lead to even lower thermal conductivity and higher ZT values than have been realized using either strategy separately.

Chapter 6

Coupled Polaron and Phonon Effects of Boron Carbides

6.1 Introduction

Widely used boron carbides ($B_{12+x}C_{3-x}$), e.g., in refractories, abrasives, thermoelectrics, nuclear reactors [54], have much unexplained structural and carrier transport properties. Their primitive cell ($R3m$ space group, rhombohedral representation) contains an icosahedron of twelve atoms with strong covalent chains connecting them, as shown in Fig. 6.1(a) [54]. They are very similar to the pure α-B_{12} structure [see Fig. 6.1(b)], with an icosahedron and polar linkers, however the inter-icosahedral bonds are changed with the addition of carbon. So, boron carbides are hard solids with the melting temperature of $\sim$ 2600 K [13, 54, 62]. Due to their polymorphism, their crystal structure identification is still evolving [119], and they have high p-type carrier density ($\sim 10^{21}$ cm^{-3}) [15, 62]. Odd number of B atoms (e.g., $x = 1$) removes bound

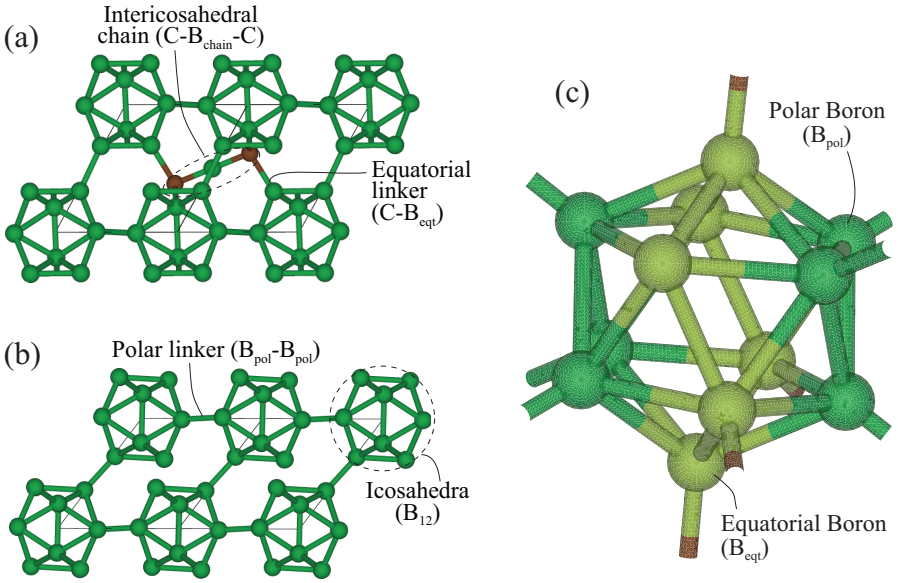

Figure 6.1: The crystalline structure of boron-related compounds (B = green, C = brown) : A primitive cell of (a) $B_{13}C_2$ and (b) pure α-B_{12}, and (c) the magnified view of a B_{12} icosahedron in $B_{13}C_2$ showing two different borons, the polar (B_{pol}; yellowish green) and the equatorial (B_{eqt}; dark green) atoms.

electrons, produces hole-like carriers (one hole per primitive cell) and the high hole density, while stoichiometric compounds $B_{12+x}C_{3-x}$ have moderate carrier density [13, 64]. Their hardness and carrier density suggest large thermal conductivity ($\kappa = \kappa_e + \kappa_L$, dominated by lattice thermal conductivity κ_L), high electrical conductivity (σ_e), and small Seebeck coefficient (α_S), but they have small κ_L and large α_S, both nearly temperature independent [14, 15, 30, 215]. Also, the small σ_e exponentially increases with temperature [14, 30].

To explain these anomalous properties, two models have been suggested by Emin *et al.* [15, 62, 66, 214]and Werheit *et al.* [119, 211]. The first is the small bipolaron model for the nonequivalent $B_{11}C$ icosahedra, suggesting localized charge (q_e) carriers with low mobility, i.e., phonon-assisted polaron hopping. The second model is based on structural disorder in B_{12}-(C-B-C), where the high density intrinsic de-

fects accompanied by strong distortion compensate for the electron deficiency of ideal metallic behavior and also reduce κ. This structural conjecture is still evolving with the mentioned polymorphism [54, 211], as reported in the phase diagram and diffraction results demonstrating the abundances of phases [54]. The $B_{11}C$-(C-B-C) model is believed to be the lowest formation energy and the most relevant structure for $x = 0$, whereas the B_{12}-(C-B-C) is the most stable phase for $x = 1$ [36, 54, 203]. Those structural models are verified from the formation energy calculation using the DFT [32, 36, 203]. Here we consider α-B_{12} and $B_{13}C_2$ structures containing a B_{12} icosahedron and a C-B-C inter-icosahedral chain, since they are the ground-state structures from the energetic (thermodynamic) perspective and because there is a distinct structural evolution with added carbon.

In this chapter, we present a comprehensive theoretical/computational analyses of the polaron formation and phonon softening in $B_{13}C_2$, using *ab-initio* methods. We predict/explain the temperature independencies of α_S (including entropy analysis of various contributions) and κ_L, and compare with available experimental results. Our results show such anomalous behaviors are caused by polaron and phonon evolutions due to the unique icosahedra and inter-icosahedral chains in $B_{13}C_2$.

6.2 Calculation Methods

6.2.1 DFT calculations

We begin with the electronic structure and lattice dynamics using various DFT calculations implemented in the `VASP` [116] and `PHONON` [151] codes. The PBE parameterization of the GGA for the exchange-correlated functional [154] and the PAW method for modeling core electrons (energy cutoff = 520 eV) [26, 117] are used. Details are given in Sections 2.2 and 2.3. The high-temperature lattice dynamics are investigated by EAIMD. The temperature-dependent phonon density-of-states are also obtained from EAIMD and the Fourier transform of the velocity autocorrelation function over 22 ps. EAIMD simulations are performed on supercells consisting of 180 atoms. Considering thermal expansion, we prepare supercells with the experimental thermal expansion coefficient ($\alpha = 5.73\times10^{-6}$/K for 300 to 1970 K) [198] and lattice parameter ($a = 5.63$ and $c = 12.16$ Å at $T = 300$ K) [54, 198] are used. The Brillouin zone is sampled at the gamma point. After constant-temperature simulations with the Nosé thermostat for 1 ps (0.5 fs time steps) reaching equilibrium, we collect atomic trajectories for 22 ps (1 fs time steps).

To predict α_{S} and κ_L, we use the NEAIMD simulations. For non-equilibrium simulations, we use the `VASP` code modified to perform NEAIMD-energy exchange [103, 142] as reported in [190, 207]. As given in Eq. (2.29), the heat flux is imposed by dividing the simulation cell into sections of equal width, and exchanging kinetic energy (velocity swapping) between the hot and cold sections. Details are given in Section 2.5.2. For further validation on the charge associated with each atom in the

simulation cell (hot to cold), the Bader analysis [91] of charge-density grid is used with the DFT charge density. NEAIMD simulations are performed on (hexagonal representation) supercells consisting of 180 (hexagonal 2×1×2 supercell), 270 (2×1×3 supercell), and 360 (2×1×4 supercell) atoms. Structure preparations are same with EAIMD simulations. We carry out constant-temperature simulations using a Nos*é* thermostat for 1 ps (0.5 fs time steps). After reaching equilibrium, a non-equilibrium calculation is performed for 22 ps (1 fs time steps).

The electron-phonon (*e*-*p*) coupling parameter is calculated from the self-consistent change in the potential of electrons interacting with a phonon mode implemented in the `Quantum-ESPRESSO` [75] package with norm-conserving pseudopotential and a plane-wave cutoff energy of 40 Ry. Fully-relaxed structures are simulated with an electron-momentum mesh of 8×8×8 and a 4×4×4 phonon-momentum mesh grid. The calculation details of the *e*-*p* coupling parameter are presented in Section 2.4. The Eliashberg spectral function $\alpha^2F(\omega)$ [29, 36, 157], the effectiveness of phonon with energy $\hbar\omega$ to scatter electrons, is defined as Eq. (2.14).

6.2.2 Entropy and energy analyses of Seebeck coefficient

The overall α_{S} can be expressed as sum of various contributions,

$$\alpha_{\mathrm{S}} = \alpha_{\mathrm{S,mix}} + \alpha_{\mathrm{S,spin}} + \alpha_{\mathrm{S,vib}} + \alpha_{\mathrm{S,trans}}, \tag{6.1}$$

where the right hand side terms are: change of entropy-of-mixing, spin entropy, vibrational entropy upon adding a charge carrier, and the net energy transferred in

moving a carrier (divided by q_eT), respectively [63]. Each carrier mostly contributes to α_{S} in different way and specific conditions, however they are highly coupled and interacting with phonon.

The mixing contribution to $\alpha_{\mathrm{S,mix}}$ is usually related with electron and dominant in lightly-doped semiconductors. The $\alpha_{\mathrm{S,mix}}$ is then related to the change of mixing entropy S_{mix} upon adding a carrier:

$$\alpha_{\mathrm{S,mix}} = \frac{1}{q_e}\frac{\partial S_{\mathrm{mix}}}{\partial N} = \frac{k_{\mathrm{B}}}{q_e}\ln(\frac{1-f_e^{\circ}}{f_e^{\circ}}), \tag{6.2}$$

where k_{B} is the Boltzmann constant and $f_e^{\circ} = N/N_A$ is the ratio of electrons to sites (Fermi function) [64, 63, 105]. The spin entropy S_{spin} contribution to α_{S} is

$$\alpha_{\mathrm{S,spin}} = \frac{\Delta S_{\mathrm{spin}}}{q_e} = \frac{k_{\mathrm{B}}}{q_e}\ln(\frac{2s+1}{2s_{\circ}+1}), \tag{6.3}$$

where $s_{\circ}$ and s are net spins of the magnetic site in the absence and presence of the spin carrier [63, 64].

For the $\alpha_{\mathrm{S,vib}}$, reducing the local vibrational frequencies (phonon softening) increases the vibrational entropy (S_{vib}). The full crystal Hamiltonian (H) for the vibrational part of the energy is obtained by adding the potential and kinetic energy. We write the Hamiltonian (for the quantum-harmonic oscillator) as [105]

$$\mathrm{H}_{\mathrm{vib}} = \sum_{k_p}\hbar\omega(k_p)(f_p^{\circ}+\frac{1}{2}), \tag{6.4}$$

where f_p° is the equilibrium occupancy of phonon. $\mathrm{H}_{\mathrm{vib}}$ is used to solve analytically for

thermodynamic properties, e.g., the free energy $F_{\rm vib}$ is -$k_{\rm B}T$ ln[$\sum$exp(-$\rm H_{vib}$/$k_{\rm B}T$)], where the entropy is $S_{\rm vib}$ = -$\partial F_{\rm vib}/\partial T$. The phonon density-of-states gives the number of modes with the frequency in the interval [ω, ω + dω], and first-order contribution to the $\alpha_{\rm S,vib}$ is [15, 63, 64, 66]

$$\begin{aligned}\alpha_{\rm S,vib} &= \frac{1}{q_e}\sum_i \frac{\partial S_{{\rm vib},i}}{\partial \omega_i}\Delta\omega_i \\ &= \frac{k_{\rm B}}{q_e}\sum_i (\frac{-\Delta\omega_i}{\omega_i})[\frac{\hbar\omega_i/2k_{\rm B}T}{\sinh(\hbar\omega_i/2k_{\rm B}T)}]^2. \end{aligned} \tag{6.5}$$

From the high-temperature limit ($k_{\rm B}T \gg \hbar\omega$) and series expansions of the hyperbolic functions, the vibrational contribution to $\alpha_{\rm S}$ is $\alpha_{\rm S,vib}$ = ($k_{\rm B}/q_e$)$\sum_i$(-$\Delta\omega_i/\omega_i$). To calculate the transport Seebeck component $\alpha_{\rm S,trans}$ related with the phonon-assisted hopping, additionally, we start from $\alpha_{{\rm S,trans},ep} = E_T/q_eT$, where subscript ep means polaron and E_T is the net vibrational energy that accompanies a phonon-assisted hopping, i.e., [15, 61, 64, 66]

$$E_T = \frac{k_{\rm B}T^2}{2}[\frac{\partial \ln(\dot\gamma_{1,2}/\dot\gamma_{2,1})}{\partial T_1} - \frac{\partial \ln(\dot\gamma_{1,2}/\dot\gamma_{2,1})}{\partial T_2}]_{T_1=T_2=T}. \tag{6.6}$$

Here $\gamma_{1,2}$ (and $\gamma_{2,1}$) are the hopping rates between site 1 to site 2 at temperatures T_1 and T_2. Using the binding energy relation with the local stiffness [15, 63, 64, 66], we have

$$E_T = E_a\sum_i (\frac{-\Delta\omega_i}{\omega_i})\frac{\hbar\omega_i/2k_{\rm B}T}{\sinh(\hbar\omega_i/2k_{\rm B}T)}. \tag{6.7}$$

In this chapter, we approximate that $\alpha_{\rm S,vib}$ and $\alpha_{\rm S,trans}$ are the dominant contribution, since $\alpha_{\rm S,mix}$ and $\alpha_{\rm S,spin}$ are estimated to be negligible. These are justified due

to heavy carrier density and non-ferromagnetic property for $B_{13}C_2$.

6.3 Results and Discussion

6.3.1 Lattice dynamics and polaron formation

To understand the vibrational behavior of $B_{13}C_2$, we begin with their lattice dynamics and electronic structures using various DFT methods. Based on Figs. 6.2(a) to (c), three distinctive features (or unconventional bond behaviors) are observed in within the $B_{13}C_2$ structure. (i) Since the bond length is inversely related to the bond stiffness [105], the inter-icosahedral C-B-C chain bonds are the most rigid ones (stronger than the intra-icosahedral and the polar-linker bonds). (ii) With increase in temperature, the bond angle of the C-B-C chain (θ_{chain}) surprisingly decrease while its bond length (r_{chain}) become longer and the polar linker bonds are almost constant. So, the B_{chain} atoms, the central atom of the most rigid bond, have a large vibrational degree-of-freedom and this increases with temperature. (iii) Significant lattice distortion of the B_{12} icosahedra is observed. These intra-bonds (e.g., B_{pol}-B_{pol}, B_{eqt}-B_{eqt}, and B_{pol}-B_{eqt}) do not monotonically increase and are distorted as temperature increases. These findings are useful in explanation of the lattice distortion and formation of polaron formation, as will be discussed later.

Figure 6.3 shows total and projected phonon dispersion curves using small displacement method in the harmonic approximation. As we expected, $B_{13}C_2$, a hard solid material, has high phonon energy (up to 200 meV) showing its rigid bonds. As

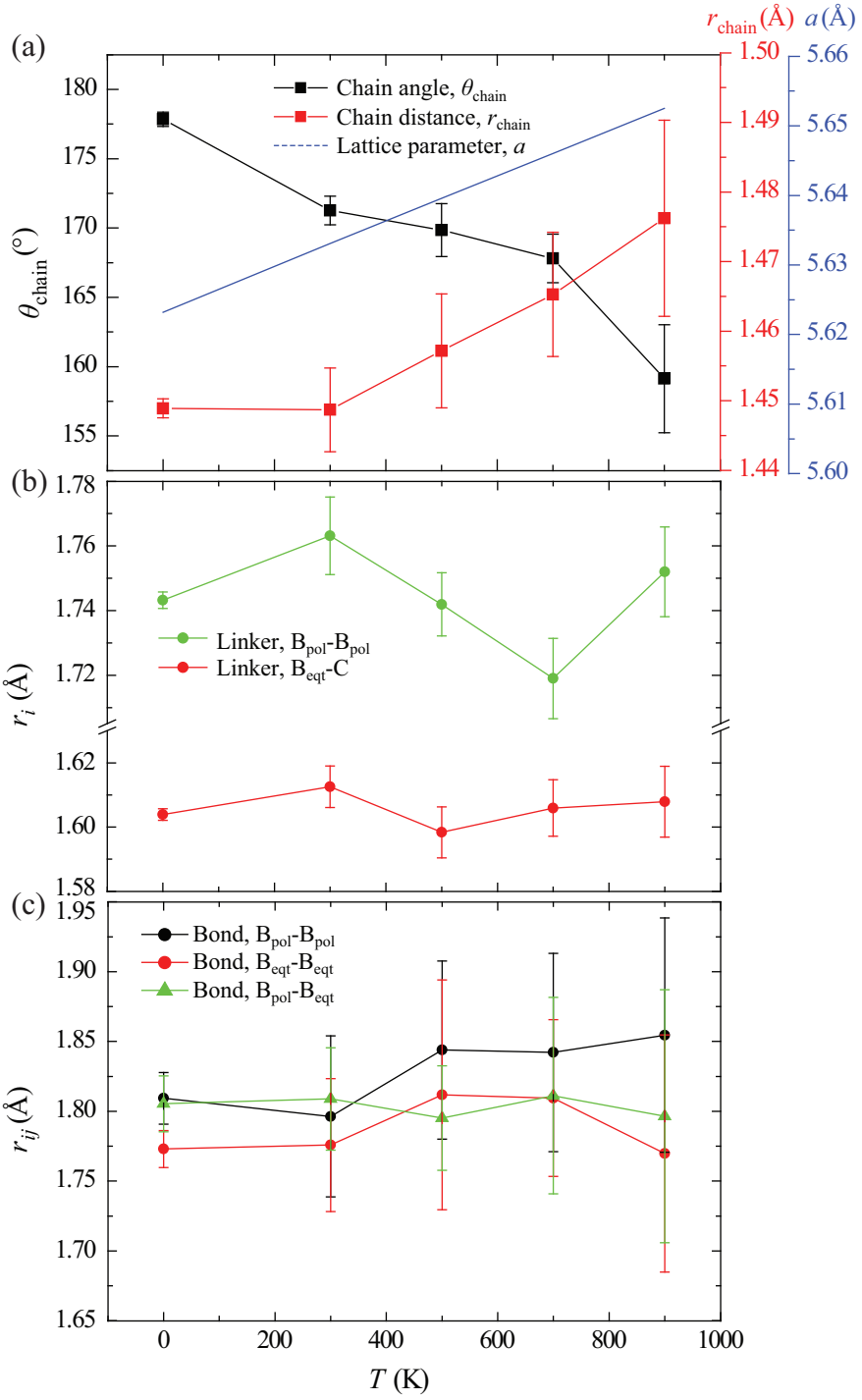

Figure 6.2: Temperature-dependent (a) bond change of inter-icosahedral C-B-C chain, (b) bond change of linker bonds, and (c) intra-icosahedral bonds. The temperature-dependent experimental lattice parameter a is also shown.

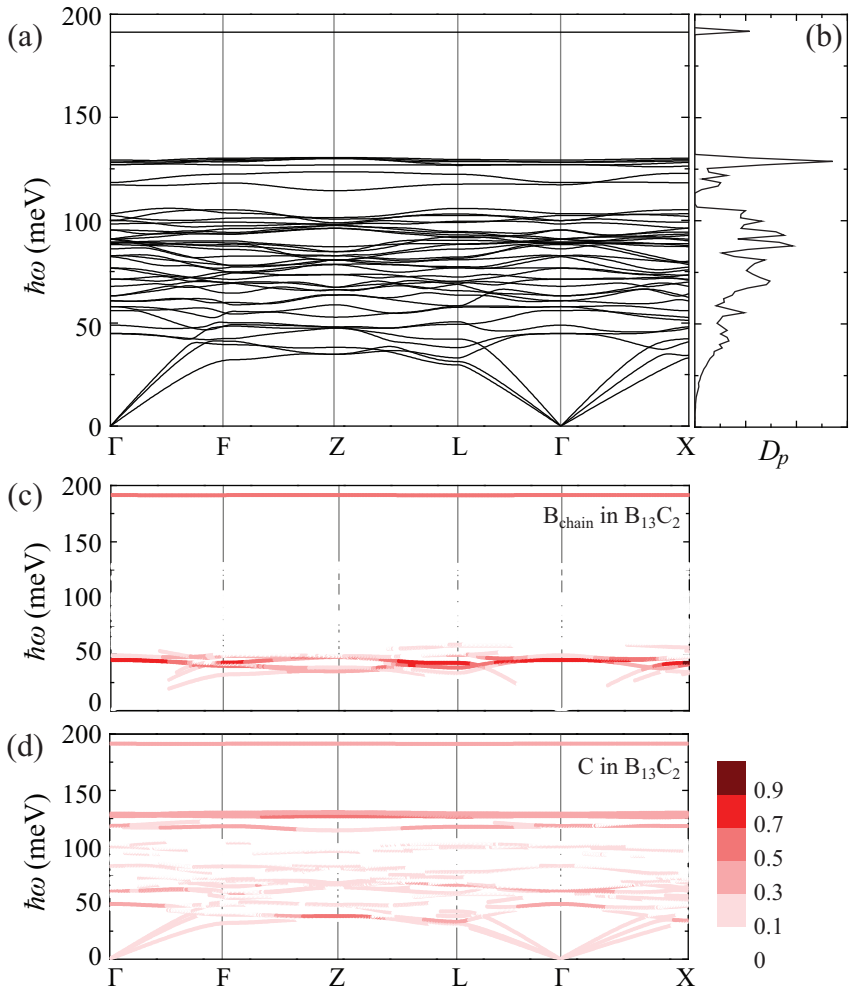

Figure 6.3: Calculated phonon characteristics of $B_{13}C_2$: Total phonon (a) dispersion curves and (b) density-of-states. Projected phonon dispersion curves of (c) B_{chain} and (d) C atoms. Color key shows the scaled contribution (maximum of one) of each atom.

shown in Figs. 6.3(c) and (d), most intra-icosahedral and polar linker bonds occupy acoustic and moderate optical parts, while the inter-icosahedral C-B-C chain bonds cover two local vibration modes [highest acoustic ($\sim$ 40) and optical ($\sim$ 190 meV)]. Despite the two-body (C-B_{chain}) bond in this chain having the shortest length (i.e. most rigid one) in $B_{13}C_2$, its three-body angle is the most flexible (due to limited neighbor atoms). Such Janus-faced C-B-C chain bond is unique in crystalline solids, and we suggest that this provides evidence of its abnormal transport properties.

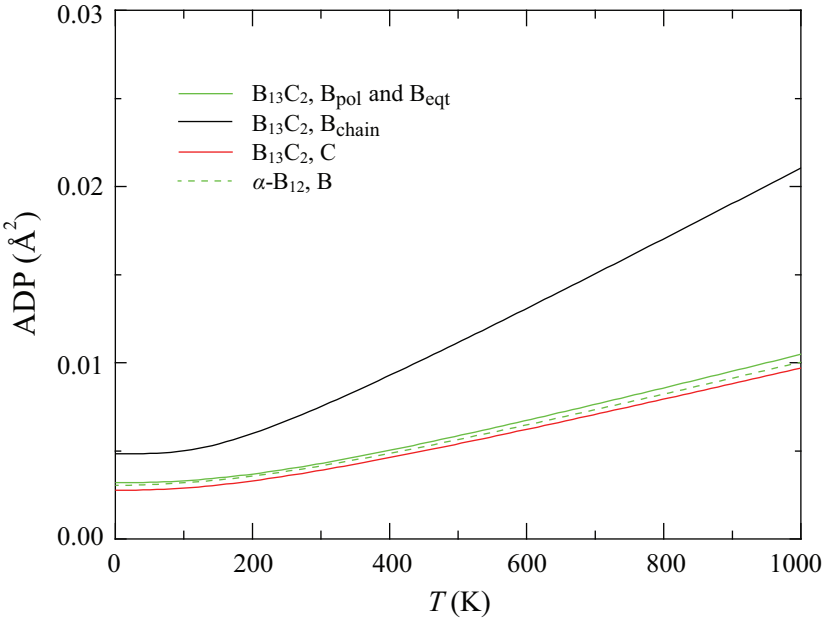

Figure 6.4: Calculated atomic displacement parameters for individual elements in $B_{13}C_2$ and α-B_{12} as a function of temperature.

Figure 6.4 shows the calculated ADP (under harmonic approximation) for each of the designated elements in $B_{13}C_2$ and α-B_{12}. Due to the strong and stable covalent bonds [181], for the overall icosahedral atoms, there is no distinct ADP difference between the two structures. However, the ADP of chain B (B_{chain}) is twice that of icosahedral B (B_{pol} and B_{eqt} in $B_{13}C_2$ and α-B_{12}). This large ADP of B_{chain}

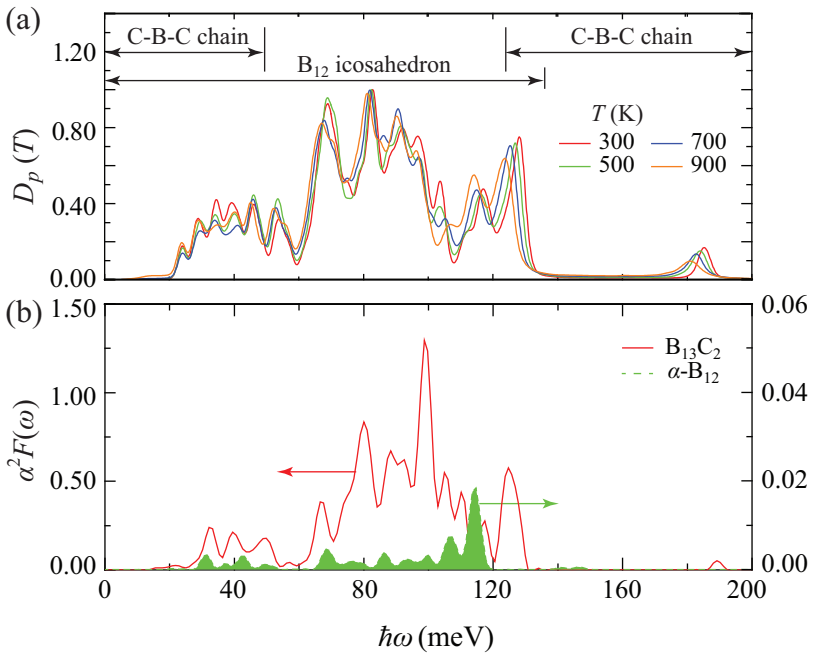

Figure 6.5: (a) Variation of total phonon density-of-states with temperature and (b) the Eliashberg function spectrum for $B_{13}C_2$.

atoms is one of distinct lattice behaviors of $B_{13}C_2$ and we expect scattering of the heat-conducting phonon wave as in rattlers [41, 139, 186]. Such phonon dispersion and atomic displacement features in $B_{13}C_2$ lattice are shown in Fig. 6.5(a). These show the phonon occupancy and roles contributed by each structural compartment of $B_{13}C_2$. Note that optical phonons of the icosahedral bonds and C-B-C chains result in the phonon softening and local vibrational frequency, respectively. In the optical frequency domain, the D_p is red-shifted as temperature increases. This phonon softening is critical in explaining the temperature independence of α_S. The B_{chain} atoms mostly lead to the local phonon mode of $\sim$ 40 meV and weak force constant, one of reasons for low κ_L of $B_{13}C_2$. This is consistent with the local phonon dispersion and large ADP of B_{chain} atoms. Next, we show that phonon softening is caused by the high-temperature Jahn-Teller distortion and polaron formation.

The e-p interaction is critical in explaining the unusual properties of $B_{13}C_2$ [36, 77, 172, 211]. The $\alpha^2F(\omega)$ spectrum characterizes the strength of the e-p coupling of the structure, and in Fig. 6.5(b). This is shown for $B_{13}C_2$ and α-B_{12} structures at low temperatures. Because $B_{13}C_2$ has high carrier density, significant e-p interactions are predicted, dominant in the icosahedral optical region, while α-B_{12} has negligible couplings. So, e-p couplings are highly related with the lattice dynamics of icosahedral structure and the trapped charge. Although the frozen structure of $B_{13}C_2$ (at T = 0 K) is an orthorhombic $R3m$ and high symmetry icosahedral complexes, we expect large geometrical distortion enhancing e-p interactions with increase in temperature, i.e., the Jahn-Teller distortion effect. The distortion and localized charge distribution of $B_{13}C_2$ result in polaron formation at high temperatures, and this causes bond softening.

Figure 6.6(a) shows the low-symmetry lattice structure and the altered effective charge of each atom, and contrasting them with the frozen (ideal) structure. At T = 0 K, the B_{12} icosahedron loses its electrons, while the inter-icosahedral C-B-C chain is negatively charged. The effective charges of B_{eqt} and B_{pol} are +0.92 and -0.01e_c, and these are highly consistent in the overall structure. However, these conditions are not sufficient for polaron formation at low temperatures. Compared to that, the Jahn-Teller distortion activated by temperature makes for unique modifications in the charge distribution, as shown in Figs. 6.6(b) and (c). Also, the polaron formation accelerates the lattice distortion (bond softening) and traps the local charge within the distorted structure. The charge density (n_e) plot shown in Fig. 6.6(b) clearly shows the existence of polaron with the localized charges and lattice distortion. Comparing

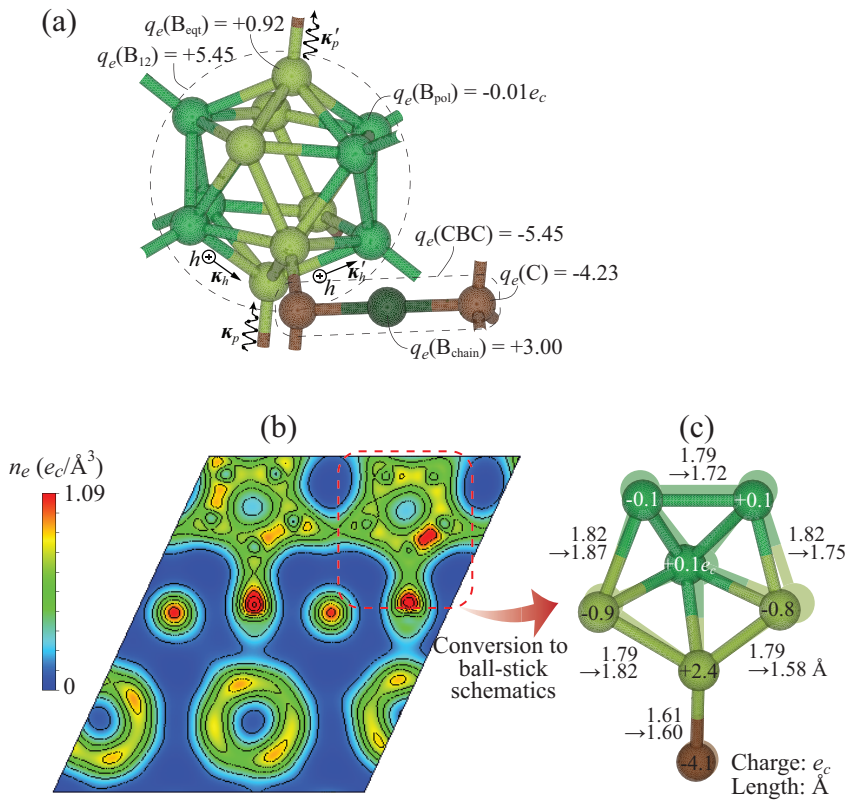

Figure 6.6: The Jahn-Teller distortion and polaron formation of $B_{13}C_2$. (a) A presentation of carrier transport and averaged effective charge distribution at $T = 0$ K. (b) Contours of constant charge density, and (c) distorted icosahedron (area surrounded by a dashed line), at $T = 900$ K (for comparison, changes of bond length and ion positions between 0 and 900 K, and effective charges at $T = 900$ K are also shown).

with high-symmetry position of ions (translucent color) shown in Fig. 6.6(c), highly-charged atoms (e.g., B_{eqt} with $+2.4e_c$) attract/repel adjacent ions depending on their polarity and accelerate the lattice distortions after producing the polarons. Using the low-temperature structure as the reference (high-symmetric lattice and the associated charge distribution), we can decipher the significant thermal lattice distortions. These are observed by comparing the intra-boron bonds of the harmonic ADP results ($\sim$ 0.1 Å at $T = 900$ K in Fig. 6.4) with the high-temperature EAIMD snapshot results [$\sim$ 0.2 Å at $T = 900$ K in Fig. 6.6(c)]. The bond length analysis in Fig. 6.2 leads to similar conclusion, i.e., significant distortions at high temperatures (large error bars

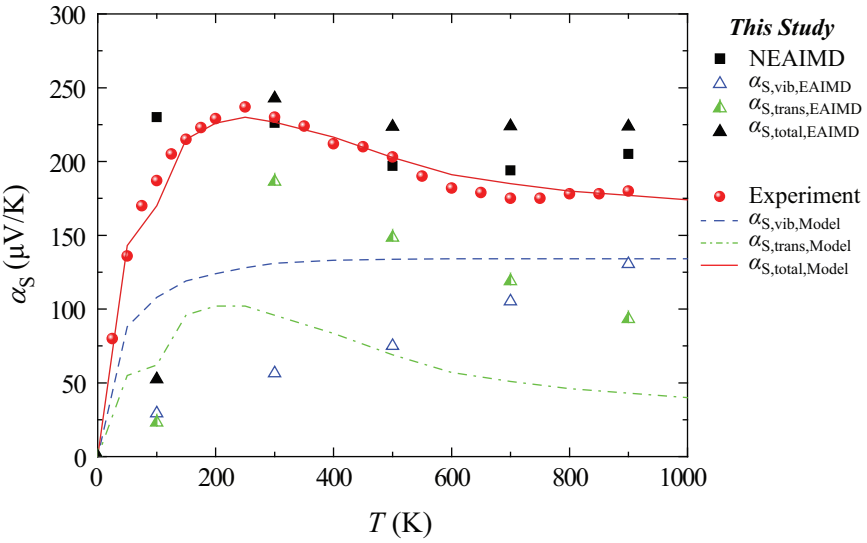

Figure 6.7: Variations of $B_{13}C_2$ Seebeck coefficient and its components as a function of temperature. NEAIMD, reported experimental results [14, 15], and analytical model [14, 15] are shown. To clarify its origins, vibration and transport components to the net Seebeck coefficient are also provided.

for the intra-icosahedral bonds compared to other bonds at $T = 900$ K). These are generally self-trapped, and cannot contribute to various transport properties at low temperatures, but several hopping mechanisms activated by temperature [15, 63, 64] are suggested. Next we show such phonon softening and polaron generation assisted by e-p interactions can affect the abnormal behaviors of α_S and κ_L in $B_{13}C_2$.

6.3.2 Prediction of Seebeck coefficient

We calculate the value of α_S for $B_{13}C_2$ using the DFT-based methods, and Fig. 6.7 results show that α_S becomes nearly independent of temperature above 600 K. Temperature-independent α_S is commonly observed in solids when high-temperature charge conduction is dominated by the hopping of constant-density small polarons [14, 15].

Here, available experimental results [15] are confirmed with the direct method and entropy analyses using DFT. Using NEAIMD shown in Fig. 6.8(a), we calculate α_{S} with this direct method, i.e., the charge difference under the applied temperature difference [see Figs. 6.8 (a) and (b)] [105],

$$\alpha_{\mathrm{S}} = -\frac{\Delta\varphi_e}{\Delta T}. \tag{6.8}$$

Here, the potential difference ($\Delta\varphi_e$) is computed as the ratio of charge difference (Δq_e) and the electric permittivity over the prescribed temperature difference (ΔT) over a distance (l), i.e.,

$$\Delta\varphi_e = \int_0^L \frac{n_e}{\epsilon_e\epsilon_\circ}\mathrm{d}x = \frac{\Delta q_e l}{\epsilon_e\epsilon_\circ A}, \tag{6.9}$$

where ϵ_e and $\epsilon_\circ$ are the relative and free-space permittivities, and A is the cross-section area of the simulation cell. For the relative permittivity of $B_{13}C_2$, the experimental results [126, 211] are used. We note that the low-temperature discontinuities in ϵ_e of $B_{13}C_2$ may be ignored because of the polarization and phase change of $B_{13}C_2$. The simulations details are given in the method section. Figure 6.8(b) shows the predicted charge distribution along the temperature gradient in the simulation cell. This snapshot shows the trapped charge and polaron generation in high-temperature icosahedra. The α_{S} obtained from Eq. (6.8) is plotted in Fig. 6.7, showing an initial sharp increase with temperature and temperature independence at high temperatures. These NEAIMD predictions agree well with the available experimental results [15].

To explain this unusual $\alpha_{\mathrm{S}}(T)$ behavior, two different contributions to α_{S} are also

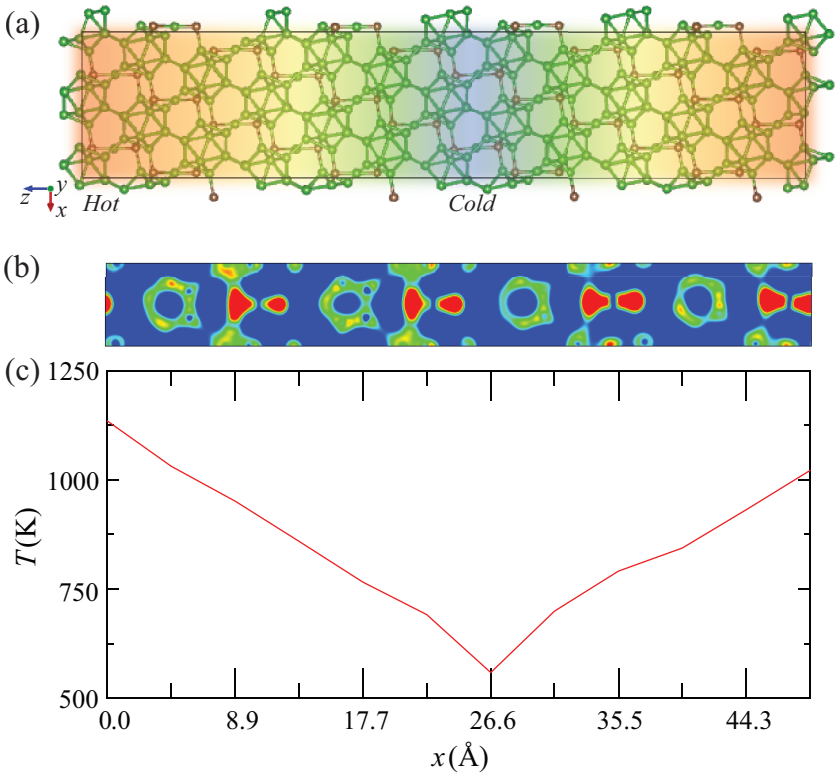

Figure 6.8: (a) A schematic of $B_{13}C_2$ structure (hexagonal, 2×1×4 supercell) used in NEAIMD simulations. Distributions of (b) charge and (c) temperature along a simulation cell.

shown in Fig. 6.7. Using the temperature-dependent D_p shown in Fig. 6.5(a) and Eq. (6.5), the high-temperature vibrational contributions to α_S are predicted. Charge carriers and their interactions cause a net energy transfer and in $B_{13}C_2$, the locally-induced polarons change the net energy transfer by employing deformation energy and hopping activation energy (E_a, $\sim$ 0.17 eV) [14, 15, 30]. The transport contributions to α_S are calculated with $\alpha_{S,trans,ep} = E_T/q_eT$ and Eq. (6.7). As shown in Fig. 6.7, the component $\alpha_{S,vib}$ increases as the temperature increases, while $\alpha_{S,trans,ep}$ rises from zero, and reaches a peak at about 1/3 of the Debye temperature (T_D, $\sim$ 750 K), and then falls to a small value. Thus, we verify that the phonon softening contributes to

α_S in $B_{13}C_2$. The sum of these two contributions is in agreement with the temperature dependence of the α_S of $B_{13}C_2$ obtained from our NEAIMD and in experiments [15]. In the low-temperature regime, we note limitations in the extrapolated structural parameters and the AIMD formalism (e.g., constant-volume calculation). Also we note that the EAIMD results [$D_p(T)$, $\alpha_{S,vib}$, and $\alpha_{S,trans}$] are more complete thus differ from the simple approximations used by Emin [14, 15]. The only two softening modes he used are 10 and 60 meV, i.e., one acoustic and one optical (albeit the lowest optical) mode. Based on our DFT predictions (see Figs. 6.3 and 6.5), more relevant modes can be selected. Our results show that such low energy (acoustic) mode are not affected by the phonon softening, so approximate models should include the higher energy phonons.

6.3.3 Prediction of lattice thermal conductivity

The lattice conductivity results of $B_{13}C_2$ are also obtained from the NEAIMD formulism as given in Eq. (2.29). Simulation details are given in the methods (Section 6.2.1). In order to consider the size limitation of NEAIMD, we check the size effect with three different simulation cells (180, 270, and 360 atoms for $B_{13}C_2$).

The κ_L of the infinite structure is determined from the linear extrapolation of their reciprocal relation (κ_L^{-1} versus l^{-1}) [190]. The final κ_L results of $B_{13}C_2$ shown in Fig. 6.9 has a plateau behavior in overall temperature range. In order to emphasize this unusual temperature-independent κ_L behavior of $B_{13}C_2$, it is contrasted with the results for α-B_{12}, i.e., the Slack behavior ($\sim T^{-1}$) [98, 105, 185]. As dis-

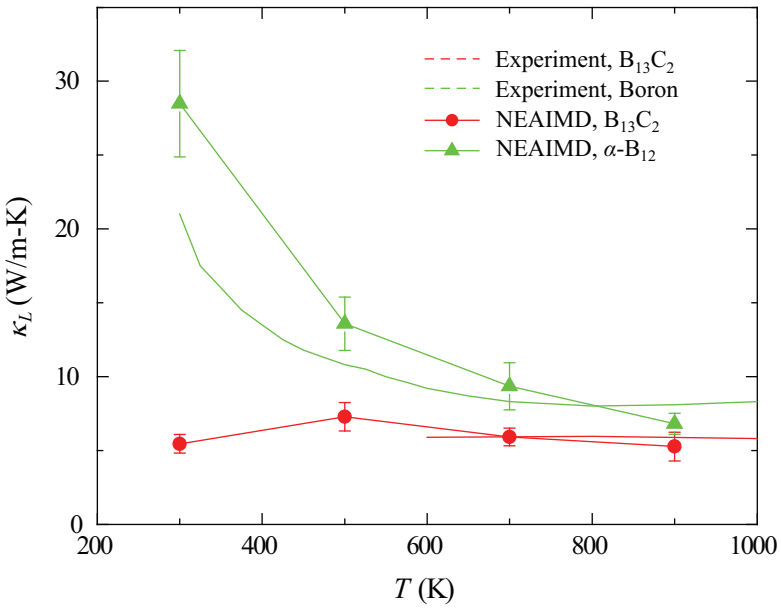

Figure 6.9: Variations of $B_{13}C_2$ and α-B_{12} lattice thermal conductivity as a function of temperature. The NEAIMD and available experimental results [187, 215] are also shown.

cussed in the lattice dynamics and charge analyses, we find two distinct features, (i) significant e-p coupling, and (ii) large ADP of the chain bond, affecting κ_L. Based on the general temperature dependence of κ_L, various phonon scattering mechanisms dominate in their respective regimes [105]. At low temperatures ($T \ll T_{\rm D}$), phonons are scattered by the grain-boundary and impurity, and by coupling with the electrons (most important here). The high temperatures ($T > 0.1T_{\rm D}$) behavior is dominated by inter-phonon scattering and follows the Slack relation for long-range acoustic phonon transport. Although $B_{13}C_2$ and α-B_{12} have almost the same icosahedral structures, the uniqueness caused by the addition of carbon into α-B_{12}, makes for the high carrier density and the C-B-C chain (inter-icosahedral) bond. Significant e-p interactions in the icosahedra suppress the κ_L at low temperatures, while the large ADP of $B_{\rm chain}$ scatters the heat-conducting phonon waves and reduces κ_L at high temperatures. In

contrast, the κ_L of α-B_{12} is large and follows the Slack relation well. This is because there are no significant phonon scattering sources (e.g., *e-p* interactions and high ADP bonds). The predicted NEAIMD results are in good agreement with the experimental results [187, 215].

6.4 Summary

Boron carbides are common high-temperature materials having anomalous properties not yet well explained. Here we showed how their polarons and phonons are affected by the interaction between lattice dynamics and charge distributions. The bond softening and *e-p* coupling caused by the high-temperature Jahn-Teller distortion and polaron formation are observed in optical phonons of icosahedra. The unique atomic displacement of the C-B-C chain bonds shows significant interphonon scattering of the acoustic modes. These theoretical and computational treatments predict abnormal temperature independencies of the Seebeck coefficient and lattice thermal conductivity, showing good agreement with experimental results. Understanding of such coupled phonon and polaron effects of $B_{13}C_2$ offers insights for new TE materials.

Chapter 7

Tuning of Electron and Phonon Behaviors in Liquid-Like Copper Selenides

7.1 Introduction

The copper selenide (Cu_2Se) has been well-known as a mixed (electronic-ionic) conductor with a significant phase transition. Above the transition temperature (T_{tr} = 413 K), it has the antifluorite FCC structure ($Fm3m$; aka β-Cu_2Se), while a monoclinic-based superstructure (α-Cu_2Se) is revealed below T_{tr} [27, 47, 93, 122, 192, 220]. Here, the antifluorite β-Cu_2Se structure is considered for the high-temperature TE applications. As shown in Fig. 7.1(a), the general crystal structure of the β-Cu_2Se consists of eight cations (Cu^+) and four anions (Se^{2-}) in its conventional cell. However, this antifluorite structures have many interstitial sites, as shown in Fig.

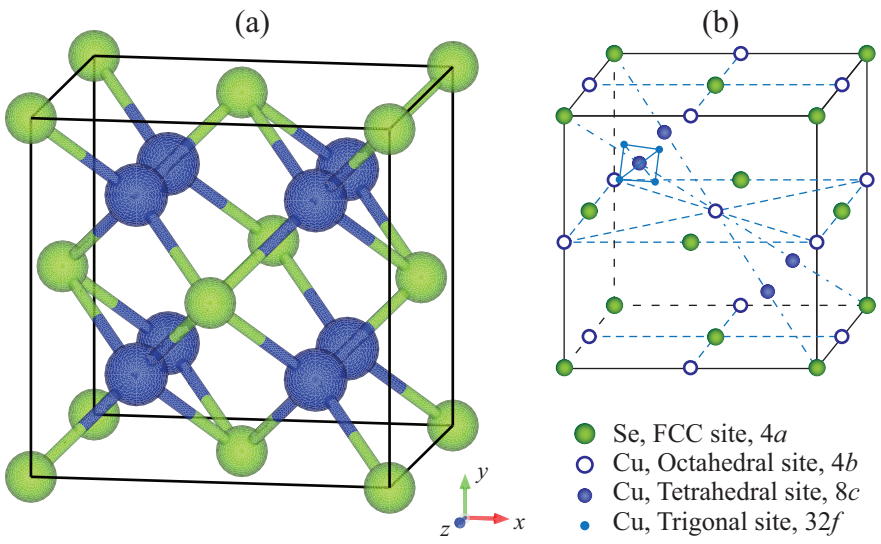

Figure 7.1: (a) The crystal structure of the β-Cu_2Se. Blue and green spheres are Cu and Se atoms. (b) Possible atomic sites for Cu^+ and Se^{2-} ions. The site designations are given in the legend.

7.2(b). The Se atoms form a rigid framework (FCC site, $4a$) in the β-Cu_2Se crystal lattice and Cu^+ ions are distributed on the different interstitial sites (octahedral, $4b$; tetrahedral, $8c$; trigonal site, $32f$) [93, 122, 150]. These close-neighbor interstitial sites allow for a significant migration of the cations (here Cu^+ ions). Recent investigations of the β-Cu_2Se have been related to applications as superionic conductor [9, 21, 47] and as TE material [122, 220] (mainly due to the significant migration of Cu^+ ions). In particular, the liquid-like properties of the β-Cu_2Se leads to a total thermal conductivity of $\kappa = 0.8$ W/m-K and show ZT of 1.5 at $T = 1000$ K [122]. However, due to lack of theoretical treatments, especially at high temperatures, fundamental understanding and predictions of the β-Cu_2Se structure and its TE properties have been lacking.

In this chapter, we present the first-principles based, comprehensive computational analyses of the electronic and phonon properties of the β-Cu_2Se and a few similar com-

pounds (e.g., β-Cu_2Te). We investigate the temperature and composition-dependent lattice dynamics and electronic properties of these structures, is search of highest ZT among them. We compare these predictions with the limited experimental results, noting the challenges in these measurements.

7.2 Calculation Methods

7.2.1 DFT calculations

We calculate the high-temperature atomic structure and the lattice dynamics using various DFT calculations implemented in the `VASP` [116] and `PHONON` [151] codes. The PBE parameterization of the GGA for the exchange-correlated functional [154] and the PAW method for modeling core electrons (energy cutoff = 355 eV) [26, 117] are used. Details are given in Sections 2.2 and 2.3. The high-temperature β-Cu_2Se structures are predicted using the EAIMD. EAIMD simulations on supercells consisting of 96 (2×2×2 conventional cells) atoms. Considering the thermal expansion, we prepare supercells with the experimental thermal expansion coefficient (α = 2.3×10^{-5}/K for 300 to 773 K and α = 10.7×10^{-5}/K for 773 to 1000 K) [122] and lattice parameter (a = 5.864 Å at T = 453 K; a = 5.917 Å at T = 873 K) [122, 220]. The Brillouin zone is sampled at the gamma point. After constant-temperature simulations with the Nosé thermostat for 1 ps (0.5 fs time steps) reaching equilibrium, we collect atomic trajectories for 22 ps (1 fs time steps).

7.2.2 Transport properties calculations

The electronic properties are calculated with the full-potential linearized augmented plane-wave method [183] as implemented in the `WIEN2k` code [25]. We calculate all TE transport properties of high-temperature β-Cu_2Se using `WIEN2k` and `BoltzTraP` [127] codes, and a NEAIMD code. All the β-Cu_2Se transport properties are calculated from the DFT band energies. They are obtained from thermally-disordered structure (EAIMD snapshots at each temperature) and the Fermi-Dirac smearing factors are also used in the transport-property calculations. The muffin-tin radii are chosen to be 2.5 a.u. for all atoms. The plane-wave cutoff $Rk_{\max} = 7.0$ suffices for good convergence. Convergence of the self-consistent calculation cycle is performed using 36 (for high temperature) k-points inside the reduced Brillouin zone to within 0.0001 Ry with a cut-off equal to -6.0 Ry between the valence and the core states. Since TE transport properties are sensitive to the band structures near the Fermi surface, we use the modified Becke-Johnson exchange potential in combination with the LDA-correlation to avoid the underestimation of the bandgap energy (a well-known problem with the DFT method) [19, 199]. For the transport calculations, the original k-mesh is interpolated onto a mesh five times as dense and the eigenenergies are found with `BoltzTraP` code. Within the Boltzmann transport theory, the temperature- and doping concentration-dependent conductivity $\sigma_e(T, \mu_e)$ and Seebeck coefficient $\alpha_{\mathrm{S}}(T, \mu_e)$ are found in Section 2.5.1 [see Eqs. (2.23), (2.24), (2.25), and (2.26)].

The NEAIMD simulations are employed for the prediction of lattice thermal con-

ductivity (κ_L). For non-equilibrium simulations, we use the `VASP` code modified to perform NEAIMD-energy exchange [103, 142] as reported in [190, 207]. As given in Eq. (2.29), the heat flux is imposed by dividing the simulation cell into sections of equal width, and exchanging kinetic energy (velocity swapping) between the hot and cold sections. Details are given in Section 2.5.2. NEAIMD simulations are performed on (hexagonal representation) supercells consisting of 192 (conventional 4×2×2 supercell), 288 (6×2×3 supercell), and 384 (8×2×2 supercell) atoms. Structure preparations are same as those for the EAIMD simulations. We carry out constant-temperature simulations using a Nosé thermostat for 1 ps (0.5 fs time steps). After reaching equilibrium, a non-equilibrium calculation is performed for 22 ps (1 fs time steps).

7.3 Results and Discussion

7.3.1 Lattice dynamics

Using the lattice dynamics analyses based on the first-principles calculations, the unique vibrational behavior of the β-Cu_2Se (e.g., the distinct temperature-dependent phonon softening due to the large interstitial displacement of the Cu atoms) are investigated. Figures 7.2(a) to (c) shows the temperature-dependent atomic trajectories of the β-Cu_2Se atoms obtained from the EAIMD simulations. The Cu atoms are highly displaced and disordered, while the Se atoms nearly remain in a rigid framework. This is quantified with the normalized directional changes of atomic density

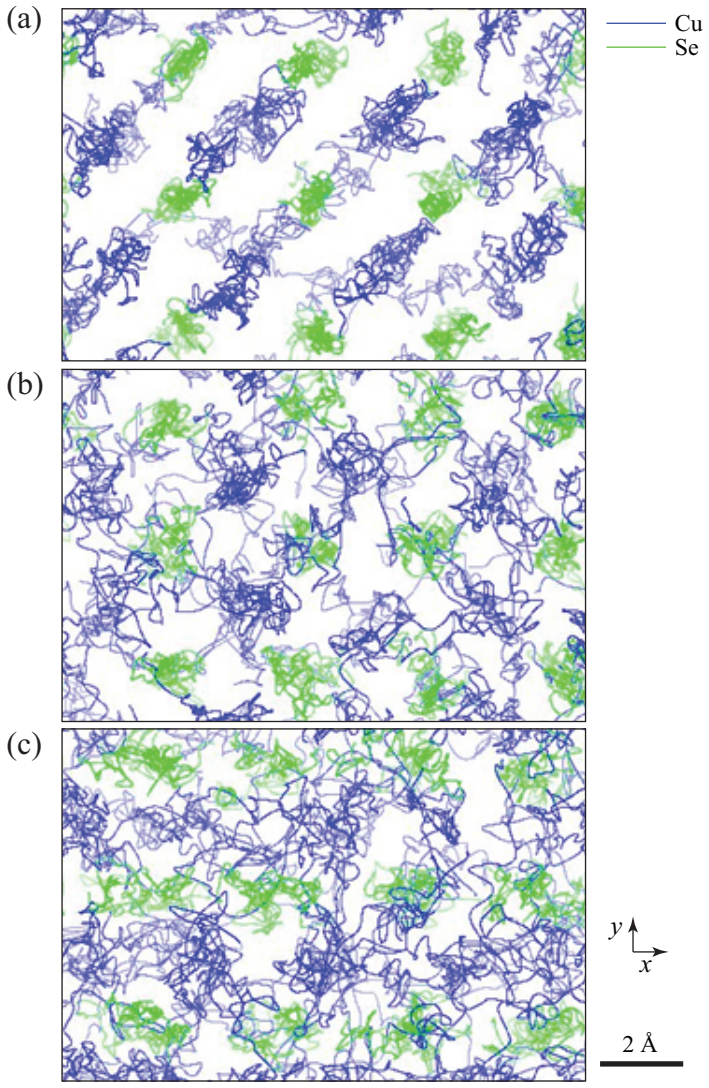

Figure 7.2: The EAIMD trajectories of the β-Cu_2Se structures for 5 ps. Blue is for Cu and green is for Se. (a) $T = 500$, (b) 700, and (c) 900 K.

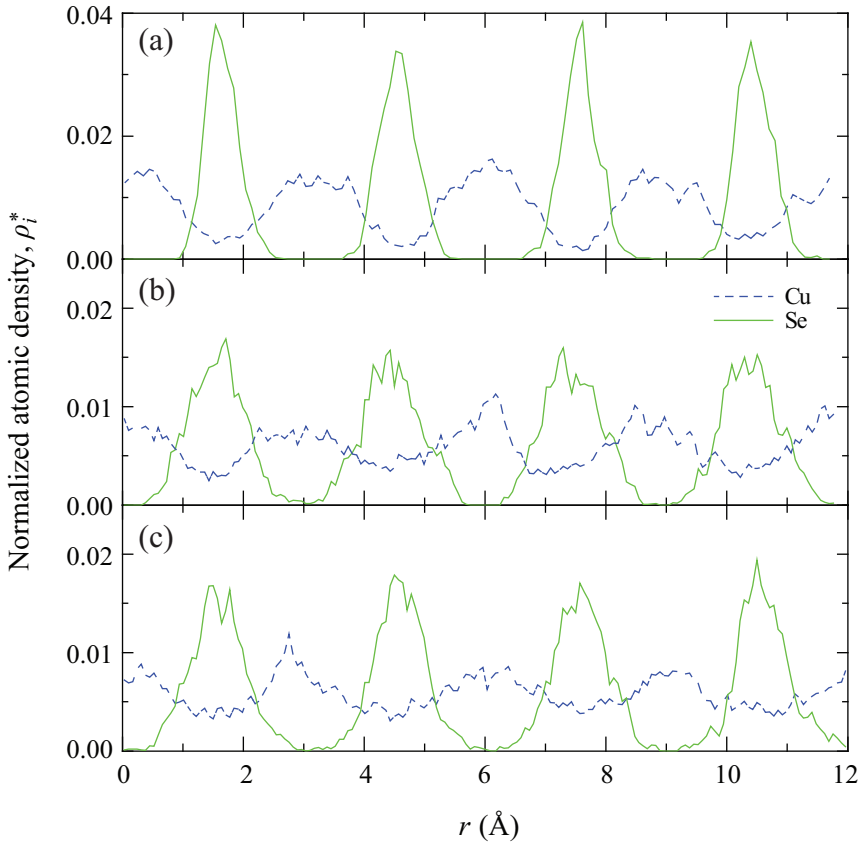

Figure 7.3: The normalized atomic density distribution of the β-Cu_2Se structures for 10 ps. (a) $T = 500$, (b) 700, and (c) 900 K.

distribution for each element. In Figs. 7.3(b) and (c), the dimensionless atomic density distributions for the structure at $T = 700$ and 900 K are compared with the results at $T = 500$ K in Fig. 7.3(a). The low-temperature structure of the β-Cu_2Se is not populated around the borders of the Se FCC and the Cu tetrahedral sites, indicating no significant movement (i.e., migration between neighboring 8c sites) of both elements at $T = 500$ K. For the Cu atoms, the nearest interstitial sites are accessed (occupied), and its density distribution is then broadened. This results from the energy-preferable high occupancies of FCC (for Se) and 8c (for Cu) sites and the sufficiently large barrier energy to prohibit the Cu migration. As temperature

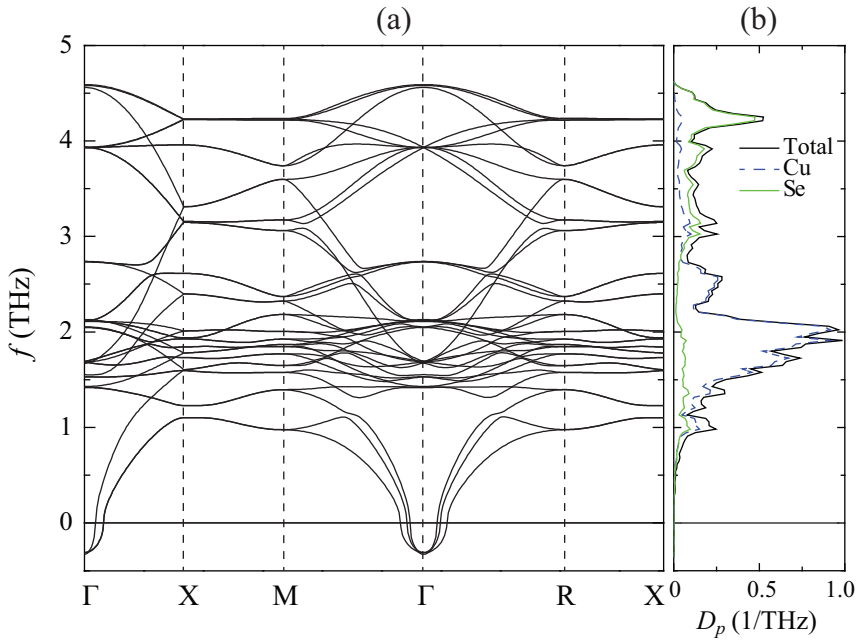

Figure 7.4: Calculated (a) total phonon dispersion curves, and (b) density-of-states of the β-Cu_2Se. The projected phonon density-of-states are also shown with the appropriate colors.

increases, different displacements of these ions are observed. The density distribution of Cu atoms becomes significantly scattered and migration among site occurs, but for the Se atoms this is much limited. It is the existence of the multiple interstitial sites (e.g., $32f$ trigonal) allows for such displacement and migration of the Cu^+ ions.

Figures 7.4(a) and (b) show the calculated phonon dispersion, and the (total and projected) density-of-states (D_p) for the β-Cu_2Se. As expected, the heavy Se atoms mostly occupy the high-phonon energy portion of the spectrum ($>$ 3 THz), while the Cu atoms cover the others. For the acoustic phonons (dominant heat carriers), the contributions from the Cu and Se atoms are nearly equal, but the roles of Cu ions are rather notable. The Cu atoms cause a flattened dispersion around 1 THz, in all directions and this suppress the acoustic phonon propagation of the Se atom, a similar role of the guest-atom vibration in the filled skutterudites [20, 41, 53, 115].

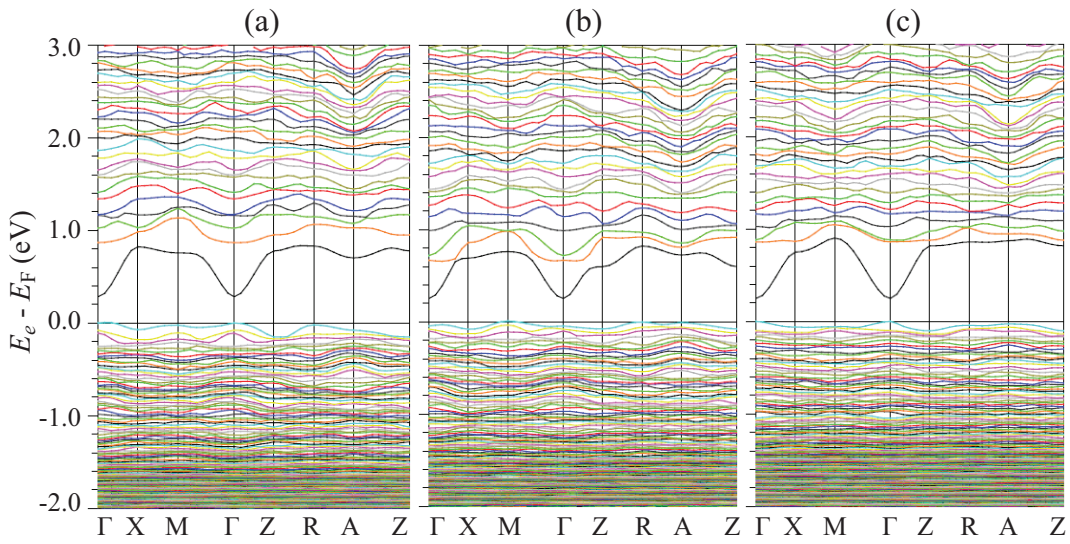

Figure 7.5: Temperature-dependent electronic band structures of the β-Cu_2Se. (a) T = 500, (b) 700, and (c) 900 K.

This observation is consistent with the general vibration understanding (i.e., the rigid Se framework and the mobile Cu^+ ions) and suggest more (i.e., heat conduction and local vibrational roles of the Cu^+ ions) about the origin of the low lattice thermal conductivity of the β-Cu_2Se.

7.3.2 Electronic transport properties

The temperature-dependent electronic band structures of the β-Cu_2Se are shown in Figs. 7.5(a) to (c). The calculated band structures of the thermally-disordered β-Cu_2Se supercell provide more reliable electronic states at high temperature (above 450 K). As expected, the available results of the bandgap energy of the β-Cu_2Se are limited ($\sim$ 1.25 eV at T = 300 K [188]), due to the many experimental challenges. Here, we have verified that the bandgap energy of the β-Cu_2Se is approximately 0.30 eV at T = 500 K and decreases as temperature increases ($\sim$ 0.25 eV at T = 900 K).

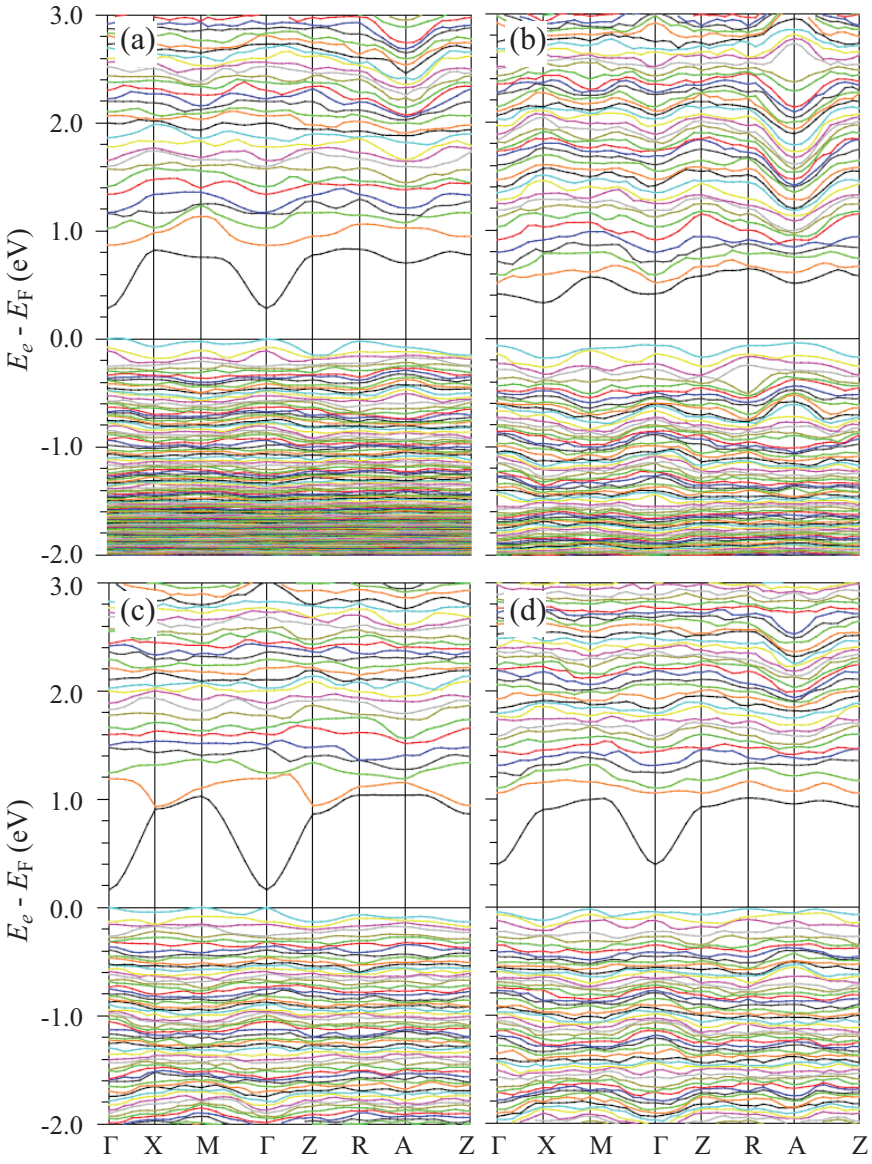

Figure 7.6: Electronic band structure of four antifluorite chalcogenides at $T = 500$ K. (a) Cu_2Se, (b) Cu_2Te, (c) Ag_2Se, and (d) Ag_2Te.

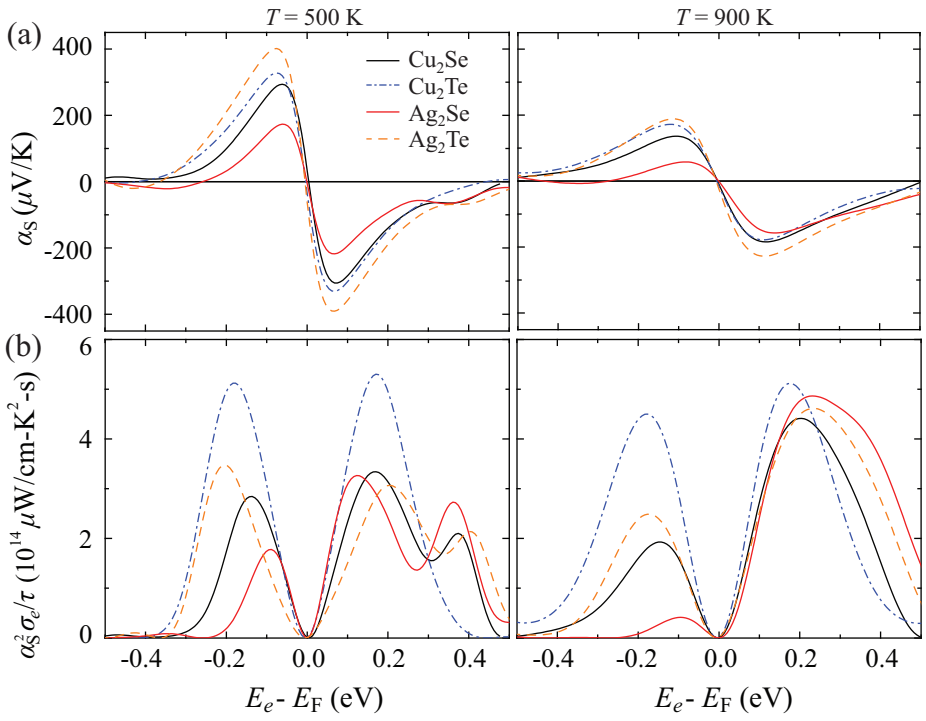

Figure 7.7: Variations of the predicted electronic TE properties, as a function of the Fermi energy, for the four antifluorite chalcogenides, and at two temperatures. (a) The Seebeck coefficient, and (b) power factor.

The alloyed compounds are one of the most promising tuning strategies for achieving higher ZT (compared to the pristine structures). To explore these possible alloy compounds of the β-Cu_2Se, we examine the electronic band structures of a few antifluorite chalcogenides (M_2X for M = Ag, Cu and X = Se, Te) and the results are shown in Figs. 7.6(a) to (d). The same β-Cu_2Se is used. Note that the bandgap energy decreases (increases) when alloying with Ag (Se) instead of Cu (Te). Also note that significant changes in the band structure are found in the β-Cu_2Te, while the other compounds show only change in the bandgap energy (0.18 eV for β-Ag_2Se and 0.40 eV for β-Ag_2Te). For the β-Cu_2Te, its band structure shows enhancement in the X- and A-direction conduction valleys. This makes the bandgap energy of the β-Cu_2Te an indirect 0.35 eV, with the possibility for high electron degeneracy. Such features in the electronic states of the β-Cu_2Te are very promising for achieving high ZT, similar to the band-convergence effects of the PbTe [109, 153]).

Using the Boltzmann transport equations under the relaxation time approximation, the electronic TE transport properties of the β-Cu_2Se and a few others (e.g., β-Cu_2Te) are calculated. The calculated transport properties at two different temperatures (T = 500 and 900 K) are shown in Figs. 7.7(a) to (d), as a function of electron energy level. The trends in the composition dependence of the TE properties are correlated with their band structure behaviors. Within the feasible doping range ($\pm$0.17 eV up to 10^{20} cm^{-3}), the Seebeck coefficients of the β-Cu_2Te and β-Ag_2Te compounds are larger than that of β-Cu_2Te, because of the enlarged bandgap and increased electron degeneracy. Note that the power factor (divided by the relaxation time) of the β-Cu_2Te is the largest among the compounds considered. We suggest

the alloy compounds of β-Cu_2Te and β-Cu_2Se are promising for superior ZT, since they have comparable electronic transport properties but expected additional phonon scattering (e.g., due to mass fluctuation).

7.3.3 Lattice thermal conductivity

For the phonon transport of the β-Cu_2Se, its lattice thermal conductivity is obtained from the NEAIMD method as expressed in Eq. (2.29). Simulation details were given in the methods (Section 7.2.1). Considering the size limitation of NEAIMD, we check the size effect with three different simulation cells (192, 288, and 384 atoms for the β-Cu_2Se).

The calculated results for the lattice thermal conductivity of the β-Cu_2Se are shown in Figs. 7.8(a) and (b). Figure 7.8(a) shows the supercell-size (l) dependence of the calculated lattice thermal conductivity values, and their extrapolation to very large l, for several temperatures. This extrapolation is common, and reliable practice as reported in [190]. Figure 7.8(b) also shows variations of the lattice thermal conductivity with temperature and this is a rather abnormal temperature dependence, over the temperature range ($\kappa_L = aT^b$, where a = 12.8 and b = -0.38). While the bulk, homogeneous materials dominated by the interphonon scattering with expect the T^{-1} dependency [98, 105, 185]. This behavior is not readily explained by the conventional phonon scattering mechanisms, so designating the phonon-scattering mechanism of the β-Cu_2Se is challenging. In order to analyze this weak temperature-dependent lattice thermal conductivity behavior of the β-Cu_2Se, we can recall its lattice dynam-

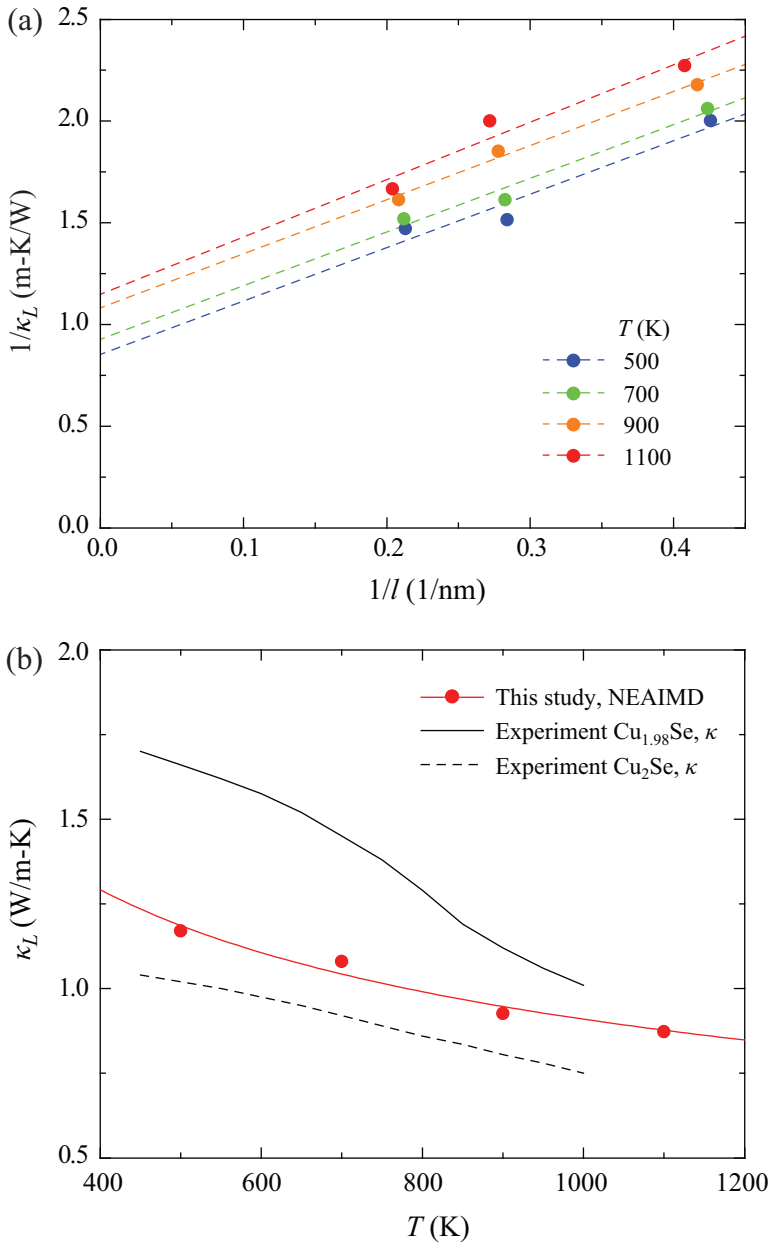

Figure 7.8: Lattice thermal conductivity results from the NEAIMD simulations. (a) Variations of the inverse of the lattice thermal conductivity with respect to the inverse of the supercell size, for three different temperatures. (b) The predicted variations of the lattice thermal conductivity with respect to temperature, and comparison with the available experimental results [122].

ics results discussed in Section 7.3.1. There we found two distinct features: (i) the distinct phonon softening due to the large interstitial displacement of the Cu^+ ions, and (ii) the limited displacement and a framework role of the Se^{2-} ions, both affecting lattice thermal conductivity. Over the temperature ranges, most acoustic phonons are highly scattered by the interphonon scattering. So, this unique weak temperature independence is caused by the large interstitial displacement of the Cu^+ ions. In addition, the weak temperature dependence can be explained the effect of rigid Se framework. Conclusively, these two different effects are combined, and it allows for the weak temperature dependence in the lattice thermal conductivity of the β-Cu_2Se.

In Fig. 7.8(b), the available experimental results are also shown and we note the difference between the NEAIMD and the experimental results [122, 220]. These can be due to the temperature-dependent instabilities arising from the significant atomic migrations between adjacent NEAIMD simulation sections. It can also be due to the problems related to atomic diffusion in the experiments (e.g., sample degradation such as change in the Cu composition). We also note that the simple application of the Wiedemann-Franz law with a constant (metallic) Lorenz number, can result in the deduced lattice thermal conductivities which are unrealistic.

7.4 Summary

In summary, we investigate the temperature-dependent electronic and phonon properties of the β-Cu_2Se and similar compounds, using the first principles. The large interstitial displacement of Cu^+ ions dominates the scattering of heat-carrying phonon

propagation observed in a rather rigid Se framework, resulting in high ZT with the significant suppression of lattice thermal conductivity. Exploring alloy compounds [e.g., β-Cu_2(Se,Te)], we note that further suppression of lattice thermal conductivity and higher ZT can be expected, since the electronic TE transport properties are not deteriorated.

Chapter 8

Summary and Future Work

8.1 Contributions

This study investigates tuning of the TE materials atomic structure and their thermal evolution for high ZT, using the first-principles based atomistic simulations. The significance of this work is the introduction and prediction of the temperature and constituent-dependent atomic motions and their roles in the phonon and charge carriers TE energy conversion. This work is based on unified and integrated computational methods (from prediction of the ground-state structure to prediction of the TE transport properties). Through these techniques, we examine tuning the TE transport properties by choosing/modifying the related independent and coupled structural variables. The electronic metrics of high ZT are the intrinsic or extrinsic control of the atomic displacement to affect the power factor and electronic thermal conductivity. Through the structural metrics for these atomic displacements we also show their dominant roles in the reduction of the lattice thermal conductivity.

Several example structures (e.g., lead tellurides, skutterudites, boron carbides, and copper selenides) are used to investigate the roles of the atomic thermal displacement in achieving high ZT.

The significant contributions of this work are summarized below.

- *Analyses on the roles of thermal disorder in lead tellurides* With the EAIMD simulations, we observe thermal disorder and find band convergence with increased temperature and close relation between thermal disorder and TE properties of p-doped PbTe. Lack of short-range order causes local overlap of valence orbitals and increase in density-of-states near the Fermi level. Effective mass becomes temperature-dependent peaking in the converged-band regime. With ECMD and the Green-Kubo autocorrelation decay we find reduction in lattice thermal conductivity (suppression of short- and long-range acoustic phonon transports). The described thermal-disorder roles lead to high ZT, and good agreement with the experimental results [109].

- *Investigation on order-disorder transition of filled skutterudites.* Filled skutterudites are high-performance TE materials and we show how their lattice thermal conductivity is greatly influenced by the topology of the filler species. We predict the *ab-initio* phase diagram of $Ba_xCo_4Sb_{12}$ and find several stable configurations of Ba ordering over the intrinsic voids. The lattice thermal conductivity predicted using ECMD shows a minimum in the two-phase mixture regime, dominated by significantly reduced long-range acoustic phonon transport [111].

- *Analyses on cage-breathing lattice dynamics of substituted skutterudites.* Based on DFT calculations, the substituted Ge atoms form the softest bonds in the compound acting as a pseudo-rattler with distinct mode-flattening features and a local phonon softener (comparable to rattlers in filled skutterudites). The collective modes of this lattice configuration induce the breathing mode in the cage which is highly correlated with the reduction in lattice thermal conductivity. The lattice thermal conductivity predicted with NEAIMD simulations is in good agreement with the experimental results and the point-defect scattering model. We suggest that this new scattering mechanism can be combined with the conventional rattling mechanism, thus causing further reduction in κ_L in these hybrid structures [41].

- *Understanding and prediction of the coupled polaron and phonon effects of boron carbides.* The anomalous temperature-independent behavior of the Seebeck coefficient and the lattice thermal conductivity of $B_{13}C_2$ are explained through polaron and phonon evolutions found using EAIMD. Analyses of lattice dynamics show that the unique icosahedron structures dominate the optical phonon modes and C-B-C intericosahedral bonds dominate the local acoustic vibration. We identify that the temperature-induced Jahn-Teller distortion and electron-phonon coupling in icosahedron structures create small polarons (i.e., charge trapping and phonon softening). We also verify that large-displacement chain atoms scatter heat-conducting phonons. Using EAIMD and NEAIMD methods (including entropy and energy analyses), we predict the Seebeck coefficient

and its components as well as the lattice thermal conductivity, and we find good agreement with experiments. Softened and localized phonons make a significant vibrational contribution to the Seebeck coefficient and allow for an amorphous-like lattice thermal conductivity [110].

- *Tuning of electron and phonon behaviors in liquid-like copper selenides.* Using the first principles, we analyze the phonon and electronic properties of the β-Cu_2Se and a few similar compounds (e.g., Cu_2Te). The temperature-dependent lattice dynamics shows large interstitial displacement of the Cu^+ ions and a rather rigid Se framework. These results in significant suppression of the lattice thermal conductivity and weak temperature dependence, $\sim T^{-0.3}$. We examine the roles of cations and anions such as Cu (or Ag) and Se (or Te) in the electronic TE properties. Then we suggest that the alloys of β-Cu_2Te and β-Cu_2Se are promising high ZT materials, since they have comparable electronic transport properties but reduced lattice thermal conductivity due to additional alloy phonon scattering.

8.2 Proposed Future Work

Three possible extensions of this work are suggested below.

- Predictions employing direct DFT simulations should be extended to all TE transport properties to complement the current BTE-RTA predictions. To accurately model and predict the electronic TE transport properties, we still use this classic model. However, we know this method is derived based on many as-

sumptions and require empirically-based properties. In this study, we suggested and used the direct *ab-initio* predictions of the lattice thermal conductivity and the Seebeck coefficient. Additional comprehensive DFT methodologies covering electrical conductivity and electronic thermal conductivity are should be developed.

- Extend to treatment of the phonon and charge carrier transport for the non-periodic materials (e.g., organic or low-dimensional structures). These have been receiving increased attention due to much anticipated potentials for tuning as compared to the bulk materials. However, due to current limitations of the *ab-initio* treatments, fundamental understanding and predictions of their structure and TE properties are lacking. This study mainly focuses on the prediction and tuning of the periodic materials in TE application. To complete this challenge, further studies should consider the van der Waals force influencing transport among neighboring structures and the important statistical approximations for the non-periodic structures.

- Experimental investigations should be carried out on the proposed high-ZT structures to verify the predicted scattering mechanisms and transport properties. Recent major theoretical advances now make possible multiple time and length-scale simulations and prediction, and allow for exploring promising new TE structures. In the future, we need to verify these new understandings and predictions via the extensive experimental investigations.

8.3 Outlook

This atomic-level treatment can be extended to meso-scale transport phenomena to include the effect of nanostructures (bulk, non-homogeneous materials). Such future progress is essential for exploring, understanding and designing new superior ZT materials.

Appendix A

Entropy Analysis of Seebeck Coefficient

A.1 Introduction

The Seebeck effect is the formation of electric potential in presence of spatial variation of temperature. In 1821, Seebeck observed that a temperature difference between two ends of a metal bar created an electrical current in between, with the voltage (difference in electric potential $\varphi_{e,i}$) being directly proportional to the temperature difference [45]. Physically, when one side of a conductor is hot, electrons have higher thermal energy and will diffuse to the cold side. The charge (carrier) concentration rise on the cold side builds an internal electric field that resists the diffusion. The Seebeck voltage is the steady-state potential difference under open-circuit condition. Here,

$$-(\varphi_{e,2} - \varphi_{e,1}) = \alpha_{\mathrm{S}}(T_2 - T_1), \tag{A.1}$$

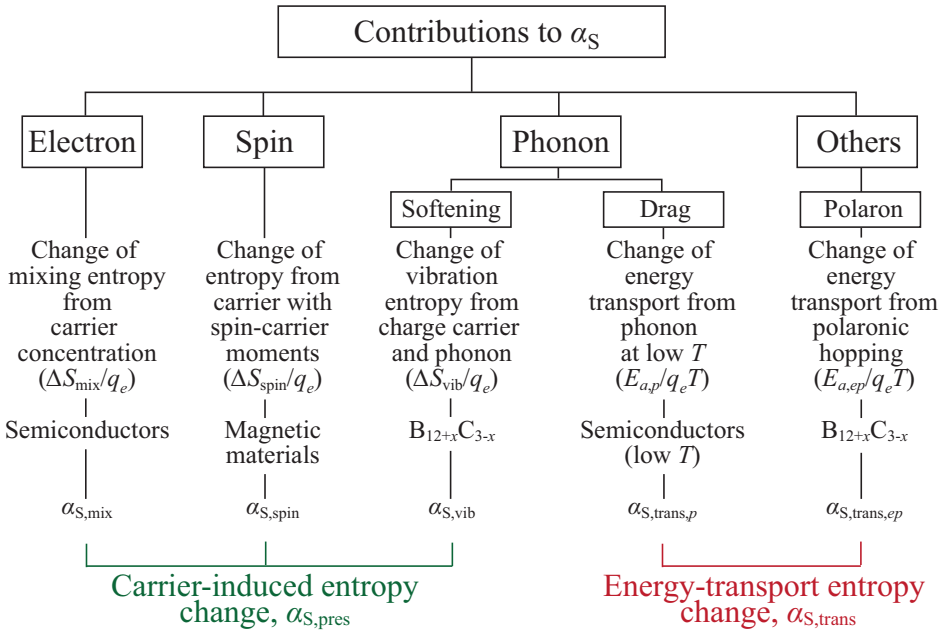

Figure A.1: Various contributions to the Seebeck coefficient with respect to different carriers. Their physical interpretation and example of materials for each category are also shown.

where α_S is the Seebeck coefficient and T_i is the temperature of site i.

A.2 Derivation

As shown in Fig. A.1, various carriers contribute to the Seebeck coefficient. Also, their interactions with electrons, magnons, phonons, and other charge carriers (e.g., polarons) substantially affect the Seebeck coefficient. Figures A.2(a) to (d) show the atomistic schematics for those contributions. The overall Seebeck coefficient can be expressed as the sum of two contributions [63, 64, 65, 141],

$$\alpha_S = \alpha_{S,pres} + \alpha_{S,trans}, \tag{A.2}$$

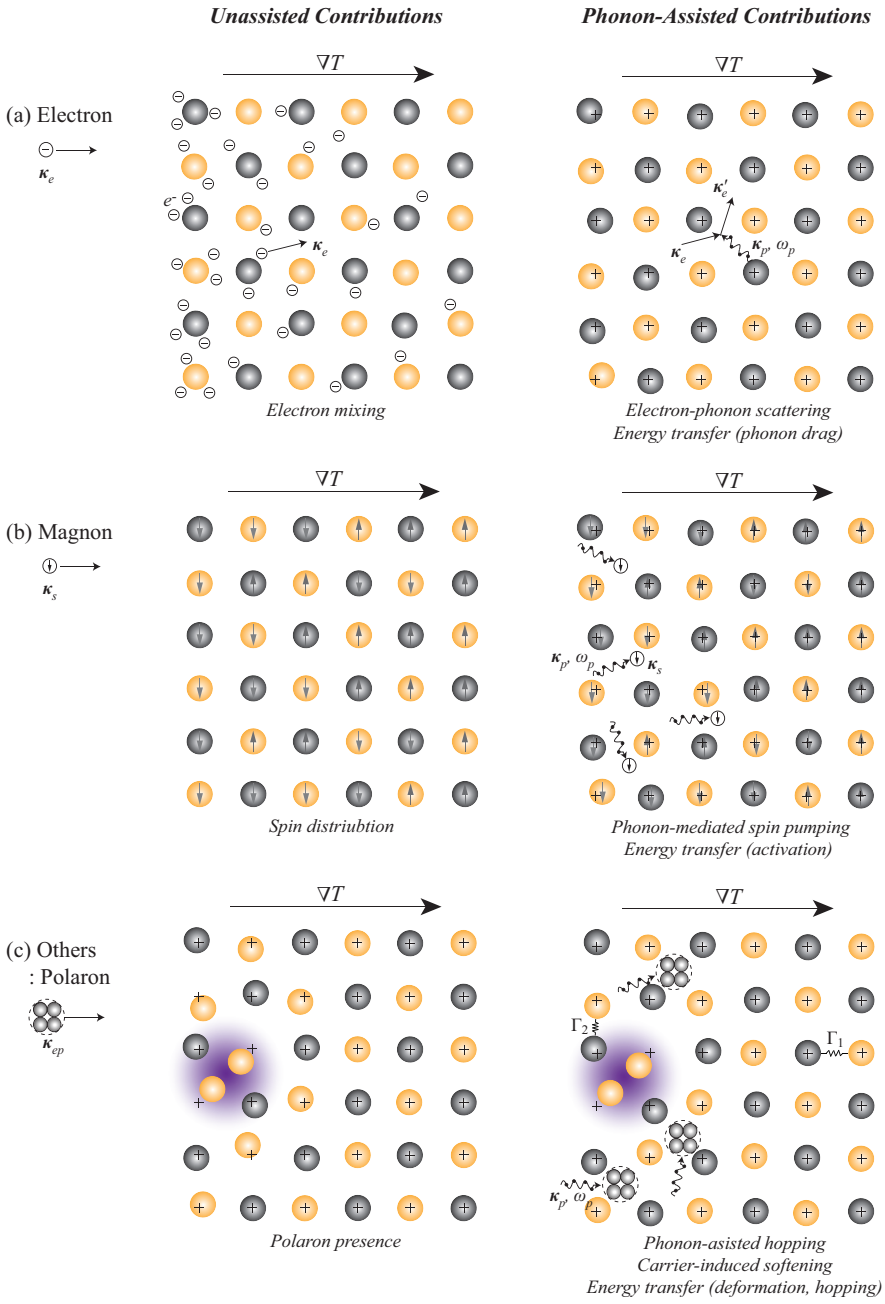

Figure A.2: Atomistic metrics of the Seebeck coefficient contributions in crystals. Model for the temperature-driven entropy change by (a) electron mixing and (b) thermal disorder, and (c) spin entropy and (d) polaron induced phonon-softening.

where $\alpha_{\mathrm{S,pres}}$ is the sum of contributions to the carrier-induced entropy change, i.e.,

$$\alpha_{\mathrm{S,pres}} = \alpha_{\mathrm{S,mix}} + \alpha_{\mathrm{S,spin}} + \alpha_{\mathrm{S,vib}}, \tag{A.3}$$

where the right-hand side terms are change of the entropy-of-mixing, spin entropy, and vibrational entropy upon adding a charge carrier, respectively. The other contribution $\alpha_{\mathrm{S,trans}}$ is the net energy transferred in moving a carrier divided by $q_e T$, where q_e is the carrier charge [63].

Each carrier mostly contributes to the Seebeck coefficient in different way and specific conditions, however they are highly coupled and interacting with phonon. In phononic point of view, most prominent contributions to the Seebeck coefficient can be summarized as electron-phonon coupling [65, 73], phonon drag [65, 168], phonon-mediated spin pumping [200], phonon-assisted carrier hopping [64, 65, 213], and carrier-induced phonon softening [64, 65, 141]. Although those effects have been examined in several experimental results [64, 65, 73, 141, 168, 200, 213], no overall coupling consideration or DFT-based calculation of phonon contributions to the Seebeck coefficient have been reported yet. The analyses and tuning of its phonon contribution is considered as one of promising strategies to achieve the high Seebeck coefficient.

A.2.1 Mixing component

The entropy-of-mixing contribution is usually dominant in lightly-doped semiconductors. The change of the entropy-of-mixing upon adding a carrier to a system is

large because there are very few carriers per thermally available state [64, 90]. Figure A.2(a) shows the electron mixing with a certain temperature gradient. The system is described as spinless fermions (here, electron) on atomic sites. As given in [105], the calculated degeneracy for this system is given by $W = N_a!/N!(N_a - N)!$, where N is the number of electrons and N_a is the number of atomic sites per unit cell. The entropy is given by $S = k_{\mathrm{B}}\ln(W) = k_{\mathrm{B}}N\ln(Z) + E/T$. Using the Stirling's approximation, and differentiating with N, we have,

$$\alpha_{\mathrm{S,mix}} = \frac{k_{\mathrm{B}}}{q_e}\ln(\frac{1 - f_e^{\circ}}{f_e^{\circ}}), \tag{A.4}$$

the so-called Heikes formula. Here $f_e^{\circ} = N/N_a$ is the ratio of electrons to sites (carrier concentration). An alternative form of this simple expression is obtained when the ratio is expressed in terms of the energy of the electronic energy band, the chemical potential (μ) and the thermal energy ($k_{\mathrm{B}}T$) via the Fermi function, $f_e^{\circ} = 1/\{\exp[(E_e - \mu)/k_{\mathrm{B}}T] + 1\}$, i.e.,

$$\alpha_{\mathrm{S,mix}} = -\frac{k_{\mathrm{B}}}{q_e}(\frac{E_e - \mu}{k_{\mathrm{B}}T}). \tag{A.5}$$

In high-temperature regime, the electronic energy level shifts with temperature, and the Seebeck coefficient become change. Figure A.2(b) show the thermal disorder effect caused by a solid's thermal expansion and the electron-phonon interaction.

A.2.2 Spin component

As given in Eq. (A.1), the common Seebeck effect refers to the generation of an electric potential $\Delta\varphi$ by placing a non-magnetic material in a temperature gradient ΔT. Extending the Seebeck effect to spins, a ferromagnetic alloy [200] can be an example. Two spin channels would introduce different TE voltages and consequently a spin voltage would be generated, $\Delta\varphi\uparrow$ - $\Delta\varphi\downarrow$ = ($\alpha_{\mathrm{S,spin}}\uparrow$ - $\alpha_{\mathrm{S,spin}}\downarrow$)$\Delta T$. The contribution to the Seebeck coefficient that results from carriers' presence altering the systems spin entropy also becomes simple in absence of intersite magnetic interactions [see Fig. A.2(b)]. Then the spin contribution for a carrier confined to a single magnetic site is

$$\alpha_{\mathrm{S,spin}} = \frac{\Delta S_{\mathrm{spin}}}{q_e} = \frac{k_{\mathrm{B}}}{q_e}\ln(\frac{2s+1}{2s_\circ+1}), \tag{A.6}$$

where $s_\circ$ and s are the net spins of the magnetic site in the absence and presence of the carrier, respectively [64].

A.2.3 Vibration component

As shown in Fig. A.2, many vibrational contributions to the Seebeck coefficient are existed. The softening of the vibrational frequencies produces a change of the vibrational entropy is one of examples. Figure A.2(c) show the polaron induced phonon softening and the augmentation of vibrational component of the Seebeck coefficient. The full crystal Hamiltonian for the vibrational part of the energy is obtained by adding the potential and kinetic energy. As shown in [105], we write the

Hamiltonian (for the quantum-harmonic oscillator) as [28, 189]

$$\mathrm{H_{vib}} = \sum_{q} \hbar\omega(q)(f_p^{\circ} + \frac{1}{2}). \tag{A.7}$$

This expression gives the Hamiltonian for the vibrational part of the energy, and it can be used to solve analytically for a number of thermodynamic properties. The free energy is [128]

$$F_{\mathrm{vib}} = -k_{\mathrm{B}}T\ln Z = -k_{\mathrm{B}}T\ln[\sum_{\mathrm{states}} \exp(-\frac{\mathrm{H_{vib}}}{k_{\mathrm{B}}T})] = k_{\mathrm{B}}T\ln[\sum_{q} \ln[2\sinh\frac{\hbar\omega(q)}{2k_{\mathrm{B}}T}]. \tag{A.8}$$

This entropy is the negative derivative of the free energy, i.e., [128]

$$\begin{aligned} S_{\mathrm{vib}} &= -\frac{\partial F_{\mathrm{vib}}}{\partial T} \\ &= 3Nk_{\mathrm{B}}T\int_0^{\omega}\{\frac{\hbar\omega}{2k_{\mathrm{B}}T}\coth(\frac{\hbar\omega}{2k_{\mathrm{B}}T}) - \ln[2\sinh(\frac{\hbar\omega}{2k_{\mathrm{B}}T})]\}D_p(\omega)d\omega, \end{aligned} \tag{A.9}$$

where $D_p(\omega)$ is the phonon density-of-states for the structure. As shown in [105], the phonon density-of-states give the number of modes with frequency lying in the interval $[\omega, \omega + \mathrm{d}\omega]$. From the high-temperature limit ($k_{\mathrm{B}}T \gg \hbar\omega$) and series expansions of the hyperbolic functions, the above reduces to

$$\begin{aligned} S_{\mathrm{vib}} &= -3Nk_{\mathrm{B}}\int_0^{\infty}[(\frac{\hbar\omega}{2k_{\mathrm{B}}T})(\frac{2k_{\mathrm{B}}T}{\hbar\omega}) - \ln(\frac{\hbar\omega}{2k_{\mathrm{B}}T})]D_p(\omega)d\omega \\ &= -3Nk_{\mathrm{B}}\int_0^{\infty} D_p(\omega)\ln(\omega)d\omega + 3Nk_{\mathrm{B}}[1 + \ln(k_{\mathrm{B}}T)]. \end{aligned} \tag{A.10}$$

Equation (A.10) is given per atom,

$$S_{\mathrm{vib}}/\mathrm{atom} = -k_{\mathrm{B}} \int_0^\infty D_p(\omega) \ln(\omega) d\omega + k_{\mathrm{B}}[1 + \ln(k_{\mathrm{B}}T)]. \tag{A.11}$$

The last term is structure independent and cancels out when taking differences. Terms involving $\ln(\hbar)$ are generally left out of the above equation for convenience (they also cancel when taking differences). Hence, the vibrational contribution to the Seebeck coefficient [63, 64] is simplified in high-temperature region as

$$\alpha_{\mathrm{S,vib}} = \frac{\Delta S_{\mathrm{vib}}}{q_e} = \frac{k_{\mathrm{B}}}{q_e} \sum_i \frac{-\Delta\omega_i}{\omega_i}. \tag{A.12}$$

A.2.4 Transport component

As shown in Fig. A.1, some charge carriers and their interactions cause the change of net energy transfer. For example, locally-induced polarons change the net energy transfer by employing deformation energy and hopping activation/transfer energy [see Fig. A.2(d)]. To calculate $\alpha_{\mathrm{S,trans}}$ related with the phonon-assisted hopping, we start from $\alpha_{\mathrm{S,trans}} = E_T/q_eT$, where E_T is the net flow of the vibrational energy that accompanies a phonon-assisted hop from an initial site to a final site [61, 64], i.e.,

$$E_T = \frac{k_{\mathrm{B}}T^2}{2}[\frac{\partial \ln(\dot{\gamma}_{1,2}/\dot{\gamma}_{2,1})}{\partial T_1} - \frac{\partial \ln(\dot{\gamma}_{1,2}/\dot{\gamma}_{2,1})}{\partial T_2}]_{T_1=T_2=T}. \tag{A.13}$$

Here $\dot{\gamma}_{1,2}$ (and $\dot{\gamma}_{2,1}$) are the hopping rates from site 1 to site 2 (and from site 2 to site 1), while site 1 is at temperature T_1 and site 2 is at temperature T_2. The ratio of the

jump rate is

$$\frac{\dot{\gamma}_{1,2}}{\dot{\gamma}_{2,1}} = \frac{\int_{-\infty}^{\infty} \exp[G(1,2:t)\cos[F_2(1,2:t) + \Delta E_{12}t/\hbar]dt}{\int_{-\infty}^{\infty} \exp[G(2,1:t)\cos[F_2(2,1:t) + \Delta E_{21}t/\hbar]dt}, \tag{A.14}$$

where,

$$G(1,2:t) = \sum_q [\varphi^c_{e-p,1}\coth(\frac{\hbar\omega}{2k_{\mathrm{B}}T_1}) + \varphi_{e-p,2}\coth(\frac{\hbar\omega}{2k_{\mathrm{B}}T_2})][\cos(\omega t) - 1], \tag{A.15}$$

$$F_2(1,2:t) = \sum_q [\varphi^c_{e-p,1} + \varphi_{e-p,2}]\sin(\omega t), \tag{A.16}$$

and ΔE_{12} is the difference between final and initial site energies (including lattice-relaxation energies) for a carrier that hops from site 1 to site 2. Here the functions $\varphi_{e-p,1}(\varphi_{e-p,2})$ describe the coupling of the electronic state at site 1 (and site 2) to vibrations of frequency ω_p when unoccupied or occupied by a carrier, respectively. A simple expression for E_T is obtained when one observes that the binding energy varies inversely with the local stiffness, $E_b \sim 1/M\omega^2$, and one considers the limit of a small fractional carrier-induced frequency shift, (ω - ω_c)/ω = |-$\Delta\omega/\omega$| $\ll$ 1. So, Eq. (A.13) simplifies to [63, 64]

$$E_T = E_a \sum_i (\frac{-\Delta\omega_i}{\omega_i}) \frac{\hbar\omega_i/2k_{\mathrm{B}}T}{\sinh(\hbar\omega_i/2k_{\mathrm{B}}T)}. \tag{A.17}$$

A.3 Example: Phonon Softening and Polaron Hopping for $B_{13}C_2$

Boron carbides ($B_{12+x}C_{3-x}$) have distinctive structures and unconventional bondings. As shown in Fig. 6.1, a boron carbide unit cell (rhombohedral representation) contains an icosahedron consisting of twelve atoms, and strong covalent bonds linking icosahedra to one another. As a result, boron carbides are very stiff, hard solids with melting temperatures of $\sim$ 2600 K [13, 54, 62]. Replacing carbon by boron atoms removes bonding electrons and thereby produces hole-like charge carriers. Such non-stoichiometry results in high densities of p-type charge carriers ($\sim 10^{21}$ cm^{-3}), or about one hole per unit cell [13].

Boron carbides' extraordinary hardness and high carrier densities suggest that these solids would have large thermal conductivities and small Seebeck coefficients. Yet many boron carbides have surprisingly small thermal conductivities and large Seebeck coefficients, suggesting localized charge carriers that move with low mobility by polaronic hopping.

The Seebeck coefficients of a boron carbide sample ($x = 1$) become nearly independent of temperature above about 600 K (see Fig. 6.7). Temperature-independent Seebeck coefficients are commonly observed in solids when high-temperature conduction is dominated by the hopping of constant density small polarons [14, 15]. Those experimental results are confirmed using the DFT-based direct method, NEAIMD. From [105], the potential difference ($\Delta\varphi_e$) is computed as the ratio of charge difference (Δq_e) and the electric permittivity over the prescribed temperature difference

(ΔT) over a distance (l) [see Eq. (6.9)].

For simulations we use the `VASP` code [116] modified to perform NEAIMD-energy exchange [103, 142] as reported in [190, 207]. The simulations are performed on the supercell of 360 atoms, based on the experimental results for thermally expanded lattice parameter [198]. We equilibrate each simulation using the EAIMD for 1 ps with a 0.5 fs time steps. Equilibrium is followed by 22 ps of NEAIMD using a 1-fs time step. To clarify the charge associated with each atom along the simulation cell (hot to cold), Bader's analysis [91] on a charge density grid is used with a DFT charge density.

The Seebeck coefficient is finally obtained from Eq. (A.1). As shown in Fig. 6.7, the NEAIMD predictions of boron carbides agree with experimental results. To clarify the origin of this unusual trend of boron carbides' Seebeck coefficient, two phonon contributions to the Seebeck coefficient are also shown in Fig. 6.7. First, reducing the local vibrational frequencies (phonon softening) increases the vibrational entropy. This entropy is from the negative derivative of the thermodynamic free energy and can be simplified using the high-temperature limit ($k_{\mathrm{B}}T \gg \hbar\omega$) and series expansions of the hyperbolic functions (see Section A.2.3). Hence, the vibrational contribution to the Seebeck coefficient is given in Eq. (A.12). Also, some charge carriers and their interactions cause the change of net energy transfer. In boron carbides, locally-induced polarons change the net energy transfer by employing deformation energy and hopping activation energy (E_a). To calculate the transport Seebeck component related with the phonon-assisted hopping, we start from $\alpha_{\mathrm{S,trans},ep} = E_T/q_eT$ and Eq. (A.13). Using the binding energy relation with the local stiffness, the exact form of E_T

can be simplifies to Eq. (A.17). Using Eq. (A.17), a simple expression for the net flow of vibrational energy, the transport contribution related with phonon-assisted hopping is calculated. In the temperature-dependent phonon density-of-states obtained from EAIMD and the Fourier transform of a velocity autocorrelation function over 22 ps (with 1 fs steps), we observed the phonon softening of overall frequency domain. This contribution to the high-temperature phonon part of the Seebeck coefficient. The vibrational part ($\alpha_{\mathrm{S,vib}}$) is increasing as temperature becomes higher. The other contribution (i.e., $\alpha_{\mathrm{S,trans},ep}$) rises from zero, reaches a peak at about 1/3 of the relevant Debye temperature ($\sim$ 750 K), and then falls to a small value. Summing these two contributions is in good agreement with the temperature dependence of the boron carbide Seebeck coefficient from NEAIMD and experiment. Note that our EAIMD decomposition provides different results with the results of Emin's approximation [14, 15].

Our theoretical and computational treatment demonstrates that boron carbides have a high-temperature phonon softening and phonon-assisted polaron hopping contributing to the Seebeck coefficient. Those understanding and new predictions show this material is a good example to show phonon contributions to the Seebeck coefficient.

Appendix B

Thermal Conductivity of Uranium Dioxides

B.1 Introduction

Uranium dioxide (UO_2) is a stable fluorite structure (CaF_2 type, space group $Fm3m$) containing 4 U^{4+} and 8 O^{2-} ions in a conventional cell (Fig. B.1). This crystalline solid is one of the most common nuclear fission fuel materials with high melting temperature ($T_m \sim 3120$ K), radiation stability, and chemical compatibility but has low thermal conductivity (κ) and fuel density impose. The low thermal conductivity directly influences the thermal stability (e.g., local heating and swelling of the fuel pellet) and the operating temperature [71, 165], so accurate thermal conductivity data and possible improvements are important.

To explain the heat conduction mechanisms in UO_2, various theoretical [51, 85, 175], computational [10, 16, 217, 218], and experimental [4, 7, 12, 17, 46, 79, 82, 94,

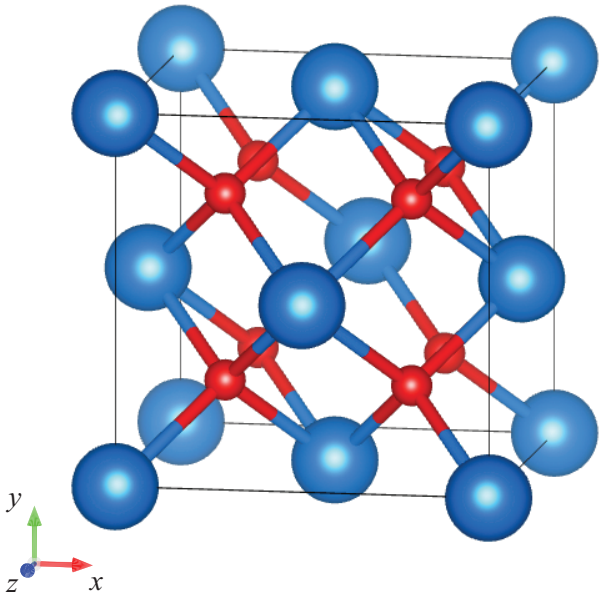

Figure B.1: Crystal structure of pristine UO_2 using the conventional cell (blue is U and red is O).

125, 136, 138, 155, 164, 209, 218] studies have been performed in the last five decades. These include the effects of the crystalline structure [4, 138, 155, 164, 209, 218], non-stoichiometry [82, 175], porosity [12, 125], and irradiation [7, 136]. These show large grain and stoichiometric composition are favorable for heat conduction, while the defects (e.g., pores remaining after sintering, and radiation-caused voids, impurities, and fission products) hinder the transport of heat carriers. Also, it has been suggested [4, 71, 85, 138, 164, 175] that charge carriers play a significant role in high-temperature heat conduction. However, so far due to the absence of first-principles based results, the fundamental understanding of the UO_2 thermal conductivity mechanisms (including the role of charged heat carriers) has been lacking.

In the large-bandgap energy crystalline materials, phonon is considered as the dominant heat-conducting carrier [105]. The heat conduction of UO_2 is dominated by phonon transport up to moderate temperatures ($T < 1500$ K). This phonon be-

havior (and lattice dynamics) is clearly explained by recent atomic-level simulations based on the DFT, including prediction of its significant anharmonicity [219] and mechanical/thermodynamic/vibrational properties [80, 221]. In the high-temperature regime ($T > 1500$ K), many reports have shown that the thermal conductivity of UO_2 is dominated by the charged-carrier transport [4, 71, 85, 105, 138, 164, 175]. Despite the semiconductor feature of UO_2 crystal (bandgap energy $\Delta E_{e,g} \sim 2.0$ eV) [18, 51, 55, 204], the classic band theory is inadequate in describing its electrical properties [11, 18, 51, 71, 84, 85, 86, 144, 167]. To explain the high-temperature behavior of its thermal conductivity, the small-polaron hopping mechanism has been suggested [11, 18, 38, 71, 84, 85, 166, 167]. This polaron model is evolving and has not been yet been verified with first-principles based analysis.

Here, we present a comprehensive analysis of the thermal conductivity of UO_2 crystals employing the DFT (including equilibrium/non-equilibrium molecular dynamics simulations) and analytic methods. We predict the temperature-dependent lattice thermal conductivity (κ_L) of UO_2 and compare our DFT predictions with the available experimental results and the prediction of the ECMD results. The effects of porosity and grain boundary scatterings are modeled with the effective lattice thermal conductivity. The charged carriers (polaron and electron) heat conduction is examined through probing the charge distribution in search of small polarons in the bulk and adjacent to the surface of UO_2 crystal. We combine these to predict the total thermal conductivity and compare with available experimental results for sintered-powder UO_2.

B.2 Calculation Methods

B.2.1 Electronic properties and lattice dynamics

We calculate the electronic structures and the lattice dynamics of UO_2 using the DFT method implemented in the `VASP` [116] and the `PHONON` code [151], respectively. The PBE parameterization of the GGA for the exchange-correlated functional [154] and the projector augmented wave method for modeling the core electrons (energy cutoff = 400 eV) [26, 117] are used. Details are given in Section 2.2. Since the standard DFT calculations fail to simulate the strong correlations among uranium $5f$ electrons as reported in many studies [40, 55, 56, 58, 59, 114, 221], we use one of the alternatives, the GGA+U method, to predict the exact electronic and phonon behaviors of UO_2. We apply the same value for the effective Hubbard parameter (U = 4.5 eV and J = 0.51 eV) used in the literatures [40, 56, 58, 59, 114]. The calculated total and projected electronic density-of-states (D_e) and bandgap energy ($\Delta E_{e,g}$ = 1.8 eV) are shown in Fig. B.2. We have reproduced the previous results [40, 56, 58, 59, 114] and verified the suitability the GGA+U method.

All phonon and mechanical and thermodynamic properties are predicted using fits of the interatomic force-constant tensors to the HF forces. Details are given in Section 2.3. For the high-temperature electronic structure and the lattice dynamics, the EAIMD is employed. The EAIMD simulations are performed on supercells consisting of 180 (bulk) and 90 (surface) atoms. To consider the thermal expansion, we prepare supercells with the experimental thermal expansion coefficient and lattice parameter, i.e., $a(T) = a_\circ(9.9734\times10^{-1} + 9.802\times10^{-6}T - 2.705\times10^{-10}T^2 + 4.391\times10^{-13}T^3)$ and

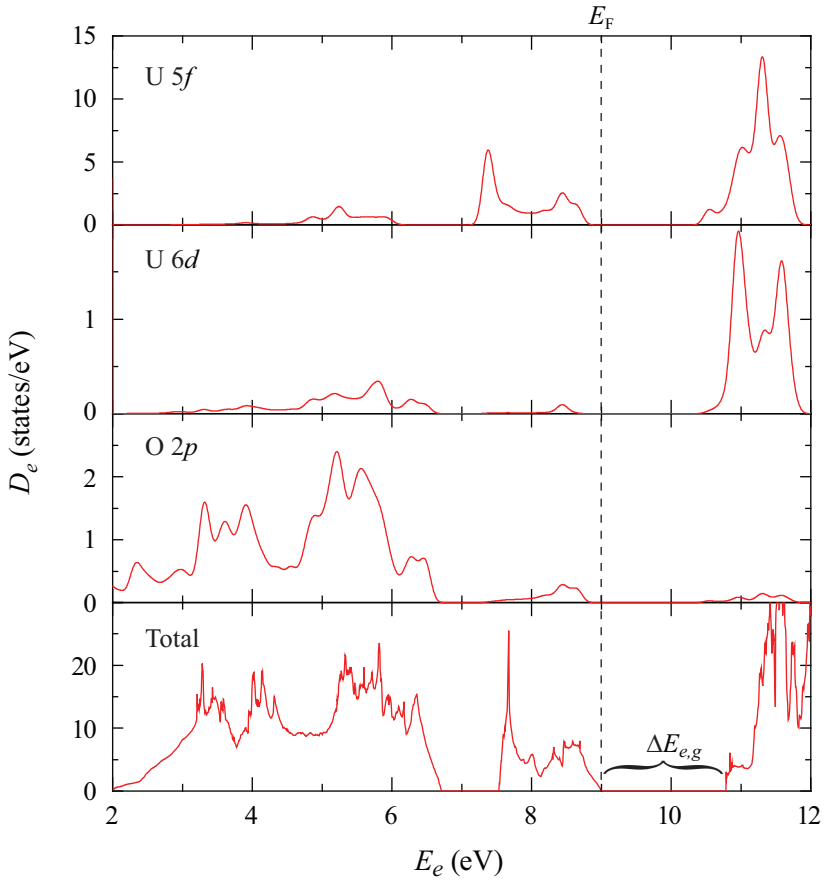

Figure B.2: Calculated projected (U 5f-6d and O 2p) and total electronic density-of-states of pristine UO_2. The Fermi level and bandgap energy are also shown.

$a_\circ = 5.455$ Å at $T = 300$ K [130]. The Brillouin zone is sampled at the Γ point. After constant-temperature simulations with the Nosé thermostat for 1 ps (0.5 fs time steps) reaching equilibrium, we collect atomic trajectories for 22 ps (1 fs time steps).

B.2.2 Thermal conductivity

To predict the lattice thermal conductivity, we use the NEAIMD with the modified `VASP` code based on the energy exchange method [103, 142] as reported in [190, 207]. As given in Eq. (2.29), the heat flux is imposed by dividing the simulation cell into sections of equal width, and exchanging kinetic energy (velocity swapping) between the hot and cold sections. Details are given in Section 2.5.2. Because the exchange of kinetic energy results in non-Newtonian dynamics in the hot and cold sections, only the linear portion of the temperature gradient is considered in calculating the temperature gradient. For further validation on the charge associated with each atom in the simulation cell (hot to cold), the Bader analysis [91] of charge-density grid is used with the DFT charge density. Using the cubic UO_2 conventional cell, 4×2×2 (total 192 atoms), 6×2×2 (total 288 atoms), and 8×2×2 (total 384 atoms) are prepared as the supercells of NEAIMD simulations. The structure preparations are same with those for the EAIMD simulations. As with EAIMD, the constant-temperature simulations are carried for 1 ps (0.5 fs time steps) and after reaching equilibrium, non-equilibrium calculations are performed for 22 ps (1 fs time steps).

In order to examine the NEAIMD results and clarify the validity of the available

empirical potential models, the lattice thermal conductivity is calculated using the ECMD results and the Green-Kubo HCACF decay [99, 105, 111, 133, 134]. The HCACF decay equation and heat current vector are given as Eqs. (2.27) and (2.28). Details are given in Section 2.5.2. After checking the size effect of ECMD simulations, averages are obtained over all three directions for a system consisting of 6×6×6 conventional unit cells (2592 atoms). The Verlet leapfrog algorithm with the Nosé-Hoover thermostat and the Berendsen barostat are used in the NpT ensemble for 200 ps and then in the NVE for 100 ps to reach equilibrium. Then 3000 ps raw data are obtained for the calculation of $\boldsymbol{q}$ and the resultant HCACFs are then directly integrated and the lattice thermal conductivity is set as the average value in the stable regime of the integral.

B.2.3 Surface structure

To analyze the pores as they are present in common, sintered-powder UO_2 samples, and their effects on the thermal conductivity, we use the well-established slab models. Three models with simple termination of (100), (110), and (111) surfaces and consisting of 90 atoms, are used. The slabs were defined with vacuum gaps of about 10 Å to minimize the interactions between the slab faces [160]. As reported in literatures [184, 195], the (111) surface consistently exhibits the lowest surface energy, followed by the (110) surface, and finally the (100) surface having the highest energy.

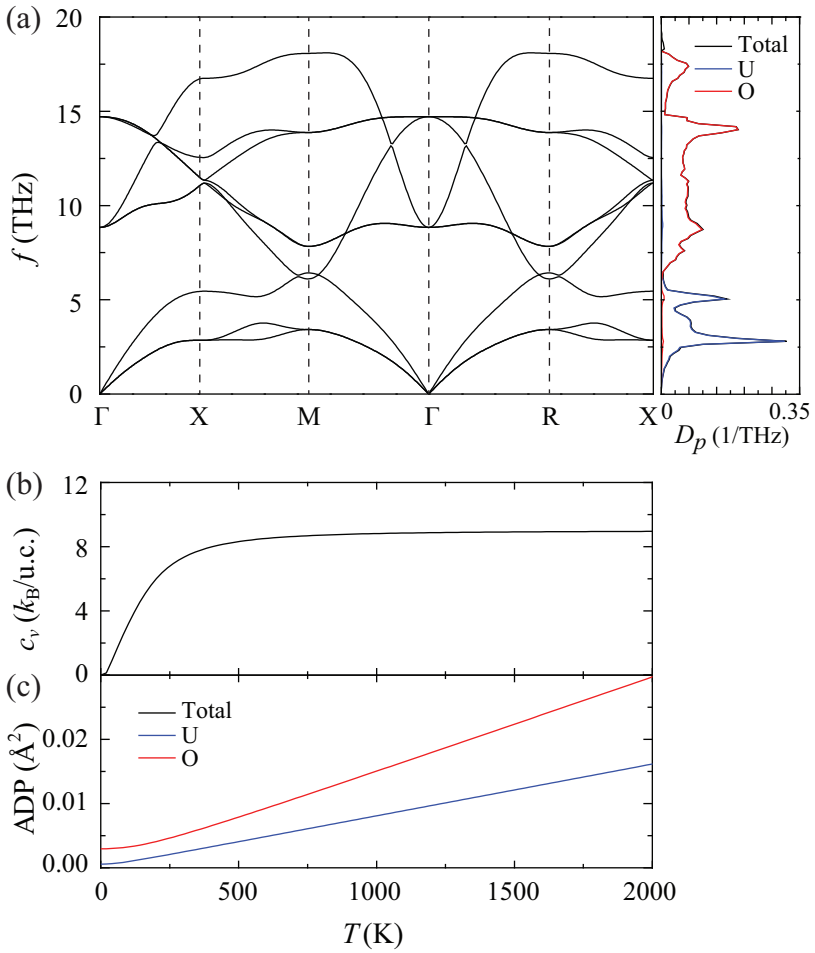

Figure B.3: (a) Calculated total phonon dispersion curves (9 modes) and total and partial density-of-states of UO_2. Temperature-dependent (b) specific heat capacity per unit primitive cell, and (c) atomic displacement parameters of UO_2.

B.3 Results and Discussion

B.3.1 Lattice dynamics and thermodynamics properties

To understand the phonon behavior of UO_2, we begin with the lattice dynamics using various DFT. Figures B.3(a) and (b) show the phonon dispersion, density-of-states (D_p), heat capacity (c_v), and ADP using small displacement method in the harmonic approximation. As we expected, heavy uranium atoms occupy the low-phonon energy portion of the spectrum (< 6 THz), while oxygen atoms cover the other. In Fig. B.3(b), the temperature-dependent heat capacity (per unit cell) is obtained from the phonon density-of-states. The asymptotic value of $c_v = 9k_{\mathrm{B}}$, the classical-harmonic Dulong-Petit limit for solids, is shown and reached for $T > T_{\mathrm{D}}$, where k_{B} is the Boltzmann constant and T_{D} is the Debye temperature, T_{D} for UO_2 = 377 K [212] and 383 K [74]. Note the quantum and anharmonicity effects at low and high temperatures, respectively. Figure B.3(c) shows the ADP results for each element. The ADP of O atoms is twice that of U. This large ADP of O is in part caused by the presence of many interstitial sites in the fluorite structure. The displacement has limited role in heat conduction, not enough to suppress the lattice thermal conductivity as Cu atoms in the β-Cu_2Se [122], or Ge atoms in $Co(Sb,Ge,Te)_3$ [41].

The time- and temperature-dependent evolutions of the U and O atoms are investigated with the RDF. Figure B.4 compares the RDF of the bulk-pristine and the pore-surface obtained from the atomic trajectories of EAIMD simulations. The known RDF thermal evolutions of the bulk structure are predictable, i.e., the peak

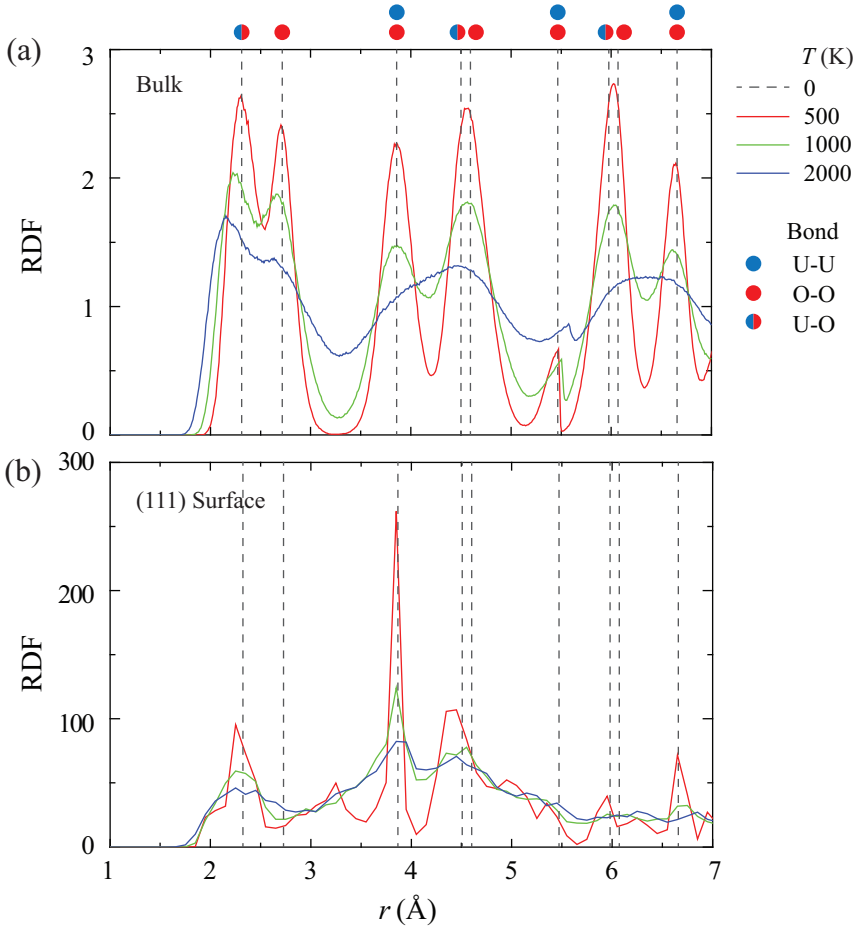

Figure B.4: Variations of the radial distribution function for the (a) bulk, pristine, and (b) (111) on the surface of UO_2, at four temperatures and for three bonds.

broadening and the non-Gaussian asymmetric feature with rising temperature (due to its well-known anharmonicity). However, the RDFs of surface atoms in the slab model are abnormal, i.e., position and intensity of peaks are different, over the temperature range. As shown in Fig. B.4(b), the surface O-O and U-O bonds are significantly softened (or shifted) while U-U bonds are strengthened. This is due to the relaxed surface structure, with distorted atomic positions and interactions, since the surface atoms have different coordination number and neighboring atoms. We expect these structural distortions to lead to surface polaron formation (charge analysis is discussed in Section B.3.3).

B.3.2 Lattice thermal conductivity

As described in the methods (Sections 2.5.2 and B.2.2), the NEAIMD-predicted lattice thermal conductivity is computed as the ratio of an applied heat flux to the resulting temperature gradient. Using three different simulations cell sizes, as shown in Fig. B.5, we verify the expected size effect and extrapolate the lattice thermal conductivity for the infinite structure, from the linear extrapolation of their reciprocal relation. Figure B.6(a) shows the temperature dependence of this predicted lattice thermal conductivity for the bulk, pristine UO_2, and compares with the available experimental results [17] and the analytical Slack relation ($\sim T^{-1}$) [98, 105, 185],

$$\kappa_{L,\mathrm{S}}(T) = \frac{3.1 \times 10^4 \langle M \rangle V_\circ^{1/3} T_{\mathrm{D},\infty}^3}{T \langle \gamma_{\mathrm{G}}^2 \rangle N^{2/3}}, \tag{B.1}$$

where $\langle M \rangle$ is the average atomic weight, N is the number of atoms, $V_\circ$ is the average volume per atom, $T_{\mathrm{D},\infty}$ is the Debye temperature, and $\langle \gamma_{\mathrm{G}} \rangle$ is the average Grüneisen parameter, over the temperature range considered. The predicted results are in good agreement with the Slack relation and higher than the single-crystalline experiment results. Applying the fitting to the power-allometric equation ($\kappa_L = aT^b$, where a and b are constants), this NEAIMD results show the exact T^{-1} temperature dependence (a = 9315.7 and b = -1.07), the Slack relation. In addition, this is expected due to the underestimation of the long-range phonon interactions with the limited size of the NEAIMD supercell. We also compare the predictions with the ECMD results (for various empirical interatomic potential models) [10, 16, 50, 217, 218] in Fig. B.6(b). The Yamada interatomic potentials give the best agreement with the NEAIMD results and the Slack relation. This supports the use of these potentials for investigation of the lattice thermal conductivity with the ECMD which allows for decomposition and extraction of the optical phonon contribution.

We decompose the ECMD results for the lattice thermal conductivity of UO_2 into the acoustic and optical components [98, 105, 133], $\kappa_L = \kappa_{L,\mathrm{A}} + \kappa_{L,\mathrm{O}}$, where A and O denote the acoustic and optical. First, the optical component of HCACF is filtered by the fast Fourier low-pass filter with a cutoff frequency of 6 THz [obtained from the upper value of acoustic phonon dispersion in Fig. B.3(a)]. Then the acoustic component is obtained by subtracting the optical part from the total conductivity. The decomposed results are shown in Fig. B.7, and we note that the acoustic contribution has the strong T^{-1} temperature dependence and dominates the lattice thermal conductivity, while as expected the optical component is relatively small and indepen-

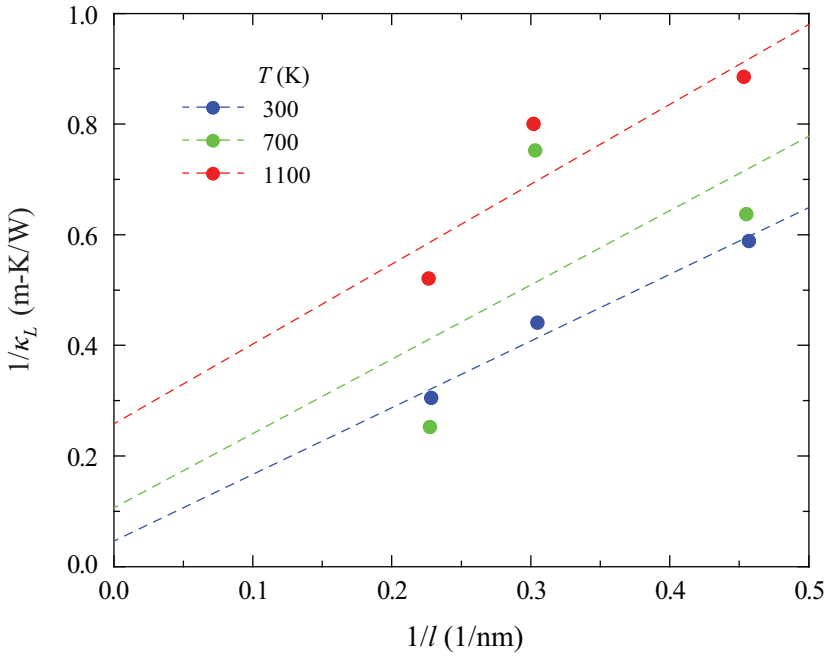

Figure B.5: Variations of the inverse of the lattice thermal conductivity with respect to the inverse of supercell size, found from the NEAIMD simulations, for three different temperatures.

dent of temperature. This is consistent with the phonon transport in bulk, crystalline solids [98, 105]. The Slack relation represents the long-range acoustic transport.

To consider the effects of grain boundary and porosity, the relaxation time model [95, 105] and the effective medium theory [104, 132, 174] are used. Staring with the Slack relation for the pristine UO_2 dominated by the phonon-phonon scattering, we consider the additional grain-boundary scattering for the polycrystalline UO_2. The dominant phonon-phonon relaxation time (τ_{p-p}) is

$$\tau_{p-p} = \frac{3\kappa_{L,\mathrm{S}}}{\rho c_v u_{p,g,\mathrm{A}}^2}, \tag{B.2}$$

where ρ is density and $u_{p,g,\mathrm{A}}$ is the average sound speed. This gives $\tau_{p-p}(T = 300\ \mathrm{K})$ $= 1.69$ ps using the calculated pristine UO_2 properties [$c_v(T = 300\ \mathrm{K}) = 227$ J/kg-K,

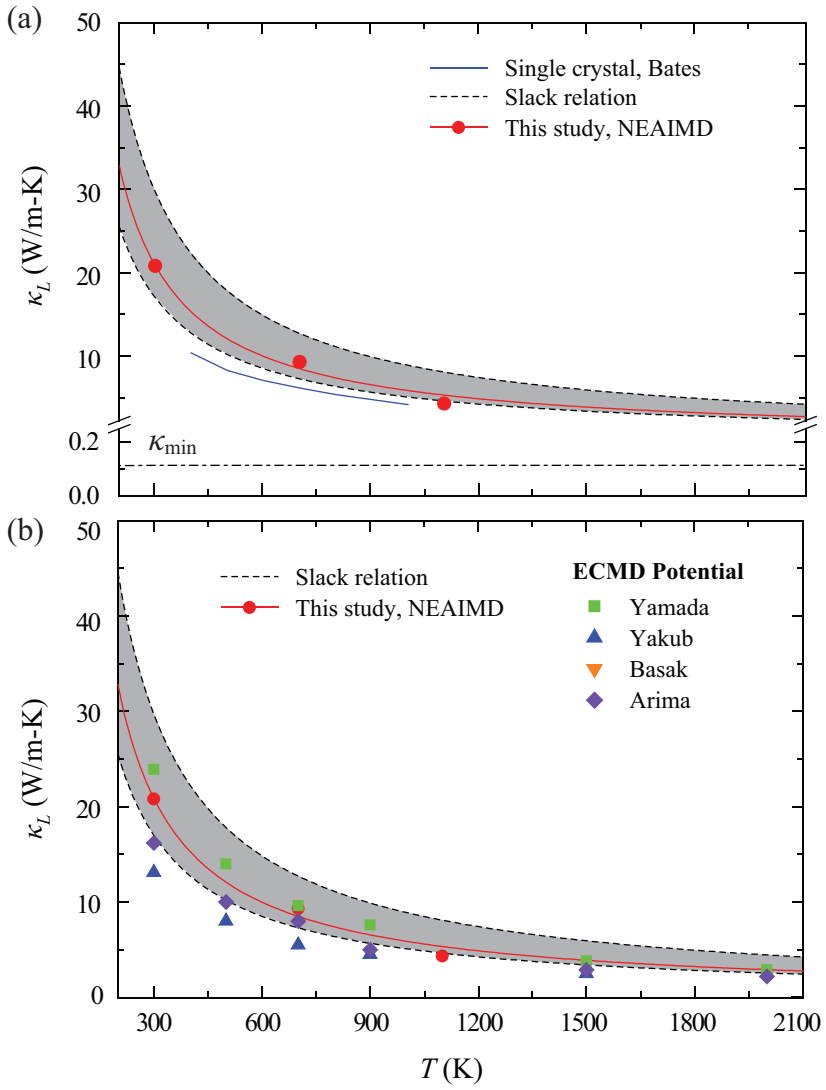

Figure B.6: Variations of the lattice thermal conductivity of UO_2 as a function of temperature. (a) The NEAIMD predicted results, the available experimental results [18], the minimum conductivity [33, 34], and the Slack relation. (b) The NEAIMD and the ECMD predictions using various available interatomic potentials [10, 16, 217, 218]. Using probable ranges of the Debye temperature, 377 K [212] to 383 K [74], and the Grüneisen parameter, 1.55 [80] to 2.0 [137, 155], the results of the Slack relation are shown with gray-shaded band

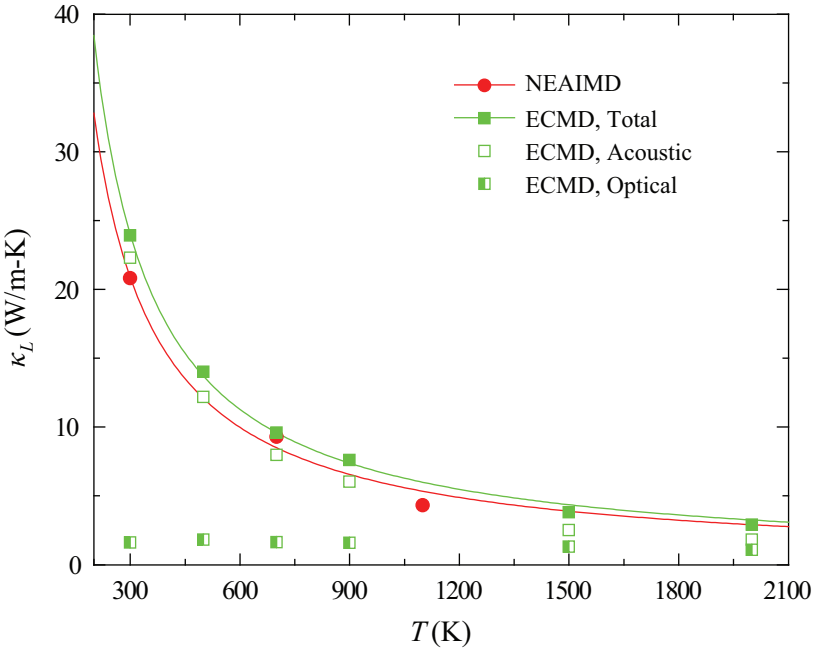

Figure B.7: Variations of the decomposed, acoustic and optical components of the lattice thermal conductivity of pristine UO_2 crystal with temperature. The ECMD results use the Yamada empirical potentials [218].

$\rho(T = 300\ \text{K}) = 11.0\ \text{g/cm}^3$, $u_{p,g,\text{T}} = 5750$ m/s, and $u_{p,g,\text{L}} = 3275$ m/s]. Using the Matthiessen rule, the overall relaxation time with inclusion of the grain-boundary scattering τ_{p-b} is

$$\frac{1}{\tau_p} = \sum_i \frac{1}{\tau_{p,i}} \approx \frac{1}{\tau_{p-p}} + \frac{1}{\tau_{p-b}}. \tag{B.3}$$

The polycrystalline scattering (i.e., grain size effect) is based on the diffuse boundary absorption and emission, i.e., the Casimir boundary scattering [95, 105]. With simplifying assumptions (phonon mean-free-path equal to grain size, and average phonon speed), we have $1/\tau_{p-b} = u_{p,g,\text{A}}/d_g$, where d_g is the grain diameter. Here we consider the half-mixed grain structure of $d_g = 0.01$ and 0.1 μm, and the total relaxation time of grain-boundary scattering is obtained from $1/\tau_{p-b} = 1/\tau_{p-b}(d_g = 0.01\ \mu\text{m}) + 1/\tau_{p-b}(d_g = 0.1\ \mu\text{m})$. This gives $\tau_{p-b} = 2.37$ ps for the simple average of the results

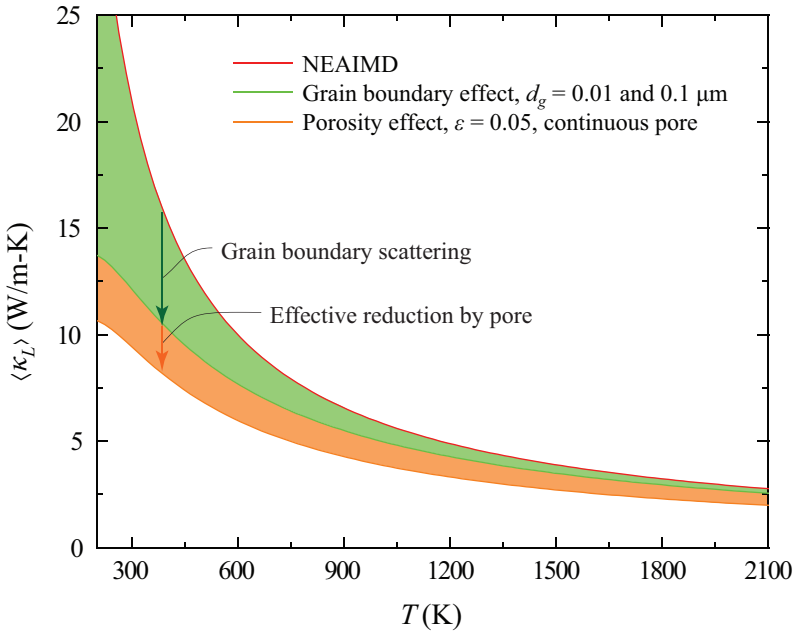

Figure B.8: Variations of the predicted effective lattice thermal conductivity of UO_2 with temperature, for the porosity and grain-boundary scattering effects. The results are from NEAIMD and the scattering and porosity models.

for $d_g = 0.01$ and 0.1 μm.

The effective thermal conductivity of porous media has been studied [104, 132, 174], and here we assume negligible conduction through the pores (i.e., $\kappa_f, \ll \kappa_L$, where κ_f is the pore fluid conductivity). A simple relation [104] for two-dimensional, periodic porous solids with continuous pores gives $\langle \kappa_L \rangle = \kappa_L(1 - \varepsilon^{1/2})$, where $\langle \kappa_L \rangle$ is the effective lattice thermal conductivity and ε is the porosity. The temperature dependence of the combined effective lattice thermal conductivity due to the grain-boundary scattering (average of $d_g = 0.01$ and 0.1 μm) and the pores ($\varepsilon = 0.05$) is shown in Fig. B.8. For these grains the high-density sintered-powder specimen (5% porosity), the grain-boundary scattering dominates at low temperatures. As temperatures, the reverse is predicted.

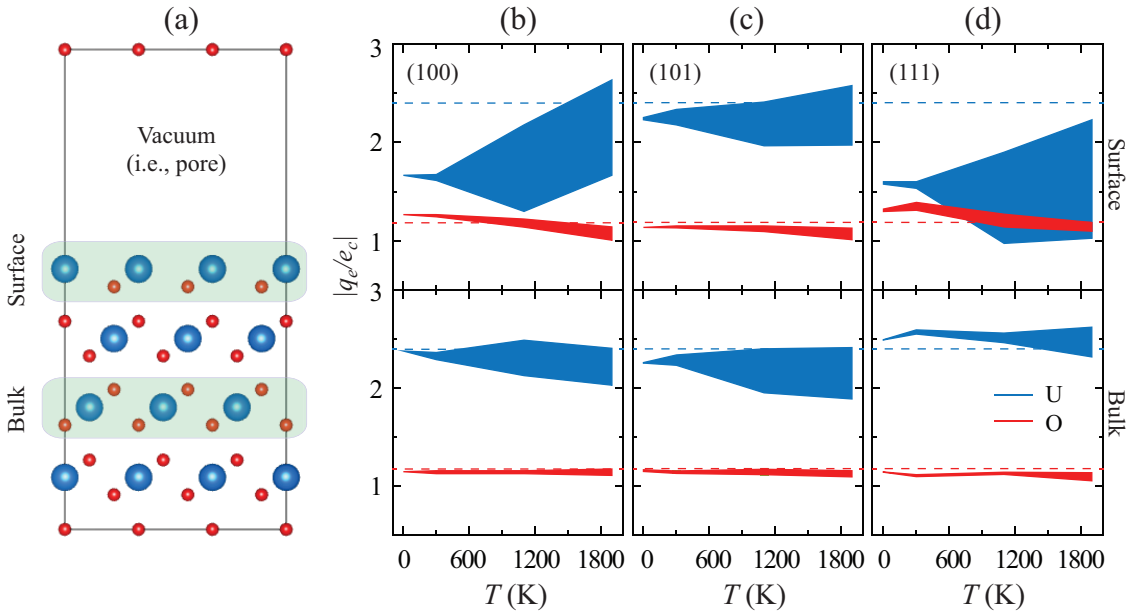

Figure B.9: (a) Atomic structure of UO_2 in the (111) plane. Temperature dependence of the effective charge of UO_2 atoms in the (b) (001), (c) (101), and (d) (111) plane. The upper and lower panels are for the pore surface and the bulk, respectively. The effective charge of U and O atoms at $T = 0$ K are also shown with the dashed lines.

B.3.3 Electronic thermal conductivity

The quantitative prediction of the electronic thermal conductivity (κ_e) of UO_2 has been challenging as given in Section B.1. Here we consider two electronic thermal transport mechanisms, the polaron and the classical intrinsic conduction models.

The polaron model can be examined by the charge and bond analyses of the DFT results [110, 120, 131]. Despite the ionic bonds and the polarization effect of the UO_2 structure, in our DFT results for bulk, pristine crystal structure we not observe any polaron formation over the temperature range of 0 to 2000 K. Since the pristine UO_2 structure is a highly stable, homogeneous symmetric structure, we find no charge

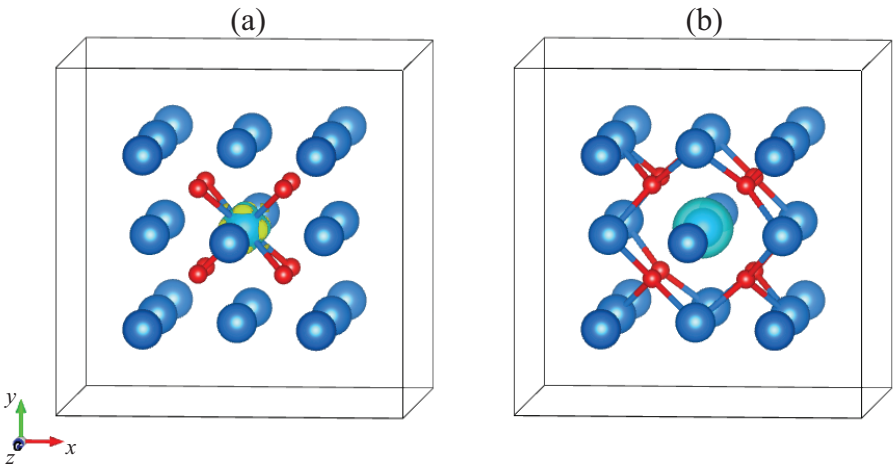

Figure B.10: The iso-charge-density difference surfaces of (a) U^{5+} and (b) U^{3+} compared to U^{4+}. The cut-off bond lengths of U-O used are 2.33 and 2.29 Å, respectively. The iso-charge-density surfaces are set as (a) 0.0137 and (b) 0.0583 e_c-Bohr^{-3}. Yellow and cyan colors mean positive and negative charges.

localization (or trapping) and structural distortion even at high temperatures. To explore such charge localization using the DFT, we use UO_2 slab models with a termination of (111) plane, as shown in Fig. B.9(a). Details are described in Section B.2.3. Using the EAIMD simulations, we investigate the effective charges (q_e) of U and O atoms as a function of temperature, and the results are shown in Figs. B.9(b) to (d). Due to the strong stability and high symmetry of the fluorite structure, initially we did not expect the effective charge changes to be large. Surprisingly, the calculated effective charge of the surface U atoms is significantly reduced and scattered compared to the O atoms, at high temperatures ($T > 500$ K). For comparison, Figs. B.9(b) to (d) also shows with dashed lines the effective charges for the pristine-bulk UO_2 at $T = 0$ K. Note that $q_{e,\mathrm{U}}$ and $q_{e,\mathrm{O}}$ at $T = 0$ K are 2.40 and -1.20 e_c respectively. As proposed in [86, 101, 166], the polaron formation is by the charge localization of U ions, $2U^{4+} \rightarrow U^{3+} + U^{5+}$. So, we believe that such charge localization is one of

the important requirements for polaron formation. Based on our predicted results, the presence of surface (or defect) in UO_2 allows for formation of polaron at high temperatures. Another evidence to verify the existence of a small polaron is the lattice distortion caused by its polarization field. This can be shown with the iso-charge-density contours with positive or negative values from the differential charge density, $\rho_{+1}(\boldsymbol{r})$ - $\rho_0(\boldsymbol{r})$, where $\rho_{+1}(\boldsymbol{r})$ is the charge density of the supercell with the polaron and $\rho_0(\boldsymbol{r})$ is the charge density without any injected excess electron. In Figs. B.10(a) and (b), the polarized and distorted bond lengths of the surrounding O and U atoms induced by the small polaron are visible. The average U-O bond length around the U^{4+} site (2.34 Å) on a pristine structure decreases to 2.30 for U^{5+}, while for the U^{3+} site it increases to 2.53 Å. Based on these results, we identify that charge localized U atoms significantly attract/repel adjacent ions (i.e., distort its lattice structure), and then small polaron is formed.

The polaron migration can be described by the distortion of the lattice deformation along a trajectory, i.e., the equilibrium configuration of two adjacent uranium ion sites. The calculated total energy of a polaron along a migration path is shown Fig. B.11(a). In the inset showing the displacements from point 0 to 4, the point 2 is identified as the activated state, a site with maximum total energy. The difference between the total energy at the activated state (point 2) and the initial state (Point 0 or 4) equals to the activation energy, $E_a = E_{\circ,2}$ - $E_{\circ,1}$, where $E_{\circ,i}$ is the total energy of site i. We find that such difference between the maximum and equilibrium values is about 0.213 eV for UO_2. This value is consistent with the reported values (E_a is in the range of 0.19 to 0.34 eV for nearly stoichiometric UO_2 crystal) in the literature

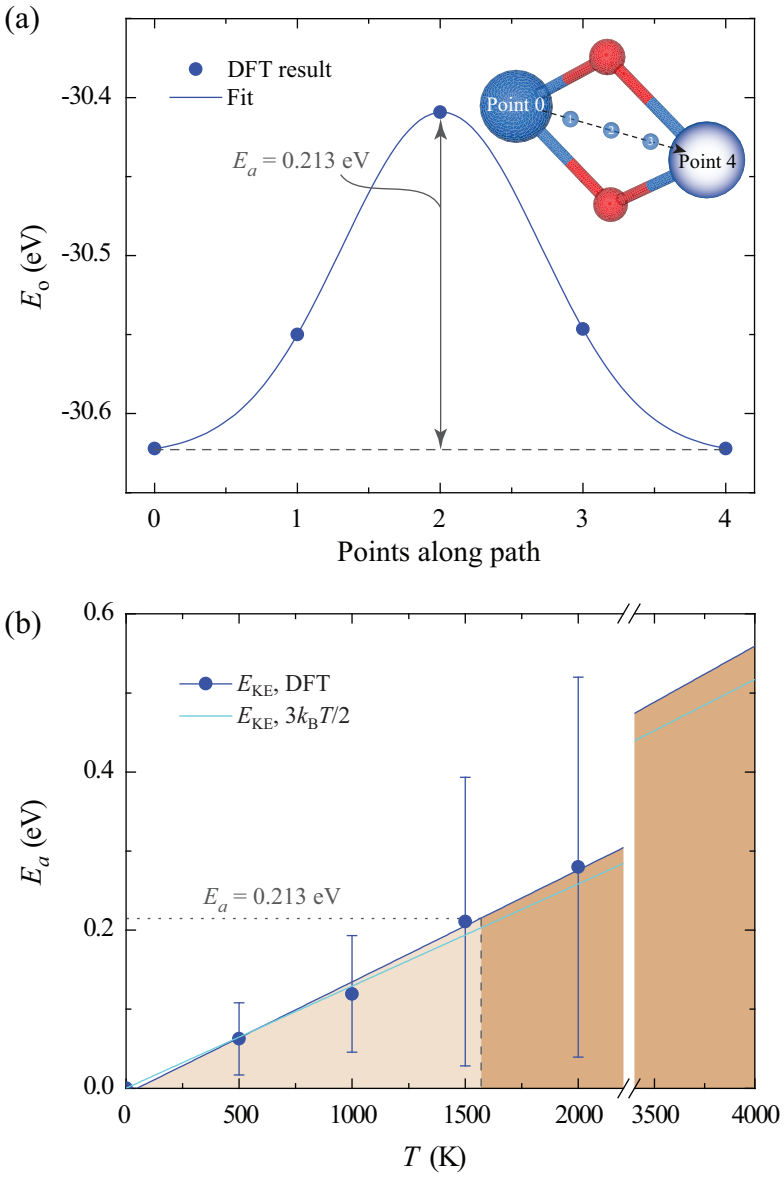

Figure B.11: (a) The calculated total energy along the polaron hopping path between two adjacent U sites in UO_2. (b) The activation energy is found from the temperature dependence of the polaron hopping energy and the kinetic energy.

[11, 18, 51, 144]. In Fig. B.11(b), we compare this activation energy with the average of kinetic energy ($E_{\mathrm{KE}} = mv_i^2/2$, where v_i is the speed of ion i) obtained from the atomic trajectories in EAIMD simulations. The average kinetic energy from an ideal gas, $E_{\mathrm{KE}} = 3k_{\mathrm{B}}T/2$ is also shown. Figure B.11(b) clearly shows that the polaron migration energy of 0.213 eV plays the role of threshold energy for $T < 1600$ K. In this temperature range, we predict that the polaron migration is limited, because the average kinetic energy of the ions is lower than the threshold polaron migration energy.

The polaron electrical conductivity ($\sigma_{e,\mathrm{I}}$) of UO_2 is given by the general formula of [11],

$$\sigma_{e,\mathrm{I}} = \frac{\sigma_{\circ,\mathrm{I}}}{T} 2x(1-2x)\exp(-\frac{E_a}{k_{\mathrm{B}}T}), \tag{B.4}$$

where $\sigma_{e,\mathrm{I}}$ is the pre-exponential factor and x is the defect concentration. Here for E_a we use the activation energy of a small polaron migration ($E_a = 0.213$ eV). From the results of the extrinsic regime of [11], we find $\sigma_{e,\mathrm{I}} = (1.2\times10^6/T)2x(1 - 2x)\exp[-0.213/(k_{\mathrm{B}}T)]$ for $x = 0.01$.

For the intrinsic electrical conduction model we use $\sigma_{e,\mathrm{II}} = n_e e_c \mu_e$, where n_e is carrier concentration and μ_e is the carrier mobility. The carrier concentration based on the quantum-mechanical treatment of conduction electron carriers in a nondegenerate state is expressed as [18]

$$n_e = \frac{2(2\pi m_{e,e} k_{\mathrm{B}}T)^{3/2}}{h_{\mathrm{p}}^3} \exp(-\frac{\Delta E_{e,g}}{2k_{\mathrm{B}}T}), \tag{B.5}$$

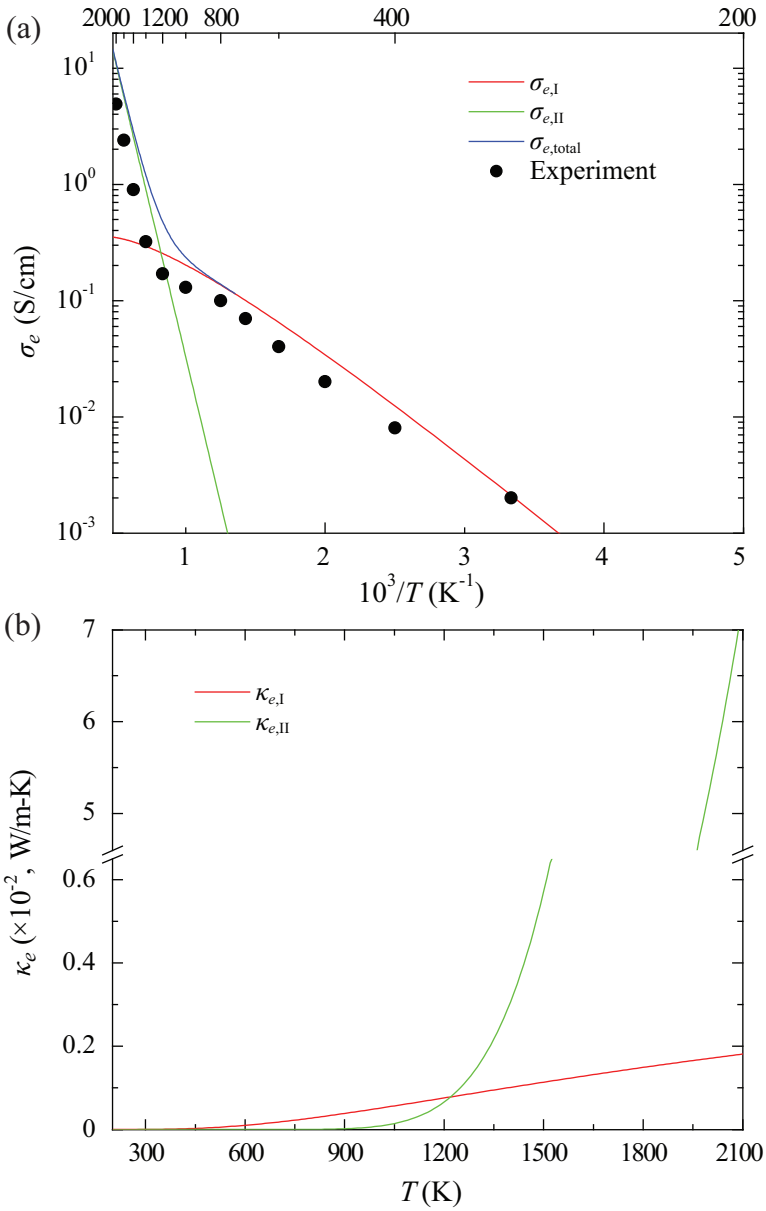

Figure B.12: Calculated temperature dependence of (a) electrical conductivity, and (b) electronic thermal conductivity. The contributions are from small polaron and from intrinsic conduction electrons, activated at different energies.

where $m_{e,e}$ is the effective mass and h_{p} is the Planck's constant. This relation is then approximated to be the simple form $\sigma_{e,\mathrm{II}} = \sigma_{\circ,\mathrm{II}}\exp[-\Delta E_{e,g}/(2k_{\mathrm{B}}T)]$, where $\sigma_{\circ,\mathrm{II}}$ is the pre-exponential factor. Based on the average results of [18], $\sigma_{\circ,\mathrm{II}} = 3.569\times10^3$ S/cm. Figure B.12(a) show the variations of the electrical conductivity as a function of temperature, along with the experimental result for single-crystal UO_2 [18].

The $\log(\sigma_e)$ versus $10^3/T$ for UO_2 in Fig. B.12(a) shows trends corresponding to the two activation energies, 0.213 (for $T < 2000$ K) and 0.9 eV (for $T > 2000$ K). Note that the polaron conduction matches the intrinsic conduction at around 2000 K. This is consistent with the experimental result of [11, 18]. Applying the Wiedemann-Franz law [105], $\sigma_e = N_{\mathrm{L},\circ}\sigma_e T$, where $N_{\mathrm{L},\circ}$ is the Lorenz number, the electronic thermal conductivity is obtained and shown in Fig. B.12(b). Similarly the polaron contribution dominates for $T < 2000$ K, while the intrinsic conduction dominates for $T > 2000$ K.

B.3.4 Total thermal conductivity

Combining phonon and charge transport contributions to the thermal conductivity, the temperature dependence of the predicted total thermal conductivity of UO_2 is shown in Fig. B.13, along with the available experimental results for sintered UO_2 powder. The experimental results show reduced lattice thermal conductivity and larger electronic thermal conductivity, compared to the NEAIMD DFT calculations on the pristine structure. Considering the porosity ($\varepsilon = 0.05$) and the grain boundary scattering (average of $d_g = 0.01$ and 0.1 μm) in the sintered powder, the

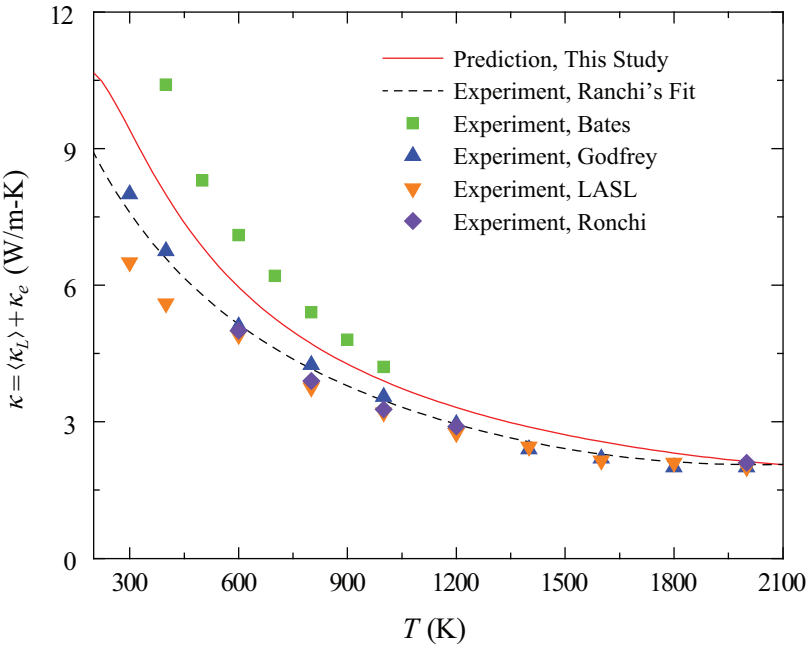

Figure B.13: Variations of the predicted total thermal conductivity of UO_2 as a function of temperature. Available experimental results [17, 44, 78, 164] and fit to them [71, 164] are also shown. Total thermal conductivity is obtained from the sum of the predicted effective lattice thermal conductivity [porous ($\varepsilon = 0.05$) and polycrystalline (average of $d_g = 0.01$ and 0.1 μm)] and the two electronic thermal conductivity contributions.

effective lattice thermal conductivity (Fig. B.8) and adding the two electronic thermal conductivity contributions [Fig. B.12(b)], the predicted results for UO_2 are in good agreement with the experiments [17, 44, 71, 78, 164].

B.4 Summary

Thermal energy transport in UO_2 by phonon, polaron and electron is of fundamental and practical interest and here we approached the three mechanisms from the first principles. We used DFT-based AIMD to explore polaron formation at elevated temperatures and the polaron hopping activation energy. We used NEAIMD and ECMD to find the lattice thermal conductivity and its acoustic and optical compo-

nents. Comparison between first-principles predictions and sintered-powder experiments has always been historically challenging. Here we identify the pore surface as necessary for the formation of polarons. Our predicted results show the lattice thermal conductivity is dominated by the large-range acoustic phonon transport, i.e., the Slack relation for $T < 1500$ K and is reduced by the pore and by the grain-boundary scattering which when included compare well with experiments. The electronic contributions from the hopping surface polarons and from intrinsic conduction electrons contribute to the total thermal conductivity for $T > 1500$ K, and these predicted activation energies are in general agreement with the experiments. The findings can provide insight and help in achieving high-performance, reliable nuclear fuel materials.

Bibliography

[1] B. Abeles. Lattice thermal conductivity of disordered semiconductor alloys at high temperatures. *Phys. Rev.*, 131:1906–1911, 1963.

[2] S. Ahmad, K. Hoang, and S.D. Mahanti. Ab initio study of deep defect states in narrow band-gap semiconductors: Group III impurities in PbTe. *Phys. Rev. Lett.*, 96:056403–1–4, 2006.

[3] S. Ahmad and S.D. Mahanti. Energy and temperature dependence of relaxation time and Wiedemann-Franz law on PbTe. *Phys. Rev. B*, 81:165203–1–11, 2006.

[4] J.B. Ainscough and M.J. Wheeler. The high-temperature thermal conductivity of sintered uranium dioxide. *Brit. J. Appl. Phys.*, 1:859–868, 1968.

[5] E.A. Albanesi, C.M.I. Okoye, C.O. Rodriguez, E.L. Peltzer y Blanca, and A.G. Petukhov. Electronic structure, structural properties, and dielectric functions of IV-VI semiconductors: PbSe and PbTe. *Phys. Rev. B*, 61:16589–16595, 2000.

[6] R.S. Allgaier. Valence bands in lead telluride. *J. Appl. Phys.*, 32:2185–2189, 1961.

[7] M. Amaya, M. Hirai, H. Sakurai, I. Kenichi, M. Sasaki, T. Nomata, K. Kamimura, and R. Iwasaki. Thermal conductivities of irradiated UO_2 and (U,Gd)O_2 pellets. *J. Phys. Colloque*, 300:57–64, 2002.

[8] A.A. Andreev. The band edge structure of the IV-VI semiconductors. *J. Phys. Colloque*, 29:C4–50–61, 1968.

[9] M. Aniya. A chemical approach for the microscopic mechanism of fast ion transport in solids. *Solid State Ion.*, 50:125–129, 1992.

[10] T. Arima, S. Yamasaki, Y. Inagaki, and K. Idemitsu. Evaluation of thermal properties of UO_2 and PuO_2 by equilibrium molecular dynamics simulations from 300 to 2000 K. *J. Alloys Compd.*, 400:43–50, 2005.

[11] S. Aronson, J.E. Rulli, and B.E. Schaner. Electrical properties of nonstoichiometric uranium dioxide. *J. Chem. Phys.*, 35:1382–1388, 1961.

[12] R.R. Asamoto, F.L. Anselin, and A.E. Conti. The effect of density of the thermal conductivity of uranium dioxide. *J. Nuclear Mater.*, 29:67–81, 1969.

[13] T.L. Aselage and D. Emin. *Chemistry, Physics and Materials Science of Thermoelectric Materials: Beyond Bismuth Telluride.* Kluwer, Dordrecht, The Netherlands, 2003.

[14] T.L. Aselage, D. Emin, and S.S. McCready. Conductivities and Seebeck coefficients of boron carbides: Softening bipolaron hopping. *Phys. Rev. B*, 64:054302–1–8, 2001.

[15] T.L. Aselage, D. Emin, S.S. McCready, and R.V. Duncan. Large enhancement of boron carbides' Seebeck coefficients through vibrational softening. *Phys. Rev. Lett.*, 81:2316–2319, 1998.

[16] C.B. Basak, A.K. Sengupta, and H.S. Kamath. Classical molecular dynamics simulation of UO_2 to predict thermophysical properties. *J. Alloys Compd.*, 360:210–216, 2003.

[17] J.L. Bates. *Thermal diffusivity of* UO_2*, in Ceramics Research and Development Quarterly Report July-Sept.* BNWL-198, Richland, WA, 1965.

[18] J.L. Bates, C.A. Hinman, and T. Kawada. Electrical conductivity of uranium dioxide. *J. Am. Ceram. Soc.*, 50:652–656, 1967.

[19] A.D. Becke and E.R. Johnson. A simple effective potential for exchange. *J. Chem. Phys.*, 124:221101–1–4, 2006.

[20] M. Beekman, R.P. Hermann, A. Möchel, F. Juranyi, and G.S. Nolas. A study of low-energy guest phonon modes in clathrate-II Na_xSi_{136} ($x = 3$, 23, and 24). *J. Phys.: Condens. Matter*, 22:355401–1–5, 2010.

[21] C.J. Benmore and P.S. Salmon. Structure of fast ion conducting and semiconducting glassy chalcogenide alloys. *Phys. Rev. Lett.*, 73:264–267, 1994.

[22] R. Berman. *Thermal Conduction in Solids.* Oxford University Press, Oxford, United Kingdom, 1979.

[23] D.I. Bilc, S.D. Mahanti, and M.G. Kanatzidis. Electronic transport properties of PbTe and $AgPb_mSbTe_{2+m}$ systems. *Phys. Rev. B*, 74:125202–1–12, 2006.

[24] K. Biswas, J. He, Q. Zhang, G. Wang, C. Uher, V.P. Dravid, and M.G. Kanatzidis. Strained endotaxial nanostructures with high thermoelectric figure of merit. *Nat. Chem.*, 3:160–166, 2011.

[25] P. Blaha, K. Schwarz, G. Madsen, D. Kvasnicka, and J. Luitz. *WIEN2k, An Augmented Plane Wave + Local Orbitals Program for Calculating Crystal Properties*. Technical University, Wien, Austria, 2001.

[26] P.E. Blöchl. Projector augmented-wave method. *Phys. Rev. B*, 50:17953–17979, 1994.

[27] W. Borchert. Gitterumwandlungen im system $Cu_{2-x}Se$. *Z. Kristallogr.*, 106:5–24, 1945.

[28] M. Born and K. Huang. *Dynamical Theory of Crystal Lattice*. Clarendon Press, Oxford, 1954.

[29] S.K. Bose, O.V. Dolgov, J. Kortus, O. Jepsen, and O.K. Andersen. Pressure dependence of electron-phonon coupling and superconductivity in hcp Fe: A linear response study. *Phys. Rev. B*, 67:214518–1–11, 2003.

[30] M. Bouchacourt and F. Thevenot. The correlation between the thermoelectric properties and stoichiometry in the boron carbide phase B_4C-$B_{10.5}C$. *Phys. Rev. B*, 20:1237–1247, 1985.

[31] E.S. Božin, C.D. Malliakas, P. Souvatzis, T. Proffen, N.A. Spaldin, M.G. Kanatzidis, and S.J.L. Billinge. Entropically stabilized local dipole formation in lead chalcogenides. *Science*, 330:1660–1663, 2010.

[32] D.M. Bylander and L. Kleinman. Structure of $B_{13}C_2$. *Phys. Rev. B*, 43:1487–1491, 1991.

[33] D.G. Cahill, A. Melville, D.G. Schlom, and M.A. Zurbuchen. Low thermal conductivity of $CsBiNb_2O_7$ epitaxial layers. *Appl. Phys. Lett.*, 96:121903–1–3, 2010.

[34] D.G. Cahill, S.K. Watson, and R.O. Pohl. Lower limit to the thermal conductivity of disordered crystals. *Phys. Rev. B*, 46:6131–6140, 1992.

[35] T. Caillat, A. Borshchevsky, and J.-P. Fleurial. Properties of single crystalline semiconducting $CoSb_3$. *J. Appl. Phys.*, 80:4442–4449, 1996.

[36] M. Calandra, N. Vast, and F. Mauri. Superconductivity from doping boron icosahedra. *Phys. Rev. B*, 69:224505–1–5, 2004.

[37] J. Callaway and H.C. von Baeyer. Effect of point imperfections on lattice thermal conductivity. *Phys. Rev.*, 120:1149–1154, 1960.

[38] J.M. Casado, J.H. Harding, and G.J. Hyland. Small-polaron hopping in Mott-insulating UO_2. *J. Phys.: Condens. Matter*, 6:4685–4698, 1994.

[39] L.D. Chen, T. Kawahara, X.F. Tang, T. Goto, T. Hirai, J.S. Dyck, W. Chen, and C. Uher. Anomalous barium filling fraction and n-type thermoelectric performance of $Ba_yCo_4Sb_{12}$. *J. Appl. Phys.*, 90:1864–1868, 2001.

[40] Y. Chen, H.Y. Geng, Y. Kaneta, M. Kinoshita, and S. Iwata. First principles modeling of stability mechanism of nonstoichiometric uranium dioxide. *Comput. Mater. Sci.*, 49:S364–S368, 2010.

[41] H. Chi, H. Kim, J.C. Thomas, X. Su, S. Stackhouse, M. Kaviany, A. Van der Ven, X. Tang, and C. Uher. Configuring pnicogen rings in skutterudites for low phonon conductivity. *Phys. Rev. B*, 86:195209–1–7, 2012.

[42] T. Chonan and S. Katayama. Molecular-dynamics simulation of lattice thermal conductivity in $Pb_{1-x}Sn_xTe$ and $Pb_{1-x}Ge_xTe$ at high temperature. *J. Phys. Soc. Jpn.*, 75:064601–1–8, 2006.

[43] M. Christensen, A.B. Abrahamsen, N.B. Christensen, F. Juranyi, N.H. Andersen, K. Lefmann, J. Andreasson, C.R.H. Bahl, and B.B. Iversen. Avoided crossing of rattler modes in thermoelectric materials. *Nat. Mater.*, 7:811–815, 2008.

[44] J.B. Conway and A.D. Feith. *An interim report on a round robin experimental program to measure the thermal conductivity of stoichiometric uranium dioxide, in General Electric Report.* GEMP-715, Fairfield, CT, 1969.

[45] J. Cooper and N. Frankenberger. Thermoelectricity - A ray from the bright tomorrow. *J. Am. Soc. Naval Engrs.*, 71:657–664, 1959.

[46] J.L. Daniel, J. Matolich, and H.W. Deem. *Thermal conductivity of UO_2, in Hanford Laboratory Technical Report*. HW-69945, Richland, WA, 1962.

[47] S.A. Danilkin, M. Avdeev, T. Sakuma, R. Macquart, and C.D. Ling. Neutron diffraction study of diffuse scattering in $Cu_{2-\delta}Se$ superionic compounds. *J. Alloys Compd.*, 509:5460–5465, 2011.

[48] O. Delaire, J. Ma, K. Marty, A.F. May, M.A. McGuire, M.-H. Du, D.J. Singh, A. Podlesnyak, G. Ehlers, M.D. Lumsden, and B.C. Sales. Entropically stabilized local dipole formation in lead chalcogenides. *Nat. Mater.*, 10:614–619, 2011.

[49] O. Delaire, K. Marty, M.B. Stone, P.R.C. Kent, M.S. Lucas, D.L. Abernathy, D. Mandrus, and B.C. Sales. Phonon softening and metallization of a narrow-gap semiconductor by thermal disorder. *Proc. Nat. Acad. Sci.*, 108:4725–4730, 2011.

[50] R. Devanathan, J. Yu, and W.J. Weber. Energetic recoils in UO_2 simulated using five different potentials. *J. Chem. Phys.*, 130:174502–1–9, 2009.

[51] J. Devreese, R. De Coninck, and H. Pollak. On the conduction mechanism in uranium dioxide. *Phys. Stat. Sol.*, 17:825–829, 1966.

[52] I.K. Dimitrov, M.E. Manley, S.M. Shapiro, J. Yang, W. Zhang, L.D. Chen, Q. Jie, G. Ehlers, A. Podlesnyak, J. Camacho, and Q. Li. Einstein modes in the phonon density of states of the single-filled skutterudite $Yb_{0.2}Co_4Sb_{12}$. *Phys. Rev. B*, 82:174301–1–8, 2010.

[53] V. Domnich, S. Reynaud, R.A. Haber, and M. Chhowalla. Chemical trends of the rattling phonon modes in alloyed germanium clathrates. *J. Appl. Phys.*, 87:7726–7734, 2000.

[54] V. Domnich, S. Reynaud, R.A. Haber, and M. Chhowalla. Boron carbide: Structure, properties, and stability under stress. *J. Am. Ceram. Soc.*, 94:3605–3628, 2011.

[55] B. Dorado, D.A. Andersson, C.R. Stanek, M. Bertolus, B.P. Uberuaga, G. Martin, M. Freyss, and P. Garcia. First-principles calculations of uranium diffusion in uranium dioxide. *Phys. Rev. B*, 86:035110–1–10, 2012.

[56] B. Dorado, G. Jomard, M. Freyss, and M. Bertolus. Stability of oxygen point defects in UO_2 by first-principles DFT+U calculations: Occupation matrix control and Jahn-Teller distortion. *Phys. Rev. B*, 82:035114–1–11, 2010.

[57] R. Dornhaus, G. Nimtz, and B. Schlicht. *Narrow Gap Semiconductors*. Springer, Berlin, Germany, 1985.

[58] S.L. Dudarev, G.A. Botton, S.Y. Savrasov, C.J. Humphreys, and A.P. Sutton. Electron-energy-loss spectra and the structural stability of nickel oxide: An LSDA+U study. *Phys. Rev. B*, 57:1505–1509, 1998.

[59] S.L. Dudarev, G.A. Botton, S.Y. Savrasov, Z. Szotek, W.M. Temmerman, and A.P. Sutton. Electronic structure and elastic properties of strongly correlated metal oxides from first principles: LSDA+U, SIC-LSDA and EELS study of UO_2 and NiO. *Phys. Status Solidi A*, 166:429–443, 1998.

[60] Z.H. Dughaish. Lead telluride as a thermoelectric material for thermoelectric power generation. *Physica B*, 322:205–223, 2002.

[61] D. Emin. Thermoelectric power due to electronic hopping motion. *Phys. Rev. Lett.*, 35:882–885, 1975.

[62] D. Emin. Icosahedral boron-rich solids. *Phys. Today*, 40:55–62, 1987.

[63] D. Emin. Vibrational contribution to the Seebeck coefficient of bipolaronic carriers in boron carbides. *Phys. Status Solidi B*, 205:385–390, 1998.

[64] D. Emin. Enhanced Seebeck coefficient from carrier-induced vibrational softening. *Phys. Rev. B*, 59:6205–6210, 1999.

[65] D. Emin. *Effects of charge carriers' interactions on Seebeck coefficients, in Thermoelectrics Handbook: Macro to Nano.* CRC Press, Boca Raton, FL, 2006.

[66] D. Emin. *Polarons.* Cambridge University Press, New York, NY, 2013.

[67] E. Engel and S.H. Vosko. Exact exchange-only potentials and the virial relation as microscopic criteria for generalized gradient approximations. *Phys. Rev. B*, 47:13164–13174, 1993.

[68] T.-H. Fang and J.-H. Wu. Molecular dynamics simulations on nanoindentation mechanisms of multilayered films. *Comput. Mater. Sci.*, 43:785–790, 2008.

[69] M.I. Fedorov and V.K. Zaitsev. *Thermoelectrics of transition metal silicides, in Thermoelectrics Handbook: Macro to Nano.* CRC Press, Boca Raton, FL, 2006.

[70] J.L. Feldman and D.J. Singh. Lattice dynamics of skutterudites: First-principles and model calculations for $CoSb_3$. *Phys. Rev. B*, 53:6273–6282, 1996.

[71] J.K. Fink. Thermophysical properties of uranium dioxide. *J. Nuclear Mater.*, 279:1–18, 2000.

[72] J.D. Gale and A.L. Rohl. The General Utility Lattice Program (GULP). *Mol. Simul.*, 29:291–341, 2003.

[73] M. Galperin, A. Nitzan, and M. Ratner. Inelastic effects in molecular junction transport: Scattering and self-consistent calculations for the Seebeck coefficient. *Mol. Phys.*, 106:397–404, 2008.

[74] H.Y. Geng, H.X. Song, K. Jin, S.K. Xiang, and Q. Wu. First-principles study on oxidation effects in uranium oxides and high-pressure high-temperature behavior of point defects in uranium dioxide. *Phys. Rev. B*, 84:174115–1–12, 2011.

[75] P. *et al.* Giannozzi. QUANTUM ESPRESSO: A modular and open-source software project for quantum simulations of materials. *J. Phys.: Condens. Matter*, 21:395502–1–19, 2009.

[76] S.N. Girard, J. He, X. Zhou, D. Shoemaker, C.M. Jaworski, C. Uher, V.P. Dravid, J.P. Heremans, and M.G. Kanatzidis. High performance Na-doped PbTe-PbS thermoelectric materials: Electronic density of states modification and shape-controlled nanostructures. *J. Am. Chem. Soc.*, 133:16588–16597, 2011.

[77] F. Giustino, J.R. Yates, I. Souza, M.L. Cohen, and S.G. Louie. Electron-phonon interaction via electronic and lattice Wannier functions: Superconductivity in boron-doped diamond reexamined. *J. Am. Chem. Soc.*, 98:047005–1–4, 2007.

[78] T.G. Godfrey, W. Fulkerson, T.G. Kollie, J.P. Moore, and D.L. McElroy. *The thermal conductivity of uranium dioxide and armco iron by an improved radial heat flow technique, in Oak Ridge National Laboratory Report.* ORNL-3556, Oak Ridge, TN, 1964.

[79] T.G. Godfrey, W. Fulkerson, T.G. Kollie, J.P. Moore, and D.L. McElroy. Thermal conductivity of uranium dioxide from -57 to 1100° C by a radial heat flow technique. *J. Am. Ceram. Soc.*, 48:297–305, 1965.

[80] P. Goel, N. Choudhury, and S.L. Chaplot. Atomistic modeling of the vibrational and thermodynamic properties of uranium dioxide, UO_2. *J. Nuclear Mater.*, 377:438–443, 2008.

[81] H.J. Goldsmid. *Electronic Refrigeration.* Pion, London, United Kingdom, 1986.

[82] L.A. Goldsmith and J.A.M. Douglas. Measurement of the thermal conductivity of uranium dioxide at 670-1270 K. *J. Nuclear Mater.*, 47:31–42, 1973.

[83] M.S. Green. Markoff random processes and the statistical mechanics of time-dependent phenomena. II. Irreversible processes in fluids. *J. Chem. Phys.*, 22:398–413, 1954.

[84] R.N. Hampton, G.A. Sauders, J.H. Harding, and A.M. Stoneham. The pressure dependence of the dielectric constant and electrical conductivity of single crystal uranium dioxide. *J. Nuclear Mater.*, 150:17–23, 1987.

[85] J.H. Harding and D.G. Martin. A recommendation for the thermal conductivity of UO_2. *J. Nuclear Mater.*, 166:223–226, 1989.

[86] J.H. Harding, P. Masri, and A.M. Stoneham. Thermodynamic properties of uranium dioxide: Electronic contributions to the specific heat. *J. Nuclear Mater.*, 92:73–78, 1980.

[87] J.J. Harris and B.K. Ridley. Room temperature transport properties of p-type PbTe. *J. Phys. Chem. Solids*, 33:1455–1464, 1972.

[88] G.L.W. Hart, V. Blum, M.J. Walorski, and A. Zunger. Evolutionary approach for determining first-principles hamiltonians. *Nat. Mater.*, 4:391–394, 2005.

[89] J.Q. He, J.R. Sootsman, L.Q. Xu, S.N. Girard, J.C. Zheng, M.G. Kanatzidis, and V.P. Dravid. Anomalous electronic transport in dual-nanostructured lead telluride. *J. Am. Chem. Soc.*, 133:8786–8789, 2011.

[90] R.R. Heikes and R.W. Ure Jr. *Thermoelectricity: Science and Engineering.* Interscience, New York, NY, 1961.

[91] G. Henkelman, A. Amaldsson, and H. Jonsson. A fast and robust algorithm for bader decomposition of charge density. *Comput. Mater. Sci.*, 36:354–360, 2006.

[92] J.P. Heremans, V. Jovovic, E.S. Toberer, A. Saramat, K. Kurosaki, A. Charoenphakdee, S. Yamanaka, and G.J. Snyder. Enhancement of thermoelectric efficiency in PbTe by distortion of the electronic density of states. *Science*, 321:554–557, 2008.

[93] R.D. Heyding and R.M. Murry. The crystal structure of $Cu_{1.8}Se$, Cu_3Se_2, α- and γ-CuSe, $CuSe_2$, and $CuSe_2$II. *Can. J. Chem.*, 54:841–848, 1976.

[94] C. Hobson, R. Taylor, and J.B. Ainscough. Effect of porosity and stoichiometry on the themal conductivity of uranium dioxide. *J. Phys. D: Appl. Phys.*, 7:1003–1015, 1974.

[95] M.G. Holland. Analysis of lattice thermal conductivity. *Phys. Rev.*, 132:2461–2471, 1963.

[96] B. Houston, R.E. Strakna, and H.S. Belson. Elastic constants, thermal expansion, and Debye temperature of lead telluride. *J. Appl. Phys.*, 39:3913–3916, 1968.

[97] K.F. Hsu, S. Loo, F. Guo, W. Chen, J.S. Dyck, C. Uher, T. Hogan, E.K. Polychroniadis, and M.G. Kanatzidis. Cubic $AgPb_mSbTe_{2+m}$: Bulk thermoelectric materials with high figure of merit. *Science*, 303:818–821, 2004.

[98] B.-L. Huang and M. Kaviany. Structural metrics of high-temperature lattice conductivity. *J. Appl. Phys.*, 100:123507–1–12, 2006.

[99] B.-L. Huang and M. Kaviany. Ab initio and molecular dynamics predictions for electron and phonon transport in bismuth telluride. *Phys. Rev. B*, 77:125209–1–19, 2008.

[100] B.-L. Huang and M. Kaviany. Filler-reduced phonon conductivity of thermoelectric skutterudites: Ab initio calculations and molecular dynamics simulations. *Acta Mater.*, 58:4516–4526, 2010.

[101] G.J. Hyland and J. Ralph. Electronic contributions to the high-temperature thermophysical properties of UO_{2+x}. A critical analysis. *HIgh Temp. High Press.*, 15:179–190, 1983.

[102] W. Jeitschko and D. Braun. $LaFe_4P_{12}$ with filled $CoAs_3$-type structure and isotypic lanthanoid-transition metal polyphosphides. *Acta Crystallogr. Sect. B*, 33:3401–3406, 1977.

[103] P. Jund and R. Jullien. Molecular-dynamics calculation of the thermal conductivity of vitreous silica. *Phys. Rev. B*, 59:13707–13711, 1999.

[104] M. Kaviany. *Principles of Heat Transfer in Porous Media*. Springer, New York, NY, second edition, 1995.

[105] M. Kaviany. *Heat Transfer Physics*. Cambridge University Press, New York, NY, 2008.

[106] M. Kaviany. *Essentials of Heat Transfer*. Cambridge University Press, New York, NY, 2011.

[107] Y. Kawaharada, K. Kurosaki, M. Uno, and S. Yamanaka. Thermoelectric properties of $CoSb_3$. *J. Alloys Compd.*, 315:193–197, 2001.

[108] C. Keffer, T.M. Hayes, and A. Bienenstock. Debye-Waller factors and the PbTe band-gap temperature dependence. *Phys. Rev. B*, 2:1966–1976, 1970.

[109] H. Kim and M. Kaviany. Effect of thermal disorder on high figure of merit in PbTe. *Phys. Rev. B*, 86:045213–1–10, 2012.

[110] H. Kim and M. Kaviany. Coupled polaron-phonon effects on Seebeck coefficient and lattice conductivity of $B_{13}C_2$ from first principles. *Phys. Rev. B*, 87:155133–1–6, 2013.

[111] H. Kim, M. Kaviany, J.C. Thomas, A. Van der Ven, C. Uher, and B. Huang. Structural order-disorder transitions and phonon conductivity of partially filled skutterudites. *Phys. Rev. Lett.*, 105:265901–1–4, 2010.

[112] Y. Kimura and A. Zama. Thermoelectric properties of *p*-type half-Heusler compound HfPtSn and improvement for high-performance by Ir and Co additions. *Appl. Rev. Lett.*, 89:172110–1–3, 2006.

[113] P.G. Klemens. Thermal resistance due to point defects at high temperatures. *Phys. Rev.*, 119:507–509, 1960.

[114] A. Kotani and T. Yamazaki. Systematic analysis of core photoemission spectra for actinide di-oxides and rare-earth sesqui-oxides. *Prog. Theor. Phys.*, 108:117–131, 1992.

[115] M.M. Koza, M.R. Johnson, R. Viennois, H. Mutka, L. Girard, and D. Ravot. Breakdown of phonon glass paradigm in La- and Ce-filled Fe_4Sb_{12} skutterudites. *Nat. Mater.*, 7:805–810, 2008.

[116] G. Kresse and J. Furthmüller. Efficient iterative schemes for *ab initio* total-energy calculations using a plane-wave basis set. *Phys. Rev. B*, 54:11169–11186, 1996.

[117] G. Kresse and D. Joubert. From ultrasoft pseudopotentials to the projector augmented-wave method. *Phys. Rev. B*, 59:1758–1775, 1999.

[118] R. Kubo. Statistical-mechanical theory of irreversible processes. I. General theory and simple applications to magnetic and conduction problems. *J. Phys. Soc. Jpn.*, 12:570–586, 1957.

[119] U. Kuhlmann, H. Werheit, and K.A. Schwetz. Distribution of carbon atoms on the boron carbide structure elements. *J. Alloys Compd.*, 189:249–258, 1992.

[120] J. Lee, S. Pennycook, and S.T. Pantelides. Simultaneous enhancement of electonic and Li^+ ion conductivity in $LiFePO_4$. *Appl. Phys. Lett.*, 101:033901–1–4, 2012.

[121] H. Li, X.F. Tang, Q.J. Zhang, and C. Uher. High performance $In_xCe_yCo_4Sb_{12}$ thermoelectric materials with in situ forming nanostructured InSb phase. *Appl. Phys. Lett.*, 94:102114–1–3, 2009.

[122] H. Liu, X. Shi, F. Xu, L. Zhang, W. Zhang, L. Chen, Q. Li, C. Uher, T. Day, and G.J. Snyder. Copper ion liquid-like thermoelectrics. *Nat. Mater.*, 11:422–425, 2012.

[123] W.-S. Liu, B.-P. Zhang, L.-D. Zhao, and J.-F. Li. Improvement of thermoelectric performance of $CoSb_{3-x}Te_x$ skutterudite compounds by additional substitution of IVB-group elements for Sb. *Chem. Mater.*, 20:7526–7531, 2008.

[124] M. Lundstrom. *Fundamentals of Carrier Transport.* Cambridge University Press, Cambridge, United Kingdom, 2000.

[125] J.R. MacEwan, R.L. Stoute, and M.J.F. Notley. Effect of porosity on the thermal conductivity of UO_2. *J. Nuclear Mater.*, 24:109–112, 1967.

[126] O. Madelung, U. Rössler, and M. Schulz, editors. *Springer Materials - The Landolt-Börnstein Database, Volume III/17G-41D.* Springer, Berlin, Germany, 2013.

[127] G.K.H. Madsen and D.J. Singh. BoltzTraP. A code for calculating band-structure dependent quantities. *Comput. Phys. Commun.*, 175:67–71, 2006.

[128] A.A. Maradudin. *Theory of Lattice Dynamics in the Harmonic Approximation.* Academic Press, New York, NY, 1971.

[129] M. Marathe, M. Imam, and S. Nrasimhan. Elastic and chemical contributions to the stability of magnetic surface alloys on Ru(0001). *Phys. Rev. B*, 79:085413–1–9, 2009.

[130] D.G. Martin. The thermal expansion of solid UO_2 and (U,Pu) mixed oxides - A review and recommendations. *J. Nuclear Mater.*, 152:94–101, 1988.

[131] T. Maxisch, F. Zhou, and G. Ceder. Ab initio study of the migration of small polarons in olivine Li_xFePO_4 and their association with lithium ions and vacancies. *Phys. Rev. B*, 73:104301–1–6, 2006.

[132] J.C. Maxwell. *A Treatise on Electricity and Magnetism.* Clarendon Press, Oxford, United Kingdom, 1904.

[133] A.J.H. McGaughey and M. Kaviany. Thermal conductivity decomposition and analysis using molecular dynamics simulations Part II. Complex silica structures. *Int. J. Heat Mass Transfer*, 47:1799–1816, 2004.

[134] D.A. McQuarrie. *Statistical Mechanics.* University Science Books, Sausalito, CA, 2000.

[135] G.P. Meisner, D.T. Morelli, S. Hu, J. Yang, and C. Uher. Structure and lattice thermal conductivity of fractionally filled skutterudites: Solid solutions of fully filled and unfilled end members. *Phys. Rev. Lett.*, 80:3551–3554, 1998.

[136] K. Minato, T. Shiratori, H. Serizawa, K. Hayashi, K. Une, K. Nogita, M. Hirai, and M. Amaya. Thermal conductivities of irradiated UO_2 and (U,Gd)O_2. *J. Nuclear Mater.*, 288:57–65, 2001.

[137] A.C. Momin and M.D. Karkhanavala. Temperature dependence of the grüneisen parameter and lattice vibration frequencies of UO_2 and ThO_2 in the range 298-2300 K. *High Temp. Sci.*, 10:45–52, 1978.

[138] J.P. Moore and D.L. McElroy. Thermal conductivity of nearly stoichiometric single-crystal and polycrystalline UO_2. *J. Am. Ceram. Soc.*, 54:40–46, 1971.

[139] D.T. Morelli, V. Jovovic, and J.P. Heremans. Low temperature properties of the filled skutterudite $CeFe_4Sb_{12}$. *J. Appl. Phys.*, 77:3777–3781, 1995.

[140] D.T. Morelli, V. Jovovic, and J.P. Heremans. Intrinsically minimal thermal conductivity in cubic I-V-VI_2 semiconductors. *Phys. Rev. Lett.*, 101:035901–1–4, 2008.

[141] A. Muhlenen, N. Errien, M. Schaer, M.-N. Bussac, and L. Zuppiroli. Thermopower measurements on pentacene transistors. *Phys. Rev. B*, 75:115338–1–6, 2007.

[142] F. Müller-Plathe. A simple nonequilibrium molecular dynamics method for calculating the thermal conductivity. *J. Chem. Phys.*, 106:6082–6085, 1997.

[143] M. Murabayashi. Thermal conductivity of ceramic solid solutions. *J. Nucl. Sci. Technol.*, 7:559–563, 1970.

[144] P. Nagels, J. Devreese, and M. Denayer. Electronic conduction in single crystals of uranium dioxide. *J. Appl. Phys.*, 35:1175–1180, 1964.

[145] Y. Noda, S. Ohba, S. Sato, and Y. Saito. Charge distribution and atomic thermal vibration in lead chalcogenide crystals. *Acta Crystallogr. Sect. B*, 39:312–317, 1983.

[146] G.A. Nolas, G.S. Slack, D.T. Morelli, T.M. Tritt, and A.C. Ehrlich. The effect of rare-earth filling on the lattice thermal conductivity of skutterudites. *J. Appl. Phys.*, 79:4002–4008, 1996.

[147] G.S. Nolas, J.L. Cohn, and G.A. Slack. Effect of partial void filling on the lattice thermal conductivity of skutterudites. *Phys. Rev. B*, 58:164–170, 1998.

[148] G.S. Nolas, J. Sharp, and H.J. Goldsmid. *Thermoelectrics: Basic Principles and New Materials Developments*. Springer, Berlin, Germany, 2001.

[149] I. Oftedal. The crystal structure of skutterudite and smaltite-chloanthite. *Z. Kristallogr.*, A66:517, 1928.

[150] M. Oliveria, R.K. McMullan, and B.J. Wuensch. Single crystal neutron diffraction analysis of the cation distribution in the high-temperature phases α-$Cu_{2-x}S$, α-$Cu_{2-x}Se$, and α-Ag_2Se. *Solid State Ion.*, 28-30:1332–1337, 1988.

[151] K. Parlinski. PHONON *Software*. Cracow, Poland, 2008.

[152] Y. Pei, A. LaLonde, S. Iwanaga, and G.J. Snyder. High thermoelectric figure of merit in heavy hole dominated PbTe. *Energy Environ. Sci.*, 4:2085–2089, 2011.

[153] Y. Pei, X. Shi, A. LaLonde, H. Wang, L. Chen, and G.J. Snyder. Convergence of electronic bands for high performance bulk thermoelectrics. *Nature*, 473:66–69, 2011.

[154] J.P. Perdew, K. Burke, and M. Ernzerhof. Generalized gradient approximation made simple. *Phys. Rev. Lett.*, 77:3865–3868, 1996.

[155] C.G.S. Pillai and A.M. George. Thermal conductivity of uranium dioxide. *J. Nuclear Mater.*, 200:78–81, 1993.

[156] A. Popescu, L.M. Woods, J. Martin, and G.S. Nolas. Model of transport properties of thermoelectric nanocomposite materials. *Phys. Rev. B*, 79:205302–1–7, 2009.

[157] G. Profeta, M. Calandra, and F. Mauri. Phonon-mediated superconductivity in graphene by lithium deposition. *Nat. Phys.*, 8:131–134, 2012.

[158] J.J. Pulikkotil, H.N. Alshareef, and U. Schwingenschlögl. Effects of $FeSb_6$ octahedral deformations on the electronic structure of $LaFe_4Sb_{12}$. *Chem. Phys. Lett.*, 514:54–57, 2011.

[159] B. Qiu, H. Bao, G. Zhang, Y. Wu, and X. Ruan. Molecular dynamics simulations of lattice thermal conductivity and spectral phonon mean free path of PbTe: Bulk and nanostructures. *Comput. Mater. Sci.*, 53:278–285, 2011.

[160] J. Rabone and M. Krack. A procedure for bypassing metastable staes in local basis set DFT+U calculations and its application to uranium dioxide surfaces. *Comput. Mater. Sci.*, 71:157–164, 2013.

[161] E. Riccardi, J.-C. Wang, and A.I. Liapis. Rational surface design for molecular dynamics simulations of porous polymer adsorbent media. *J. Phys. Chem. B*, 112:7478–7488, 2008.

[162] L.M. Rogers. The Hall mobility and thermoelectric power of p-type lead telluride. *Brit. J. Appl. Phys.*, 18:1227–1235, 1967.

[163] P. Rogl. *Formation and crystal chemistry of clathrates, in Thermoelectrics Handbook: Macro to Nano.* CRC Press, Boca Raton, FL, 2006.

[164] C. Ronchi, M. Sheindlin, M. Musella, and G.J. Hyland. Thermal conductivity of uranium dioxide up to 2900 K from simultaneous measurement of the heat capacity and thermal diffusivity. *J. Appl. Phys.*, 85:776–789, 1999.

[165] V.V. Rondinella and T. Wiss. The high burn-up structure in nuclear fuel. *Mater. Today*, 13:24–32, 2010.

[166] P. Ruello, K.D. Becker, K. Ullrich, L. Desgranges, C. Petot, and G. Petot-Ervas. Thermal variation of the optical absorption of UO_2: Determination of the small polaron self-energy. *J. Nuclear Mater.*, 328:46–54, 2004.

[167] P. Ruello, G. Petot-Ervas, and C. Petot. Electrical conductivity and thermoelectric power of uranium dioxide. *J. Am. Ceram. Soc.*, 88:604–611, 2005.

[168] C. Ruf, H. Obloh, B. Junge, E. Gmelin, , and K. Ploog. Phonon-drag effect in GaAs-Al_xGa_{1-x}. *Phys. Rev. B*, 37:6377–6380, 1998.

[169] S. Rundqvis and N. Ersson. Structure and bonding in skutterudite-type phosphides. *Arkiv. Kemi*, 30:103–114, 1969.

[170] B.C. Sales, D. Mandrus, and R.K. Williams. Filled skutterudite antimonides: A new class of thermoelectric materials. *Science*, 272:1325–1328, 1996.

[171] J.R. Salvador, J. Yang, X. Shi, H. Wang, A.A. Wereszczak, H. Kong, and C. Uher. Transport and mechanical properties of Yb-filled skutterudites. *Science*, 89:1517–1534, 2009.

[172] G.A. Samara, D. Emin, and C. Wood. Pressure and temperature dependences of the electronic conductivity of boron carbides. *Phys. Rev. B*, 32:2315–2318, 1985.

[173] J.M. Sanchez, F. Ducastelle, and D. Gratias. Generalized cluster description of multicomponent systems. *Physica A*, 128:334–350, 1984.

[174] K.W. Schlichting, N.P. Padture, and P.G. Klemens. Thermal conductivity of dense and porous yttria-stabilized zirconia. *J. Mater. Sci.*, 36:3003–3010, 2001.

[175] H.E. Schmidt. Some considerations on the thermal conductivity of stoichiometric uranium dioxide at high temperatures. *J. Nuclear Mater.*, 39:234–237, 1971.

[176] A. Shakouri, E.Y. Lee, D.L. Smith, V. Narayanamurti, and J.E. Bowers. Thermoelectric effects in submicron heterostructure barriers. *Microscale Thermophys. Eng.*, 2:37–47, 1998.

[177] X. Shi, J. Yang, J.R. Salvador, M. Chi, J.Y. Cho, H. Wang, and S. Bai. Multiple-filled skutterudites: High thermoelectric figure of merit through separately optimizing electrical and thermal transports. *J. Am. Chem. Soc.*, 133:7837–7846, 2011.

[178] X. Shi, W. Zhang, L.D. Chen, and J. Yang. Filling fraction limit for intrinsic voids in crystals: Doping in skutterudites. *Phys. Rev. Lett.*, 95:185503–1–4, 2005.

[179] X. Shi, W. Zhang, L.D. Chen, and J. Yang. Thermodynamic analysis of the filling fraction limits for impurities in $CoSb_3$ based on ab initio calculations. *Acta Mater.*, 56:1733–1740, 2008.

[180] S. Shin, M. Kaviany, T. Desai, and R. Bonner. Roles of atomic restructuring in interfacial phonon transport. *Phys. Rev. B*, 82:081302(R)–1–4, 2010.

[181] S. Shin, M. Kaviany, T. Desai, and R. Bonner. Structural study of α-rhombohedral boron at high pressures. *J. Phys. Soc. Jpn.*, 80:084601–1–13, 2011.

[182] D.J. Singh. Doping-dependent thermopower of PbTe from Boltzmann transport calculations. *Phys. Rev. B*, 81:195217–1–6, 2010.

[183] D.J. Singh and L. Nordstrom. *Planewaves, Pseudopotentials and the LAPW Method*. Springer, Berlin, Germany, second edition, 2006.

[184] F. Skomursk, R.C. Ewing, A.L. Rohl, J.D. Gale, and U. Becker. Quantum mechanical vs. empirical potential modeling of uranium dioxide (UO_2) surfaces: (111), (110), and (100). *Am. Mineral.*, 91:1761–1772, 2006.

[185] G.A. Slack. *The thermal conductivity of nonmetallic solids, in Solid State Physics*. Academic Press, New York, NY, 1979.

[186] G.A. Slack. *New materials and performance limits for thermoelectric cooling, in CRC Handbook of Thermoelectrics*. CRC Press, Boca Raton, FL, 1995.

[187] G.A. Slack, D.W. Oliver, and F.H. Horn. Thermal conductivity of boron and some boron compounds. *Phys. Rev. B*, 4:1714–1720, 1971.

[188] G.P. Sorokin, Yu.M. Papshev, and P.T. Oush. Photoconductivity of Cu_2S, Cu_2Se, and Cu_2Te. *Sov. Phys. Solid State*, 7:1810–1811, 1966.

[189] G.P. Srivastava. *The Physics of Phonons*. Adam Hilger, Bristol, United Kingdom, 1995.

[190] S. Stackhouse, L. Stixrude, and B.B. Karki. Thermal conductivity of periclase (MgO) from first principles. *Phys. Rev. Lett.*, 104:208501–1–4, 2010.

[191] E.F. Steigmeier and B. Abeles. Scattering of phonons by electrons in germanium-silicon alloys. *Phys. Rev.*, 136:A1149–A1155, 1964.

[192] A.L.N. Stevels and F. Jellinek. Phase transformations in copper chalcogenides: I. The copper-selenium system. *Recl. Trav. Chim.*, 90:273–283, 1971.

[193] X. Su, H. Li, G. Wang, H. Chi, X. Zhou, X. Tang, Q. Zhang, and C. Uher. Structure and transport properties of double-doped $CoSb_{2.75}Ge_{0.25-x}Te_x$ (x = 0.125-0.20) with in situ nanostructure. *Chem. Mater.*, 23:2948–2955, 2011.

[194] X. Su, H. Li, Y. Yan, G. Wang, H. Chi, X. Zhou, X. Tang, Q. Zhang, and C. Uher. Microstructure and thermoelectric properties of $CoSb_{2.75}Ge_{0.25-x}Te_x$ prepared by rapid solidification. *Acta Mater.*, 60:3536–3544, 2012.

[195] P.W. Tasker. The surface properties of uranium dioxide. *Surf. Sci.*, 78:315–324, 1979.

[196] R.N. Tauber, A.A. Machonis, and I.B. Cadoff. Thermal and optical energy gaps in PbTe. *J. Appl. Phys.*, 37:4855–4860, 1966.

[197] I. Terasaki, Y. Sasago, and K. Uchinokura. Large thermoelectric power in $NaCo_2O_4$ single crystals. *J. Appl. Phys.*, 56:R12685–R12687, 1997.

[198] F. Thevenot. Boron carbide-a comprehensive review. *J. Eur. Ceram. Soc.*, 6:205–225, 1990.

[199] F. Tran and P. Blaha. Accurate band gaps of semiconductors and insulators with a semilocal exchange-correlation potential. *Phys. Rev. Lett.*, 102:226401–1–4, 2009.

[200] K. Uchida, H. Adachi, T. An, T. Ota, M. Toda, B. Hillebrands, S. Maekawa, and E. Saitoh. Long-range spin Seebeck effect and acoustic spin pumping. *Nat. Mater.*, 10:737–741, 2011.

[201] C. Uher. *Skutterudites: Prospective novel thermoelectrics, in Semiconductors and Semimetals Vol. 69: Recent Trends in Thermoelectric Materials Research I.* Academic Press, San Diego, CA, 2001.

[202] C. Uher. *Skutterudite-based thermoelectrics, in Thermoelectrics Handbook: Macro to Nano.* CRC Press, Boca Raton, FL, 2006.

[203] N. Vast, J. Sjakste, and E. Betranhandy. Boron carbides from first principles. *J. Phys.: Conf. Ser.*, 176:012002–1–18, 2009.

[204] B.W. Veal and D.J. Lam. X-ray photoelectron studies of thorium, uranium, and their dioxides. *Phys. Rev. B*, 10:4902–4908, 1975.

[205] Yu.I. Vesnin and Yu.V. Shubin. On the constancy of the average crystal lattice parameter in the decay of the solid solutions PbS-PbTe. *Mat. Res. Bull.*, 19:1355–1359, 1984.

[206] C.J. Vineis, T.C. Harman, S.D. Calawa, M.P. Walsh, R.E. Reeder, R. Singh, and A. Shakouri. Carrier concentration and temperature dependence of the electronic transport properties of epitaxial PbTe and PbTe/PbSe nanodot superlattices. *Phys. Rev. B*, 77:235202–1–14, 2008.

[207] D. Wang, L. Tang, M. Long, and Z. Shuai. Anisotropic thermal transport in organic molecular crystals from nonequilibrium molecular dynamics simulations. *J. Phys. Chem. C*, 115:5940–5946, 2011.

[208] H. Wang, Y. Pei, A.D. LaLonde, and G.J. Snyder. Heavily doped p-type PbSe with high thermoelectric performance: An alternative for PbTe. *Adv. Mater.*, 23:1366–1370, 2011.

[209] T. Watanabe, S.B. Sinnott, J.S. Tulenko, R.W. Grimes, P.K. Schelling, and S.R. Phillpot. Thermal transport properties of uranium dioxide by molecular dynamics simulations. *J. Nuclear Mater.*, 375:388–396, 2008.

[210] D. Wee, B. Kozinsky, N. Marzari, and M. Fornari. Effects of filling in $CoSb_3$: Local structure, band gap, and phonons from first principles. *Phys. Rev. B*, 81:045204–1–11, 2010.

[211] H. Werheit. On excitons and other gap states in boron carbide. *J. Phys.: Condens. Matter*, 18:10655–10662, 2006.

[212] B.T.M. Willis. Neutron diffraction studies of the actinide oxides. II. Thermal motions of the atoms in uranium dioxide and thorium dioxide between room temperature and 1100°. *Proc. R. Soc. Lond. A*, 274:134–144, 1963.

[213] C. Wood. Transport properties of boron carbides. *AIP Conf. Proc.*, 140:206–215, 1986.

[214] C. Wood and D. Emin. Conduction mechanism in boron carbide. *Phys. Rev. B*, 29:4582–4587, 1984.

[215] C. Wood, D. Emin, and P.E. Gray. Thermal conductivity behavior of boron carbides. *Phys. Rev. B*, 31:6811–6814, 1985.

[216] L. Xu, Y. Zheng, and J.-C. Zheng. Thermoelectric transport properties of PbTe under pressure. *Phys. Rev. B*, 82:195102–1–16, 2010.

[217] E. Yakub, C. Ronchi, and D. Staicu. Molecular dynamics simulation of premelting and melting phase transitions in stoichiometric uranium dioxide. *J. Chem. Phys.*, 127:094508–1–11, 2007.

[218] K. Yamada, K. Kurosaki, M. Uno, and S. Yamanaka. Evaluation of thermal properties of uranium dioxide by molecular dynamics. *J. Alloys Compd.*, 307:10–16, 2000.

[219] Q. Yin and S.Y. Savrasov. Origin of low thermal conductivity in nuclear fuels. *Phys. Rev. Lett.*, 100:225504–1–4, 2008.

[220] B. Yu, W. Liu, S. Chen, H. Wang, H. Wang, G. Chen, and Z. Ren. Thermoelectric properties of copper selenide with ordered selenium layer and disordered copper layer. *Nano Energy*, 1:472–478, 2012.

[221] Y. Yun, D. Legut, and P.M. Oppeneer. Phonon spectrum, thermal expansion and heat capacity of UO_2 from first principles. *J. Nuclear Mater.*, 426:109–114, 2012.

[222] L. Zhang, G. Rogl, A. Grytsiv, S. Puchegger, J. Koppensteiner, F. Spieckermann, H. Kabelka, M. Reinecker, P. Rogl, W. Schranz, M. Zehetbauer, and M.A. Carpenter. Mechanical properties of filled antimonide skutterudites. *Mater. Sci. Eng. B*, 170:26–31, 2010.

[223] Y. Zhang, X. Ke, P.R.C. Kent, J. Yang, and C. Chen. Anomalous lattice dynamics near the ferroelectric instability in PbTe. *Phys. Rev. Lett.*, 107:175503–1–4, 2011.